Electronic and Lattice Structure of the Strongly Correlated Transition Metal Oxides Fe_3O_4 and $LaSr_2Mn_2O_7$: a hybrid density functional study

Andrew Daniel Rowan

A Thesis submitted to
The University of Dublin
Trinity College
for the degree of
Doctor of Philosophy

SCHOOL OF PHYSICS
TRINITY COLLEGE DUBLIN

May 2007

Declaration

This thesis is submitted to the University of Dublin by the undersigned for the degree of Doctor of Philosophy. This thesis has not been submitted as an exercise for a degree at this or any other university. The work carried out within is entirely the candidate's own. The Library of the University of Dublin, Trinity College, may lend or copy this thesis upon request.

Andrew Rowan

March 2007

Dublin

Summary

This thesis is a theoretical study of the electronic and lattice structure of the inverse spinel magnetite (Fe_3O_4) and the half-doped bilayered manganite system $LaSr_2Mn_2O_7$. Both systems are strongly correlated transition metal oxides exhibiting a rich variety of physical behaviours, due to the complex interactions of charge, spin, orbital and lattice degrees of freedom. A hybrid density functional approach is adopted in order to circumvent the well-known difficulties of traditional density function theory and Hartree-Fock theory in accurately describing the electronic structure of such strongly correlated transition metal oxides.

The first aim of this thesis is to investigate the Verwey structural and metal-insulator phase transition in magnetite. Partial charge ordering (CO) was found to exist on the octahedral Fe_B sublattice in the low temperature monoclinic structure. The charge ordering arrangement does not conform to the well-known Anderson criterion for ferrites. We find that this CO is accompanied by an associated orbital ordering on Fe_B sites. We also find that charge populations on the tetrahedral Fe_A sites are closer to 2+ than the 3+ state which emerges from a simple ionic picture. Crystal structure optimisations have been carried out on the low-temperature structure using 30% and 50% Hartree-Fock exchange mixing in the hybrid density functional. These calculations show that the electron-lattice interaction plays a key role in opening the band gap at the Verwey transition. The high-temperature cubic $Fd\bar{3}m$ cell is also studied. Charge and orbital order are found to be energetically favourable in an insulating solution at 30% Hartree-Fock exchange mixing. A symmetry-breaking structure optimisation to a $P1$ space group demonstrates the correlation of lattice distortion with orbital ordering. A group theoretic symmetry analysis is performed in order to identify the cell distortion modes which feature in this displacive phase transition. It is shown that the Verwey transition results from the cooperative effects of

strong electron repulsion and strong electron coupling to the lattice, leading to polaronic behaviour, and that both factors must be adequately accounted for in any theoretical consideration of magnetite physics.

The thesis then investigates the half-doped bilayer manganite $LaSr_2Mn_2O_7$, which is of interest due to its colossal magnetoresistance and structural similarity to the high-temperature superconducting cuprates. The exact antiferromagnetic ground state is established, and evidence is found of extreme two-dimensional characteristics, including a suppressed but finite density of states at the Fermi energy. This feature remains robust even for calculations with up to 60% Hartree-Fock exchange mixing, and for ab-initio optimisation of the lattice geometry. This is consistent with photoemission experiments which point towards the existence of a 'pseudogap' phase in this family of manganite compounds.

Acknowledgements

First and foremost, I would like to warmly thank my supervisor Dr. Charles Patterson for all the help and support I've received during the course of this work. The door to Charles' office has always been open for all my questions and general ramblings, and all his friendly and patient advice and suggestions are deeply appreciated. I am particularly grateful to Charles for his understanding and encouragement regarding the Masters degree which I simultaneously undertook during the course of this thesis, and his support in dealing with the Powers That Be to enable this crazy plan of mine to become a reality - it was well worth the effort! Similarly, I would also like to acknowledge the super folks in the Department of Mathematical Physics at NUI Maynooth for all their help and encouragement during that leg of my graduate student journey - in particular Professor Danny Heffernan and Professor Charles Nash.

I would also like to acknowledge the hospitality of Professor Rod Bartlett and the Quantum Theory Project during my very enjoyable stay at the University of Florida in sunny Gainesville, where some of this work was carried out. Thanks must go to Charles again for making this happen, and to the Trinity Trust for a travel award.

I would like to thank the denizens of Office 2.21/3 for all the coffee and stimulating conversations that made for such a pleasant working environment, and for their benevolent tolerance of my occasional musings on abstract topological nonsense. The same goes to the Luce Hall footballers for many an enjoyable kick-about which always brightened up a Friday.

To all my wonderful friends in Dublin for all the good times and moral support - it's been a privilege and a top laugh to hang out with you during my graduate student years.

Finally, to my parents - I couldn't have done it without your love and support, and it is to you that I dedicate this thesis.

Contents

List of Figures

List of Tables

Chapter 1

Introduction

The band theory of solids has been very successful in describing the electronic structure of many materials. Central to this philosophy is the notion that an uneven number of electrons in the unit cell results in metallic behaviour, arising from a partially filled band crossing the Fermi level. Very early on, however, it was pointed out by de Boer and Verwey that a variety of transition metal oxides that were predicted to be conductors by band theory were in fact insulators [1]. Mott and Peierls ascribed this anomaly to the role of strong electrostatic repulsion in these systems, favouring electron localisation around particular sites. This electron localisation often occurs due to repulsion between electrons in d- and f-orbitals.

The prototypical example of this breakdown of the single particle picture is nickel oxide. In 1949, Mott proposed a model for NiO as an insulator, where the energy gap which prevents conduction can be understood as arising from the competition between the Coulomb potential U between $3d$ electrons, and the transfer integral t of $3d$ electrons between neighbouring atoms. The total energy gap is given by $\Delta = U - 2zt$, where z is the number of nearest neighbour atoms. One of the simplest representations of the essential physics of such 'Mott' insulators is the well-known Hubbard model,

given by

$$H = - \sum_{<i,j>,\sigma} t_{ij} c^{\dagger}_{i\sigma} c_{j\sigma} + U \sum_{i} n_{i\uparrow} n_i \downarrow \tag{1.1}$$

The first term is a kinetic energy term representing the hopping of electrons from site i to site j. The second is the on-site Coulomb repulsion term, where $n_{i\sigma} = c^{\dagger}_{i\sigma} c_{i\sigma}$ is the number operator.

A further difficulty in obtaining a good theoretical description of many strongly correlated transition metal oxides is the competing energy scales present, beyond simply the strong Mott-Hubbard interaction U. The charge-transfer interaction U_{pd}, which is the energy cost for the transfer of an oxygen p electron to the neighbouring transition metal ion, can be sufficient to open a gap. Such systems are dubbed charge-transfer insulators in the classification scheme of Zaanen, Sawatsky and Allen[1]. In fact, photoemission studies point to NiO gap being of p-d character [3], thus making it a charge-transfer insulator in this scheme. Strong electronic coupling to lattice degrees of freedom can result in polaronic behaviour [4], a situation which will be examined further in this thesis when we investigate the Verwey transition in magnetite. The Hund's rule exchange interaction energy $U_{ex} = 2J_H$, defined as the energy needed to flip a d electron spin, may also play a key role in the conduction mechanism - such a term is central in mediating ferromagnetism in the double exchange model [5], which provides a first approximation to the physics of manganites like the half-doped bilayer $LaSr_2Mn_2O_7$ under study in this work.

As is well-known, the electronic structure of many strongly correlated transition metal oxides is inadequately described by traditional mean field ab-initio approaches such as Hartree-Fock (HF) and Density Functional The-

[1]The term 'Mott insulator' in this scheme is reserved for systems with a gap due to d-d electron correlation specifically. In the common lexicon, however, the term is used to describe any system which is predicted by band theory to be metallic but is insulating due to strong electron correlation, irrespective of the actual character of the band gap [2]. In this thesis, we will use the term 'Mott insulator' in this sense.

ory (DFT), as outlined in Chapter 2. The use of hybrid density functionals offers the prospect of a computationally cost effective means to improve the respective deficiencies present in HF and DFT, without recourse to many-body perturbative approaches, where the calculation of the electronic structure and lattice geometry optimisation is computationally prohibitive in all but the simplest unit cells.

In this thesis, we investigate two strongly correlated transition metal oxides exhibiting extremely rich physics due to the strong coupling of charge, spin, orbital and lattice degrees of freedom. The first is the well-known inverse spinel system magnetite, Fe_3O_4, which undergoes a metal-insulator and concurrent symmetry lowering structural phase transition at $T \simeq 125K$ from a cubic to monoclinic unit cell. This is known as the Verwey transition, and controversy has surrounded its exact mechanism since its discovery over 60 years ago [6]. Fe_3O_4 remains a hot topic of experimental and theoretical research with major questions outstanding, including the nature of charge/orbital ordering [7],[8], the low-temperature structural distortion [9], [10], [11] and the relative roles of electron-electron correlation [12] and electron-lattice coupling [13] in the Verwey transition mechanism. This work seeks to clarify these issues using a hybrid density functional approach.

The behaviour of Mott insulators when doped [2] can also present major theoretical and experimental challenges - perhaps none more spectacular than the high-temperature superconductivity seen in cuprates [14]. The combination of strong correlation and low-dimensionality in the high-T_c cuprates leads to novel forms of emergent order [15] across the phase diagram, including dynamic inhomogeneity [16] and the mysterious 'pseudogap' phase [17]. The colossal magnetoresistive manganites are another class of doped Mott insulator which possess a rich variety of orders as temperature and doping fraction are varied. Much research has been carried out into the physics of cubic manganites [18]; however the bilayer manganite series

$La_{2-2x}Sr_{1+2x}Mn_2O_7$ has remained less explored until recent years. This upsurge of interest has arisen due to the effective low-dimensionality of these bilayer compounds and their structural similarity to the superconducting cuprates, as well as their colossal magnetoresistive effect. We therefore focus on the bilayer manganite $LaSr_2Mn_2O_7$. The electronic structure and lattice geometry are investigated using hybrid DFT, and we find evidence of a pseudogap-like density of states brought about by reduced dimensionality in the 2d MnO_2 layers which are stacked perpendicular to the z-axis.

This thesis is organised as follows. In Chapter 2, an overview is given of the quantum many-body problem, and two widely adopted approximations, density funcional theory and Hartree-Fock theory, are outlined. Hybrid density functional theory is then introduced. The optimisation of crystal structures plays a crucial role in this work and the background and methodology of this tool is described. Chapter 3 gives an overview of the physics of magnetite and its famous Verwey transition, and plots a course through the enormous body of experimental and theoretical literature which has built up throughout almost 70 years of magnetite research. This provides a context for our subsequent extensive study of the electronic structure and lattice dynamics of the low-temperature monoclinic cell and high-temperature cubic cell of magnetite respectively. Band structures, density of states, charge and spin populations, charge density difference maps and optimised atomic coordinates are obtained for a range of values of Hartree-Fock exchange mixing and initial charge configurations. Finally, in Chapter 4, the electronic structure, crystal structure and magnetic ground state of $LaSr_2Mn_2O_7$ is subject to investigation using our hybrid density functional approach.

Chapter 2

Quantum Many-Body Theory

2.1 Introduction

In this work, we consider a system of N non-relativistic electrons. The equation of motion for an individual electron in the system is the single particle Schroedinger equation, which we write in time-dependent form.

$$\left(i\hbar\frac{\partial}{\partial t} - (H_0 + H_I)\right)\psi = 0 \tag{2.1}$$

Here H_0 denotes the free particle Hamiltonian and H_I accounts for interactions, whose form we have not yet specified. The states of the electron form a Hilbert space $\mathcal{H}$: the space of square integrable functions on $\mathbf{R}^3$. We can move to a many-particle picture by forming n-particle Hilbert spaces $\mathcal{H}^{\otimes n}$ under the operation of tensor product of single particle spaces. The collection of multiparticle states for all N generates a Hilbert space $\mathcal{F}$ called Fock space. We can define creation and annihilation operators[1] $a_{\mathbf{p}}^{\sigma\dagger}$ and $a_{\mathbf{p}}^{\sigma}$ on this space. Their action is to map between n-particle Hilbert spaces of different particle numbers in $\mathcal{F}$. This allows us to define Schroedinger field

[1] obeying fermionic anti-commutation relations

operators $\psi^\dagger = a_{\mathbf{k}}^{\sigma\dagger}\phi^*$ and $\psi = a_{\mathbf{k}}^{\sigma}\phi$, where ϕ can be a Bloch state in a crystal or a localised Wannier-like orbital in the tight-binding limit, of spin σ and momentum $\mathbf{k}$. Thus we may write down the two point correlation function for a single particle in the N-electron system.

$$iG(x,y) = \langle N|T\{\psi^\dagger(x)\psi(y)\}|N\rangle \tag{2.2}$$

$|N\rangle$is the exact N-electron ground state and $\psi^\dagger(x)$ is the field operator which creates an electron at $x = (\mathbf{r}, t)$, while $\psi(y)$ annihilates an electron at a time $(y = (\mathbf{r}', t')$. T is the time ordering operator:

$$T(O(t_1)O(t_2)) = \begin{array}{ll} O(t_1)O(t_2), & t_1 > t_2 \\ O(t_2)O(t_1), & t_2 > t_1 \end{array} \tag{2.3}$$

$iG(x,y)$ is in fact a Green's function of equation 2.1. The physical interpretation of the Green's function is as a *propagator*, i.e. the probability amplitude that, for $t' > t$, an electron added at $\mathbf{r}$ at time t will propagate to $\mathbf{r}'$ at time t' and that, for $t > t'$, a hole added at $\mathbf{r}'$ (electron removed) will propagate to $\mathbf{r}$.

Interactions

We now consider the exact form of interactions in the many-body system. These interactions will modify the many-particle ground state $|N\rangle$ and the form of the time-evolution operator $U(t,t')$ in the interaction picture. We consider a two-body Coulomb potential, written in field operator notation as

$$\hat{V} = \frac{1}{2}\int d^3r d^3r' \psi^\dagger(\mathbf{r})\psi^\dagger(\mathbf{r}')v_c(\mathbf{r}-\mathbf{r}')\psi(\mathbf{r}')\psi(\mathbf{r}) \tag{2.4}$$

This situation is well-described by Landau's Fermi Liquid theory, a phenomenological theory which can describe homogenous N-electron systems. The basic assumption of Landau theory is that the spectrum of the non-interacting Fermi gas may be deformed to the spectrum of an interacting

Fermi liquid by adiabatically switching on a weak interaction. Thus the excitations of the Fermi gas, electrons and holes, can be continuously deformed into so-called quasiparticles and quasiholes respectively. These quasiexcitations will have *renormalised* properties owing to the presence of interactions, such as an effective mass m^* which differs from the "bare" electron mass m by an amount proportional to the strength of the interaction. A physically intuitive way to think of this is of an individual electron being screened by a polarisation cloud as it repels neighbouring electrons. The incorporation of interactions introduces the energy-dependent self energy term $\Sigma(\mathbf{k}, \omega)$ which "dresses" the free particle propagator G_0 and contains all possible exchange-correlation interactions felt by the single electron. In an energy-momentum representation, the self-energy can be written

$$\Sigma(\mathbf{k}, \omega) = \Sigma'(\mathbf{k}, \omega) + i\Sigma''(\mathbf{k}, \omega) \tag{2.5}$$

Its real and imaginary parts contain all the information on energy renormalisation and quasiparticle lifetime, respectively, of an electron with band energy ϵ_k and wavevector $\mathbf{k}$. The Green's function expressed in terms of the electron self-energy is given by

$$\frac{1}{\omega - \epsilon_k - \Sigma(\mathbf{k}, \omega)} \tag{2.6}$$

A related quantity is the one-particle spectral function $A(\mathbf{k}, \omega) = A^+(\mathbf{k}, \omega) + A^-(\mathbf{k}, \omega)$. The two terms in the sum are the one-electron addition and removal spectra, which can be probed directly by inverse and direct photoemission spectroscopy respectively. The one-particle spectral function is related to the Green's function as follows:

$$A(\mathbf{k}, \omega) = -\frac{1}{\pi}\mathrm{Im}G(\mathbf{k}, \omega) \tag{2.7}$$

One such experimental technique, angle-resolved photoemission spectroscopy (ARPES), has emerged as a key technique for the study of 2-dimensional

doped Mott insulators [19] such as the bilayered colossal magnetoresistive manganites investigated in this thesis.

In general, the exact computation of the self-energy $\Sigma(\mathbf{k}, \omega)$ and the related one-particle spectral function is a formidable task, involving summation of an infinite series which includes products of Green's functions and self-energy insertions. This situation is represented diagrammatically in Figure 2.1. A useful first order approximation to the full self-energy is the Hartree-Fock self-energy. Hartree-Fock (HF) theory results from an expansion of the self-energy in terms of the bare Coulomb interaction $V_c(\mathbf{r} - \mathbf{r}')$. Thus higher order self-energy terms, corresponding for example to excitation of the electron hole pairs responsible for charge screening, are not taken into account at Hartree-Fock level. The HF self-energy will be purely real, since electrons in this single-particle theory do not feel the presence of other *individual* electrons[2], resulting in an infinite lifetime for Hartree-Fock 'quasiparticles'. In the next section, we will give a brief overview of how Hartree-Fock theory can be implemented numerically.

2.2 Hartree-Fock Theory

We consider the non-interacting N-electron problem. The equation of motion is

$$(\widehat{T} + \widehat{V}_{ext})\Psi = E\Psi \tag{2.8}$$

Here the Hamiltonian $\widehat{H}_0 = (\widehat{T} + \widehat{V}_{ext})$ accounts for one-particle kinetic energy and electron-nuclear potential energy $\widehat{V}_{ext}$ but does not account for electrons interacting with each other. The inter-electron interaction term

$$\widehat{V}_{ee} = \frac{1}{2} \sum_{i \neq j}^{N} \frac{1}{|\mathbf{r}_i - \mathbf{r}_j|} \tag{2.9}$$

introduces difficulties in that it couples the N one-electron orbitals ϕ_i into an N-electron wavefunction which is a function of $3N$ spatial coordinates

[2]Rather they move in an average so-called Hartree potential V_H

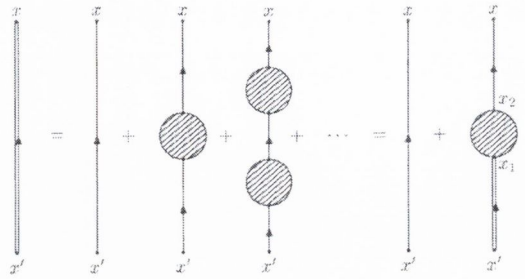

Figure 2.1: Diagrammatic representation of the interacting-particle propagator G (double line) in terms of the free-particle propagator G_0 (single line) and full electron self-energy Σ (hatched circle), i.e. the series of one particle irreducible diagrams. Such diagrams cannot be split in two by removing a single line.

$\mathbf{r}_i$ and N spin coordinates σ_i. The N-electron wavefunction in the position basis can be obtained from the N-electron Fock space state vector by

$$\langle x_1, \cdots, x_N | N \rangle = \Psi(x_1, \cdots, x_N) \tag{2.10}$$

This is normalised to one as shown:

$$\int dx_1 \cdots \int dx_N |\Psi(x_1, \cdots, x_N)|^2 = 1 \tag{2.11}$$

Here we write $x_i = (\mathbf{r}_i, \sigma_i)$. Without this Coulomb interaction, the N-electron wavefunction can be written as an antisymmetrized[3] Slater determinant of one-electron orbitals.

$$|\Phi_0\rangle = \begin{vmatrix} \phi_1(\mathbf{r}_1) & \phi_2(\mathbf{r}_1) & \cdots & \phi_N(\mathbf{r}_1) \\ \phi_1(\mathbf{r}_2) & \phi_2(\mathbf{r}_2) & \cdots & \phi_N(\mathbf{r}_2) \\ \phi_1(\mathbf{r}_3) & \phi_2(\mathbf{r}_3) & \cdots & \phi_N(\mathbf{r}_3) \\ \vdots & \vdots & \ddots & \vdots \\ \phi_1(\mathbf{r}_N) & \phi_2(\mathbf{r}_N) & \cdots & \phi_N(\mathbf{r}_N) \end{vmatrix} \tag{2.12}$$

[3]due to the Pauli exclusion principle for fermions

A set of one-particle Hartree-Fock eigenvalue equations can be obtained.

$$(\widehat{H}_0 + \widehat{V}_H)\phi_i + \int V_{ex,i}(\mathbf{r}, \mathbf{r}')\phi_i(\mathbf{r}')d\mathbf{r}' = E\phi_i(\mathbf{r}) \tag{2.13}$$

Here the full Coulomb repulsion term $\widehat{V}_{ee}$ is replaced by a mean-field Hartree potential V_H and corresponding exchange term V_{ex} to account for the Pauli exclusion principle for fermions. These terms are written explicitly as

$$V_H(\mathbf{r}) = \sum_{j\neq i}^{occ} \int \frac{n(\mathbf{r}')}{|\mathbf{r} - \mathbf{r}'|} d\mathbf{r}' \tag{2.14}$$

$$V_{ex,i}(\mathbf{r}, \mathbf{r}') = -\sum_{j\neq i}^{occ} \frac{\phi_j(\mathbf{r})\phi_j^*(\mathbf{r}')}{|\mathbf{r} - \mathbf{r}'|} \tag{2.15}$$

Here $n(\mathbf{r})$ is the electron density, which is given by

$$n(\mathbf{r}) = \sum_{i=1}^{N} |\phi_i(\mathbf{r})|^2 \tag{2.16}$$

This allows a self-consistent procedure to be numerically implemented: a trial guess is made of the non-interacting electron wavefunction $\tilde{\Psi}$, which can be decomposed into the sum of N one-electron orbitals. The one-electron Hartree-Fock equations are then solved. A new density is obtained from the new trial wavefunction, obtained by varying the linear expansion coefficients of the trial wavefunction. This process is repeated until the desired degree of convergence has been obtained.

2.3 Density Functional Theory

An alternative approach to the quantum many-body problem is afforded by the density functional theory. The central premise is that the interacting N-electron problem with electron density $n(\mathbf{r})$ can be mapped to a non-interacting problem with the same density $n(\mathbf{r})$. This fictitious system of non-interacting electrons is known as the Kohn-Sham system. Then the

one-electron Kohn-Sham orbitals ϕ_i may be described by the Kohn-Sham equations,

$$\{-\frac{1}{2}\nabla^2 + v_s(\mathbf{r})\}\phi_i(\mathbf{r}) = \epsilon_i\phi_i(\mathbf{r}) \tag{2.17}$$

with density given by equation 2.16. Here the subscript s denotes single-electron equations. The key shift in this viewpoint is the central point occupied by the density $n(\mathbf{r})$. This arises from the Hohenberg-Kohn Theorems [20]. The first of these demonstrates the existence of a one-to-one mapping between the ground state electron density and the ground state wavefunction of a many-particle system. The second HK theorem proves that the ground state density minimizes the total electronic energy of the system.

Now the ground state functional of an interacting system of density $n(\mathbf{r})$ can be written as a sum of terms

$$F[n] = T_s[n] + U[n] + E_{xc}[n] \tag{2.18}$$

Here $T_s[n]$ is the non-interacting kinetic energy functional, while $U[n]$ represents the Hartree-Fock energy, an exact form for which is known. The final term is the exchange-correlation functional $E_{xc}[n]$, accounting for all other electronic interaction energy beyond Hartree-Fock level. The second Hohenberg-Kohn theorem states that this functional is universal for density $n(\mathbf{r})$. However, an exact form for $E_{xc}[n]$ is in general unknown for a given system. Thus, an approximation for the exchange-correlation energy must be found.

The total energy for a given external potential $v_{ext}(\mathbf{r})$ is then given by the minimum of

$$E[n] = \min_n(F[n] + \int d^3r\ v_{ext}(\mathbf{r})\ n(\mathbf{r})) \tag{2.19}$$

This is equivalent to functional minimisation by means of the Euler-Lagrange equation

$$\frac{\delta F}{\delta n(\mathbf{r})} + v_{ext}(\mathbf{r}) = \mu \tag{2.20}$$

where $\mu = \partial E/\partial N$ is the chemical potential, and is a constant for constant particle number $N = \int d^3\ \mathbf{r} n(\mathbf{r})$.

The Kohn-Sham potential $v_s(\mathbf{r})$ for the non-interacting system is then

$$v_s(\mathbf{r}) = v_{ext}(\mathbf{r}) + v_{HF}(\mathbf{r}) + v_{xc}(\mathbf{r}) \tag{2.21}$$

with $v_{xc}(\mathbf{r}) = \delta E_{xc}[n(\mathbf{r})]/\delta n(\mathbf{r})$. Thus we know the unique Kohn-Sham potential felt by non-interacting electrons of the same density, given some approximation for v_{xc}. In fact, the exchange-correlation potential v_{xc} may be thought of roughly as a kind of DFT analogue to the electron self-energy Σ, albeit local and energy-independent, unlike the full non-local, energy-dependent electron self-energy $\Sigma(\mathbf{k}, \omega)$.

The first and most commonly used approximation for v_{xc} has been the local density approximation (LDA). This essentially assumes a uniform distribution of electronic density. It has a relatively straight-forward extension to spin-polarised systems by considering densities $n_\sigma(\mathbf{r})$ for electrons of spin σ. This is known as the local spin density approximation (LSDA).

Corrections to the local density approximation itself are mainly classified under the heading of gradient expansions. The idea is that, in order to take into account the charge inhomogeneity in the charge density of real systems, an expansion of a functional in gradients should increase accuracy:

$$A^{GEA}[n] = \int\ d^3r\ (a(n(\mathbf{r})) + b(n(\mathbf{r}))|\nabla n|^2 + \cdots) \tag{2.22}$$

The most well-known such method is the generalised gradient approximation (GGA) for the exchange-correlation functional. Semi-empirical approaches and fitting to small molecules have yielded popular GGA functionals such as the Becke exchange functional [21] and the Lee-Yang-Parr correlation functional [22].

However, if the Kohn-Sham equations for an insulator are solved using the LDA or GGA approximations for v_{xc}, the resulting Kohn-Sham band gap

Δ_{LDA}^{KS} is found to be too small by typically 40-50% in comparison with experiment [3]. This has particular ramifications for some strongly-correlated "Mott" insulators, such as the late transition metal monoxides, which are predicted to be metallic with DFT-LDA/GGA. These systems usually contain transition metal or with partially filled d shells. When applying a one-electron method with an orbital-independent potential like the LDA, one obtains a partially filled d band with metallic-type electronic structure and itinerant d electrons, often in total disagreement with the experimentally determined Mott insulating state due to localisation of d-electrons. A similar situation can arise with partially filled f-electron shells in rare-earth metal oxides.

Several attempts have been made to circumvent this difficulty. Self-interaction correction (SIC) methods try to account for the unphysical self-interaction of the electron which is known to occur in the LDA [23]. In exact DFT, only the highest occupied state is free from self-interaction, but LDA has general self-interaction for all states. This self-interaction is most significant for localised states; hence SIC reproduces quite well the localised nature of d or f states in transition metal and rare-earth compounds. However, SIC one-electron energies are frequently in strong disagreement with spectroscopic data.

Another popular approach to improve electronic structure calculations of transition metal oxides is the LSDA + U method [24]. Here the absence of LSDA orbital dependence is compensated by the addition of a so-called Hubbard U term, set to act only on localised d electrons. This splits the partially filled d band into lower and upper Hubbard bands and thus allows a band gap to be obtained. In practice, the separation of the electron states into two subsystems is carried out by choosing an orbital basis set for the partially filled d shell with density matrix ρ_d, which takes into account the exchange and Coulomb interactions for localised d-electrons. Thus the LSDA

$+ U$ functional will be of the general form

$$E^{LSDA+U}[n^\sigma, \rho^\sigma] = E^{LSDA}[n^\sigma] + E^U[\rho_d^\sigma] - E_{dc}[\rho^\sigma] \tag{2.23}$$

The final energy functional corrects for double counting of d-orbital exchange-correlation energy. In the absence of a specific d-orbital basis set, equation (2.23) should reduce to the normal LSDA. The parameters U and J must be chosen for the d-orbitals, thus adding an empirical element to the method. Recent work has focussed on calculating the Hubbard U term from first principles using some perturbative, frequency dependent method such as the random phase approximation [25], as used in the calculation of the screened interaction W in the GW approximation. Overall, LSDA + U has been quite successful in reproducing experimental results on strongly correlated transition metal oxides, though band structures can be unsatisfactory, while partially filled d bands in metallic transition metals will also be split, resulting in an unphysical insulating state for these systems.

The Hartree-Fock approach, which we previously discussed, is inherently self-interaction free, containing an explicit exchange term which cancels the self-interaction. Thus, unrestricted Hartree-Fock methods have been used for strongly correlated magnetic transition metal oxides and have successfully reproduced both the correct magnetic ordering and insulating ground state of various Mott insulators where DFT has failed e.g. in La_2CuO_4, the prototypical parent compound of the high-temperature superconducting cuprate series $La_{2-x}Sr_xCuO_4$ [26]. However, problems arise with using the bare Coulomb potential V featured in the non-local Hartree-Fock electron self-energy. In real systems, the bare Coulomb interaction felt by an electron would be screened by the overall charge density. Hartree-Fock theory's neglect of screening results in a pronounced ionic character and band gaps which are grossly overestimated, often a factor of 2-3 larger than experimental values [27]. The ionic bonding character also leads to underestimation of magnetic coupling constants [28]. This may be understood by appealing to

the Hubbard model for Mott insulating systems. The kinetic exchange mechanism in the Hubbard model gives magnetic coupling constant $J = t^2/U$, where t and U are the transfer integral and on-site Coulomb interaction. U will be large in the unscreened HF theory, leading to a small J.

The GW Method

The GW method [3] overcomes these problems by considering higher-order Feynman diagrams which account for screening of the bare Hartree-Fock exchange V_c, resulting in the screened interaction $W = \epsilon^{-1}V_c$ first considered by Hubbard. This screening occurs through the excitation of electron-hole pairs, which are non-interacting in the random phase approximation (RPA). The resulting electron self-energy $\Sigma(\mathbf{k}, \omega)$ in the GW approximation depends on both the frequency and wavevector of the electron, unlike in Hartree-Fock. This is written

$$\Sigma(x_1, t_1, x_2, t_2) = iG(x_1, t_1, x_2, t_2)W(x_1, t_1, x_2, t_2) \tag{2.24}$$

The frequency dependence of the screened interaction W is encoded in the inverse dielectric matrix $\epsilon^{-1}(\mathbf{k}, \omega)$. This response function must be first calculated using DFT or HF eigenfunctions, and the frequency dependence then must be tackled numerically, typically by means of computationally costly plasmon-pole or real space/imaginary time approaches. Herein lies the considerable computational overhead associated with the GW method. To date, there have been few GW studies on solids with structures more complex than simple transition metal monoxides and other diatomic compounds. These studies have focussed mainly on excitation energies in the form of quasiparticle band structures.

Hybrid Density Functionals

An accurate and cost effective compromise can be reached in the form of hybrid density functionals. This involves dealing with the self-interaction

problem in LSDA by mixing a Hartree-Fock exchange energy functional into the total LSDA energy functional. This makes use of the exact cancellation between Coulomb and exchange terms in Hartree-Fock theory and was first proposed for small molecules by Becke, based on the adiabatic connection formula for the exchange-correlation energy of the Kohn-Sham density [29]. Becke found that calculated ground state energies for a large range of molecules were greatly improved compared to LDA alone. Hybrid functionals were subsequently found to be significantly more reliable than the best GGA functionals for computing atomisation enthalpies [30], geometries and vibrational frequencies [31]. The most commonly used hybrid functional, similar to Becke's original scheme, is the B3LYP functional. This involves three parameters A, B and C fitted to thermochemical data - where B is the proportion of Becke's original exchange functional [29], C is the proportion the GGA correlation functional given by Lee, Yang and Parr [22] and $A = 20\%$ is the percentage of Hartree-Fock exchange mixing.

$$E_{xc}^{B3LYP} = (1-A)E_x^{Slater} + AE_x^{HF} + BE_x^{Becke} + CE_c^{LYP} + (1-C)E_c^{VNW} \tag{2.25}$$

The remaining terms in the above expression are E_x^{Slater}, the Dirac-Slater local exchange, and E_c^{VNW}, the local density approximation to the electron gas correlation functional, following the parameterisation of Vosko, Wilk and Nusair [32].

Surprisingly, this B3LYP hybrid functional is able to reproduce the thermochemistry of transitional metal-containing molecules, despite no transition metal compounds being used in the original data [33]. Despite its success in chemical physics, periodic solid state calculations using B3LYP have not appeared until relatively recently, due mainly to the difficulty in treating exchange and Coulomb series to a sufficiently high level of accuracy. Unlike LDA+U, which attempts to separate localised d-orbitals and applies a Hubbard U and J term to these orbitals only, the HF exchange mixing

is orbital independent in that it affects all Kohn-Sham orbitals in the DFT density functional. This B3LYP hybrid approach has yielded remarkably good band gap values in a variety of solids and insulators [34], including the Mott insulators MnO and NiO. Comparisons with comparable transitional metal monoxide calculations using GW [35],[36] show that in many instances the band gaps obtained with B3LYP [34] have errors of similar magnitude to GW when compared to experimental gap values. This is obtained at a fraction of the computational cost, and can be understood to arise from the characteristic Mott insulator band gap errors from Hartree-Fock and DFT cancelling each other out to some extent in B3LYP.

Thus, in GW, the bare Hartree-Fock interaction is dynamically screened by a charge density response function, the frequency and wavevector dependent inverse dielectric matrix $\epsilon^{-1}(\mathbf{k}, \omega)$, whereas in B3LYP, the bare Hartree-Fock interaction is reduced in a uniform, non-frequency dependent manner by mixing with the DFT energy functional. To date, there have been very few systematic direct comparisons of B3LYP and GW, or indeed of B3LYP and LDA+U. A comparative study on weakly correlated silicon [34] show good agreement between both methods and experiment. A similar study of the prototypical strongly correlated insulator NiO in its ferromagnetic phases show that the GW band structure based on B3LYP wave functions is quite similar to the parent B3LYP band structure [37],[38]. There is a 0.2 eV broadening of the gap, from 4.1 eV to 4.3 eV, while there are also relative shifts in the valence bands and a general upward shift in conduction bands. This latter work also suggests that hybrid functionals may be a better starting point for GW, since the calculation of the dielectric matrix used to obtain the screened interaction W involves the relative energies of valence and conduction bands obtained by a mean-field method such as DFT or HF.

In addition to band gaps, the addition of HF exchange into hybrid func-

tionals has successfully recovered the experimental ground state magnetic order in a range of strongly correlated transition metal oxides. Studies have been performed on the high T_c parent Mott insulator $CaCuO_2$ [39], the colossal magnetoresistive manganite parent Mott insulator $LaMnO_3$ [40], as well as a range of similar systems [28]. As we previously discussed, Hartree-Fock theory greatly underestimates magnetic coupling constants, while DFT overestimates. The above studies found that hybrid functionals with 35% Hartree-Fock mixing, as opposed to B3LYP's usual 20%, in fact produced magnetic coupling constants in closest agreement with empirically determined values, while continuing to maintain good agreement for band gaps.

In this thesis, we adopt a hybrid density functional scheme similar to the above, for a range of values of Hartree-Fock exchange. This is implemented in the CRYSTAL code [41]. In order to obtain eigenstates of the system, it is necessary to expand single electron wavefunctions over a set of pre-defined basis functions. CRYSTAL uses a basis of Gaussian-type orbitals of the general form

$$\chi^{GTF} = d_j e^{-\alpha|\mathbf{r}-\mathbf{A}|^2} = d_j e^{-\alpha r_{\mathbf{A}}^2} \tag{2.26}$$

where d_j is referred to as the contraction coefficient. Gaussian basis sets can provide an accurate description of electronic distribution in both valence and core states[4] and are generally relatively compact and computationally efficient. The quality of basis sets is a very important factor in determining whether self-consistent electronic structure calculations in CRYSTAL will converge to a stable energy minimum. There are a number of approaches available to optimise basis sets. We mention the inclusion of *polarisation* functions as an example. These are functions of higher angular quantum number than the highest occupied orbital of the system, which facilitate polarisation effects in the charge density. The inclusion of more basis functions can also aid convergence, though care must be taken to avoid linear

[4]plane wave basis sets can perform poorly for core states

dependence errors since Gaussian orbitals in general do not form a complete set.

2.4 Structure Optimisation

The determination of equilibrium structure is of primary importance in the modelling of chemical systems. Less research has been carried out into periodic systems due to the prohibitive computational cost. In this section, we will outline a modified conjugate gradient scheme, due to Schlegel [42], which allows atomic coordinates to be optimised in order to locate minima on the potential energy surface. This involves computing the matrix of second derivatives of the total potential energy with respect to atomic positions x^i.

The problem may be described as follows. We consider a unit cell with N atoms. The position of the i^{th} atom is described by the 3-dimensional position vector $\vec{r}_i$. Thus we have a $3N$-dimensional position vector X which describes any given atomic arrangement, in some $3N$-dimensional space S. Every possible set of atomic positions in the crystal can therefore be denoted by a vector X^a in S. The potential energy E is a function of $3N$ variables $x^{i\alpha}$, cycling over i atoms with coordinates $\alpha = 1, 2, 3$. Thus there is a $3N$-dimensional potential energy 'surface' (PES), any point on which describes the potential energy of the lattice for a given atomic arrangement. To find an equilibrium crystal structure, we wish to find the potential energy minima on the PES. This is an example of a general optimisation problem: given a function E of $3N$ variables $x_{i\alpha}$, we wish to find its minimum.

The conjugate gradient scheme of Schlegel [42] allows one to construct a series of steps leading to a stationary point of the potential energy E. Here we give a brief overview of the algorithm outlined in [42]. A stationary point is defined as a point where the $3N$-dimensional gradient vanishes, $g_i = dE/dx_i = 0$, yielding a gradient vector $\vec{G} = 0$. The first-derivative finds the stationary points on the PES, while second derivatives permit

their characterisation. Assume that p such steps have already been taken. At step $p+1$ we have the energy E and its gradient $\vec{G}^a$ at $(m+1)$ points $(0 \leq a \leq m \leq p)$. This information is arranged so that X^0 represents the current atomic positions, X^1 the most recent previous point, and so on, with X^m being the oldest. From the previous step, we also have the $n \times n$ matrix of second derivatives (called the Hessian matrix) of E, that is an approximation to the true Hessian $F_{ij} = d^2E/dx^i dx^j$.

An optimisation step consists of three parts. Firstly, the Hessian from the previous step is corrected. Then, a search is performed for a minimum between the current PES point and the previous point, i.e. in the direction $(X^a - X^0)$. Finally, using the Hessian matrix and minimum thus obtained, the next estimate of the location of the stationary point is given by

$$x_i^{new} = \tilde{x}_i - \sum_j F_{ij}^{-1} \tilde{g}_j$$

Here $\tilde{x}_i$ and $\tilde{g}_j$ are the position coordinates of the previous minimum, and that of its numerically obtained gradient g. Thus we see that gradients are evaluated every time the total energy is computed; the second derivative (Hessian) matrix is built from the gradients. At each step, a one-dimensional minimisation using a quadratic polynomial is carried out, followed by a $3N$-dimensional search using the Hessian.

If a negative eigenvalue is found, its sign is reversed. This forces a steepest descent step along the direction of the eigenvector possessing the negative eigenvalue. At each step, the gradient vector $\vec{G}^a$ and the displacement vector $X^{a+1} - X^a$ are tested against given tolerance levels for convergence. The root-mean-square gradient and displacement, as well as the absolute value of the largest component of each, must fall below their respective tolerance levels. If these four conditions are satisfied, the optimisation is considered complete. The above algorithm is implemented in parallel in the CRYSTAL03 code [41], and used in this work.

Phonon Modes

The Hessian matrix F_{ij} may also be used to obtain the vibrational eigenmodes of the crystal and their associated vibrational eigenfrequencies. This information on phonon modes can provide essential insight into physics of the system under study. We recall that if there are N atoms in the primitive cell, then there are $3N$ branches to the phonon dispersion relation: 3 acoustic branches (a longitudinal LA and two transverse TA), and $3N - 3$ optical branches, also split into longitudinal LO and tranverse TO modes. Thus for P primitive cells, the crystal will have a total of $3NP$ vibrational degrees of freedom.

Vibrational frequencies may be calculated at the Γ point of the Brillouin zone as follows. Using the Hessian F_{ij} as calculated above, the mass-weighted Hessian is calculated:

$$W_{\alpha i,\beta j}(\vec{q}=0) = \frac{F_{ij}}{\sqrt{M_\alpha M_\beta}}$$

M_α and M_β are the masses of atoms α and β associated with the i^{th} and j^{th} coordinates, respectively. The matrix $W_{\alpha i,\beta j}$ is then diagonalised to obtain eigenvalues (phonon mode frequencies) and eigenvectors (phonon mode atomic displacement vectors). Certain advantages accrue from calculations performed at the Γ point. $W(0)$ is simple to calculate from the expression above, and possesses the point symmetry of the crystal. In addition, the three acoustic modes, corresponding to translations at Γ, have zero frequency. This in fact should act as a check of the reliability of calculated results. Results for which the three acoustic modes show non-zero frequencies should be discarded. Lastly, it is the Γ point modes which give rise to the infrared and Raman spectra observed in experiments.

This computationally demanding process has been implemented in a beta version of the CRYSTAL06 code which we have adopted in this work. The transverse optical modes are calculated by default. Care must also

be taken to ensure that the initial crystal structure is at a minimum of the potential energy surface before vibrational calculations are carried out. This in effect entails attempting phonon calculations only on cell geometries which have already been converged and optimised to high accuracy, typically with tolerances governing the Coulomb and exchange integral convergence criteria set to 10^{-9} Hartree.

The hybrid density functionals used in this work have proven effective for equilibrium cell geometry optimisations [43]. The LDA and GGA alone suffer from such shortcomings as under- and overestimation of cell volumes.

Chapter 3

Magnetite

3.1 Introduction

Magnetite (Fe_3O_4) is the oldest known magnetic material, having been documented over 2500 years ago by the ancient Greeks. It has the largest net magnetization of all the naturally occurring minerals on Earth, and these magnetic properties led to magnetite, or lodestone, being used as an early form of magnetic compass. The remarkable physical properties of this material ensure that it continues to be of immense current interest. As a half-metal at room temperature, with an unusually high Curie temperature, magnetite is of technological interest as a potential source of spin-polarised electrons in spintronics applications [44]. Magnetite is also cited as a possible multiferroic material [45] - that is, a material which is simultaneously magnetic and ferroelectric, rendering it of considerable theoretical and practical importance. In addition, this system displays the (in)famous Verwey phase transition, the exact nature of which remains condensed matter physics' longest running controversy.

Magnetite has the formal ionic formula $Fe^{3+}[Fe^{2+}Fe^{3+}]O_4$. There are two inequivalent iron sublattices in the unit cell: the tetrahedrally coordinated A-sites and octahedral B-sites, yielding formal valence of +2.5 on the Fe_B

ions. This system undergoes a phase transition at $T_N = 860K$ from a paramagnetic to a ferrimagnetic state. At $T_V \simeq 125K$, the system undergoes another phase transition, characterised by a structural distortion and an abrupt decrease in conductivity by some two orders of magnitude. This class of transition is named after Eugene Verwey, who first discovered it in Fe_3O_4 in 1939 [6]. More generally, Fe_3O_4 has served as a prototype for many early studies of magnetism. Néel developed his theory of antiferromagnetism following studies on this system [46], while the nascent theory of metal-insulator transitions in strongly correlated systems received much impetus from observations of the Verwey transition, in particular the early studies of Mott and Peierls (see [47] and references therein).

Fe_3O_4 belongs to the class of spinel ferrites, as first determined by the early x-ray studies of Bragg [48, 49]. Such systems have the general formula AB_2O_4, with a cubic cell consisting of 32 close-packed oxygen ions, with 64 tetrahedrally coordinated A-type sites and 32 octahedral B-type sites. 8 of the A-sites are occupied by Fe^{2+} ions while 16 of the B-sites are occupied by Fe^{3+}. Observing the unusually high conductivity of this material above the metal-insulator transition, relative to similar spinels such as Co_3O_4 and Mn_3O_4[1], Verwey concluded that the correct arrangement of Fe ions was the *inverse* spinel structure, whereby the first octet of Fe^{3+} ions reside on the tetrahedral sites, while the second octet, along with the Fe^{2+} ions, reside on the 16 B-sites. This arrangement immediately suggests a simple conduction mechanism due to hopping of the 'extra' Fe^{2+} electron between closely spaced B-sites. This mechanism was used by Verwey in a schematic theory of a putative order-disorder transition, whereby the high temperature disordered metallic phase demonstrated conduction by the above channel, with the low-temperature insulating phase resulting from a localization of conduction electrons on the 8 B-sites. This localization was postulated to

[1] at around $10^3 < \Omega < 2.5 \times 10^4$ versus $\sim 10^{-5}\Omega^{-1}$ m $^{-1}$

lead to a mixed valence charge-ordered state, with a concomitant symmetry-lowering structural distortion from cubic to tetragonal. Such a scenario also allows for the possibility of so-called 'orbital order', a real space ordering of charge carriers in certain orbitals.

Very early on, however, questions were raised about the validity of the Verwey charge ordering model. Experimental studies often produced conflicting results, in no small part due to the poor quality of magnetite samples used in many early studies, and controversy still persists to the present day on the exact mechanism of the Verwey transition. In many respects, this could be considered the oldest unresolved question in condensed matter physics.

In the next section, we will outline the basic electronic structure of this material and discuss the influence of competing energy scales and strong electronic correlation on the macroscopic properties of this system. Strongly correlated systems such magnetite, as well as many other transition metal oxides such as the colossal magnetoresistive manganites and high-temperature superconducting cuprates, tend to order; this can occur in the spin, charge or orbital sectors and is a continuing hot topic of research in the physics of condensed matter. Hence magnetite provides us with a useful platform for the study of the general phenomenon of order in strongly correlated electron systems. We will also provide a brief overview of the development of experimental and theoretical research in magnetite physics, allowing us to identify the historical stumbling blocks which have contributed to the continued controversy over the exact mechanism of the Verwey transition since its discovery over 60 years ago. This will provide a context for our work and it is hoped that our hybrid HF/DFT calculations help to shed some light on this debate.

3.2 Basic Electronic Structure

It is instructive to have some heuristic picture of the basic electronic structure of this system. Thus we consider the configuration in terms of free Fe^{2+} and Fe^{3+} ions in the appropriate crystal environment. In this simple picture, the tetrahedral A-sites contain Fe^{3+} ions, yielding a d^5 electronic configuration. According to Hund's rules, though strictly valid only in the case of a free atom, this gives a singlet ${}^6S_{5/2}$ ground state term. The point group symmetry of the A-site is cubic; however, there is no crystal field splitting for the orbital singlet S ground state. There is also no spin-orbit splitting, since the the orbital moment is zero. Therefore, we have a spin-only ground state $S = 5/2$. A similar situation arises for the B-site Fe^{3+}.

In the case of the octet of Fe^{2+} ions on B-sites, Hund's rule filling yields a spin ground state of $S = 2$. The nearest neighbour oxygen octahedral field splits the ${}^5D_4$ ground state into triply degenerate t_{2g} levels and an excited state e_g doublet. This allows a possible t_{2g} orbital ordering to take place.

It is worth noting that the 5 d-electrons are arranged in a relatively high spin state when compared to some other well-known strongly correlated systems such as the high temperature superconducting cuprates, where a d^9 configuration on copper yields a spin of $S = 1/2$ per Cu ion[14]. This low spin state has the effect of making the system somewhat more "quantum" in nature [16].

3.3 Early Experiment

The literature on this long-running subject is encyclopedic; in this section, we give a brief overview of the relevant highlights pertinent to our research. Although a specific heat anomaly had been reported for magnetite as early as 1926 [50], it was Verwey who discovered the associated discontinuity in conductivity [6]. Verwey originally envisaged a specific ordering of the

octahedrally coordinated ions in the low-temperature phase, whereby these ions arrange in alternate $a/4$-spaced $\langle 100 \rangle$ planes, with homovalent ions forming chains along the $\langle 110 \rangle$ and $\langle \bar{1}10 \rangle$ directions as shown in Figure 3.1.

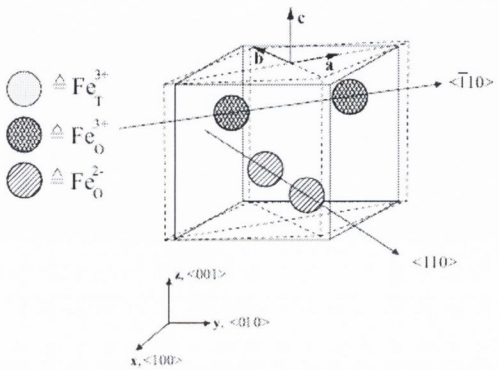

Figure 3.1: Originally proposed Verwey charge ordering scheme [8].

This charge ordering arrangement induces an orthorhombic distortion with respect to the high-temperature cubic cell. Such a crystal geometry should result in a (002) reflection visible by neutron diffraction. This reflection was detected by Hamilton in 1958 [51] using synthetic single crystals and applying a magnetic field to pick a spin orientation, thus counteracting multiple twinning effects. Such twinning effects can arise where a crystal has a mosaic of different cubic [001] axes for spin orientations, thus exhibiting overall isotropic behaviour. However, the same paper also reports experiments performed on natural crystals, which did not reveal any (002) reflection consistent with orthorhombic symmetry, though the author attributed this to the defects present in naturally occurring magnetite crystals.

Later neutron scattering studies by Shirane et al in 1975 [52] also failed to detect the (002) reflection, and suggested that it was merely an artefact resulting from simultaneous reflections. Their magnetic intensity distribution suggested alternate Fe^{2+} and Fe^{3+} in the ab-plane, in contrast to the Verwey model (Figure 3.1) of single modulation along the c-axis. Further

electronic and x-ray diffraction results revealed superlattice reflections inconsistent with orthorhombic symmetry, indicating that the low temperature cell is monoclinic, in contravention of the original Verwey charge ordering scheme.

Detailed neutron diffraction experiments on the low-temperature structure by Iizumi et al [9] in 1982 proposed a monoclinic Cc supercell of dimension $\sqrt{2}a \times \sqrt{2}a \times 2a$ relative to the high-temperature cubic cell. In these experiments, care was taken to check for spurious multiple twinning effects. Structural refinements were carried out using orthorhombic symmetry constraints on atomic positions. Besides proposing a Cc space group, the authors reported no significant variation in the mean Fe-O distances for the Fe B-sites, such as might accompany charge ordering. Iizumi's results also cast doubts on a previous conjectured charge ordering model due to Mizoguchi, which was derived on the basis of NMR measurements [53].

It seems that many early experimental studies of magnetite were plagued by the poor quality of samples employed. This stemmed in part from the widespread use of natural crystals, which suffer from an array of imperfections such as substitutional impurities, octahedral vacancies, dislocations and internal stresses. Also, many synthetically produced crystals did not follow present day standards of preparation and characterization, as discussed in the literature review of Walz [8]. This was evident, for example, from the reported Verwey transition temperatures T_V, which can act as a rough guide to characterise the actual quality of the magnetite crystals themselves. Such disparities in crystal quality may partially account for the many ambiguous and occasionally conflicting experimental results which strew the landscape of magnetite literature. An informative overview of the historic development of magnetite studies may be found in the review of Walz [8] and references therein.

3.4 Recent Experiment

X-Ray and Neutron Scattering

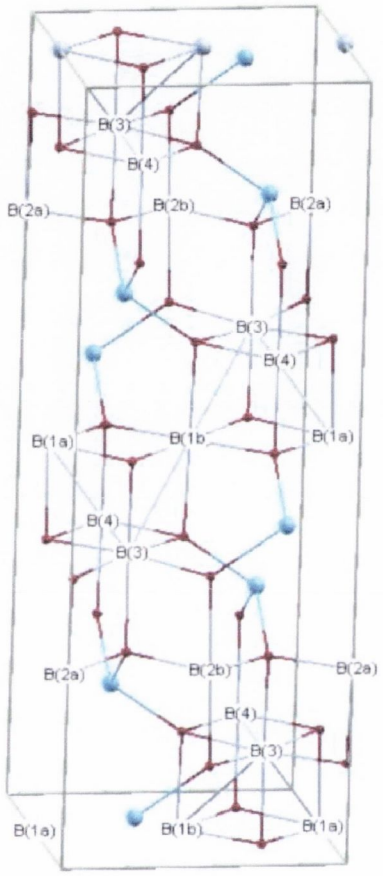

Figure 3.2: Fe_3O_4 low-temperature $P2/c$ cell. Octahedral Fe_B ions are labelled as shown. Tetrahedral Fe_A ions are coloured in cyan and oxygens are in red.

Recent high resolution x-ray and neutron diffraction data on highly stoichiometric powder samples by Wright et al [54] helped to reignite a flurry of interest in the question of charge ordering in magnetite. The use of such

powder samples can eliminate multiple twinning and negates the need to attempt their removal by the application of B-fields, such as in the earlier crystal studies of Iizumi [9]. However, some loss of resolution may occur in the obtained spectra, due to peak overlap. Structural refinements were carried out on the centric monoclinic $P2/c$ subcell, with atomic positions further constrained by orthorhombic $Pmca$ symmetry operations, similar to those of Iizumi [9]. This creates four inequivalent B sites (labelled $B1$-$B4$), each of which acts as an average over four sites in the full Cc supercell. This low-temperature $P2/c$ structure is shown in Figure 3.2

X-ray and neutron diffraction techniques can have difficulty directly distinguishing between Fe^{2+} and Fe^{3+} due to their nearly equal atomic scattering factors. The presence of charge ordering must therefore be inferred indirectly from Fe-O bond distances and associated bond valence sums (BVS). Bond valence sums provide a somewhat crude empirical chemical guide based on the principle that the bond length is approximately a unique function of bond valence [55]. Despite using the same symmetry constraints as the Iizumi study [9], Wright et al found, following structural refinement, that their refined parameters differed, leading to different values for the Fe-O bond distances. In fact, these authors found Fe-O bond lengths to be smaller for $B2$ and $B3$ as opposed to the $B1$ and $B4$ iron sites. They further claimed that the coincidence of these pairs of average Fe-O distances is not an artifact of the $Pmca$ symmetry constraints of the refinement [11].

Based on a BVS analysis, they conclude that partial long range charge ordering exists on B sites, with an estimated charge difference of 20% of that expected for ideal Fe^{2+} and Fe^{3+} states for the $P2/c$ cell. Given the fact that the $P2/c$ cell is averaged over 4 inequivalent subsites in the full Cc $\sqrt{2}a \times \sqrt{2}a \times 2a$ supercell, this configuration permits averaging over $4Fe^{2+}$ and $4Fe^{3+}$ subsites, or over ($3Fe^{2+}$ + Fe^{3+}) and (Fe^{2+} + $3Fe^{3+}$). The authors refer to these scenarios as class I and class II CO respectively,

yielding 20% charge disproportionation for class I and 40% for class II.

This view was once again challenged, this time by Garcia et al [56]. These authors carried out *x-ray resonant scattering* on two single crystals A and B, using the diffraction anomalous fine structure technique [7]. The atomic anomalous scattering factor and x-ray absorption coefficient depend on the chemical state of the scattered atom; hence a periodic arrangement of Fe^{2+} and Fe^{3+} should be revealed by different reflections in resonant x-ray scattering experiments. The authors probed the iron K edge of the forbidden (002) and (006) reflections, which in this instance are permitted by the anisotropy of the iron anomalous scattering factor [56]. They found no evidence of a charge ordered state above or below the Verwey transition temperature, on both highly stoichiometric and lower quality synthetic single crystals [7]. Further studies of (00 *odd*) and (00 *half-integer*) reflections revealed no resonances consistent with charge density modulation along the c-axis, either with the periodicity of the cubic or doubled cubic cell [57], leading this group to conclude that strong electron-phonon interaction, and not charge order, is the driving force for the Verwey transition. Our ab-initio results will show that both of these behaviours play a key role in the physics of this system.

Mössbauer Effect and Nuclear Magnetic Resonance

Nuclear magnetic resonance and Mössbauer techniques should be sensitive to different ionic valence states or crystallographic sites. Recent NMR studies [58] appear to confirm the low temperature monoclinic Cc structure, with 8 and 16 lines on A- and B-sites respectively. A doubly degenerate Fe_A line was detected below T_V, while Fe_B site lines were strongly mixed. This would indicate that integer charge order is not present in the low-temperature structure. More radically, recent Mössbauer studies under pressures of up to 12 GPa have led to the proposal of a coordination crossover scenario,

whereby charge density is shifted from B-sites to the tetrahedral A-sites at the Verwey transition [59]. This shift would cause the inverse spinel structure to change to a normal spinel arrangement, i.e.

$$[Fe^{3+}]_A[2Fe^{3+} + e^-]_B \longleftrightarrow [Fe^{2+}][Fe^{3+}Fe^{3+}]_B$$

The authors assert that this scenario would account for the apparent equivalence of Fe_B sites found in the study. A further x-ray diffraction study at different pressures by the same authors [10] found that the plot of metal-insulator transition temperature as a function of pressure $T_V(P)$ coincides with the curve of structural distortion temperature as a function of pressure $T_{dist}(P)$. From this, they conclude that the low temperature gap is associated with the particular electronic band structure resulting from the structural distortion. These authors therefore emphasize the role of electron-lattice coupling, as opposed to charge ordering, in opening up the band gap.

Optical Properties

Some debate also surrounds the question of whether the Verwey transition can be considered a true metal-insulator transition, or indeed if the high-temperature phase is actually metallic at all.

Photoemission spectroscopy (PES) by Chainani et al [61] on synthetic single crystals found a gap of 70 meV below T_V, which is half the activation energy obtained from electrical resistivity measurements ($E_a \sim 140$ meV), and which closes above T_V. Soon after, another PES study [62] concluded that the band gap is not in fact collapsed above T_V, but is reduced by ~ 50 meV, indicating a semiconductor-insulator transition.

A more recent soft x-ray photoemission study was carried out by Schrupp et al [60], using used radiation tuned to Fe $2p$-$3d$ resonance ($h\nu = 707.6$ eV). This allowed an enhanced probing depth of ~ 45 Å to be obtained so as to distinguish from purely surface effects. Such surface effects were shown

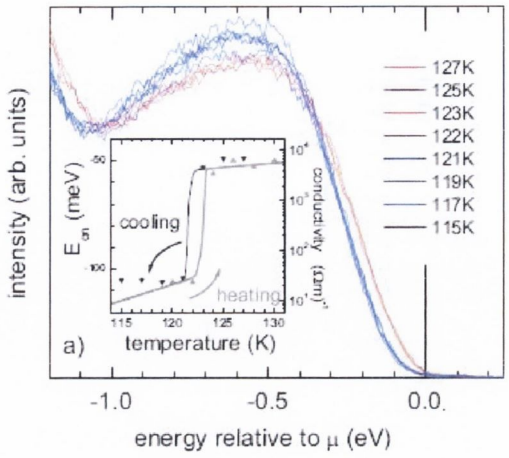

Figure 3.3: Fe_3O_4 soft x-ray photoemission spectra. Inset: spectral edge energy during cooling (down-triangles) and heating (up-triangles). From Schrupp et al [60].

to be significant when low-energy photoemission was used. Valence band spectra were obtained above and below the Verwey transition. The position of the chemical potential was calibrated by the Fermi edge of an evaporated gold film in electrical contact with the magnetite crystals. A gap was found in the low-temperature phase; above T_V the spectral edge becomes abruptly shifted towards the chemical potential. This discontinuous energy shift of the spectral edge energy at T_V can be seen in Figure 3.3. The authors pick a reference spectral edge energy, which they dub the spectral onset energy. This onset energy jumps exactly at T_V and is consistent with the hysteretic behaviour of the conductivity on both sides of the Verwey transition [8]. If the onset energy is identified with the insulator half-gap (i.e. the chemical potential μ is assumed to divide the band gap in half), its discontinuous change $\Delta E_{on} \approx 50$meV will cause the concentration of *thermally activated* charge carriers to increase by a factor of $\exp(\Delta E_{on}/k_B T_V)$. This would account for the observed two-orders magnitude jump in conductivity, as

already argued in the earlier photoemission study of Park [62]. Both of the PES studies therefore indicate a semiconductor-insulator transition. This points towards thermally activated conductivity above T_V.

As shown in Figure 3.3, no indication of a metallic Fermi edge or quasiparticle feature was observed in the high-temperature phase, in notable contrast to systems exhibiting the classical Mott metal-insulator transition, which display a prominent doublet of quasiparticle peak and lower Hubbard band. The valence band spectra showed exponential suppression of spectral weight towards the chemical potential at all temperatures investigated. This spectral feature was attributed to strong electron-phonon coupling, and the formation of small polarons, i.e. electron (or hole) excitations dressed by virtual phonons, was advanced as a possible cause. The theoretical notion of polaronic quasiparticles in Fe_3O_4 has been around for some time, stemming from the work of Chakraverty [63], Yamada [64] and Mott [65].

PES measures transitions to the Fermi level, whereas infrared spectroscopy measures an optically allowed transition from one electronic band to another across the Fermi level. Optical conductivity measurements obtained a gap value of 140 meV below T_V [66], consistent with some previous PES and activation energy experiments. Terahertz and infrared conductivity measurements [67] in the insulating state found a power-law frequency dependence for the low-frequency dynamic conductivity ($\sigma_1 \propto \nu^s$ with $s \sim 1.3$), which is a characteristic feature of hopping conduction between localised states [68]. An unexpected result of this study was the abrupt change of the dielectric constant at T_V, even yielding negative values above T_V. Along with the conductivity spectra, these results indicate the formation of a narrow band of quasi-free carriers that contain only a small part of the spectral weight. Our density of states calculations show a narrow band below T_V corresponding to localisation of electrons in a particular d-orbital on one of the two Fe B-sites in an Fe_3O_4 unit. Our structure op-

timisation show that this band is strongly coupled to the surrouding Fe-O octahedral lattice, suggesting polaronic behaviour.

Gasparov et al [69] carried out infrared and Raman measurements. It was found that the Verwey transition manifests itself in both infrared and Raman spectrum as the temperature is lowered through T_V. In the Raman spectrum, one can see at least 17 new modes about T_V. Optical conductivity data in the same study found a gap-like feature below T_V which could be attributed to a polaronic picture, where carriers below T_V are localised polarons leading to a strong polaron peak in the optical spectrum. Above T_V, some carriers are delocalised, leading to a peak broadening and reduction in oscillator strength.

The above experiments point to the influence of the electron-lattice interaction in magnetite physics. This picture is in agreement with early theoretical proposals advanced by Ihle and Lorentz [13]. In the Mott picture of the Verwey transition [65], the charge carriers are either polarons or bipolarons. Above T_V, the system is described as a Wigner glass, a system where the carriers are localized by disorder-induced random-field potentials. When the temperature is raised, some of the polarons dissociate, leading to a hopping type of conductivity. By contrast, a model Hamiltonian of Cullen and Callen [12] considered the role of electron correlation to be central and did not consider phonons. This model envisaged magnetite as a crystal of Fe_B^{3+} ions with an 'extra' Fe electron hopping between them. Our results show that both the electron-electron correlation and the electron-lattice interaction play a central role in creating a lattice distortion and opening a gap at the Verwey transition.

3.5 Low Temperature Phase Results

So what is the net outcome of this perhaps somewhat bewildering array of experimental results - and what is the present paradigm for magnetite and

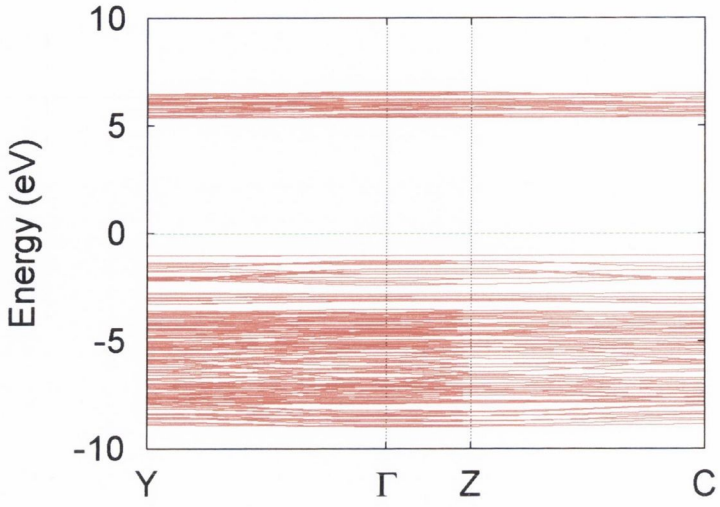

Figure 3.4: $P2/c$ cell majority-spin electronic band structure at 50% exchange.

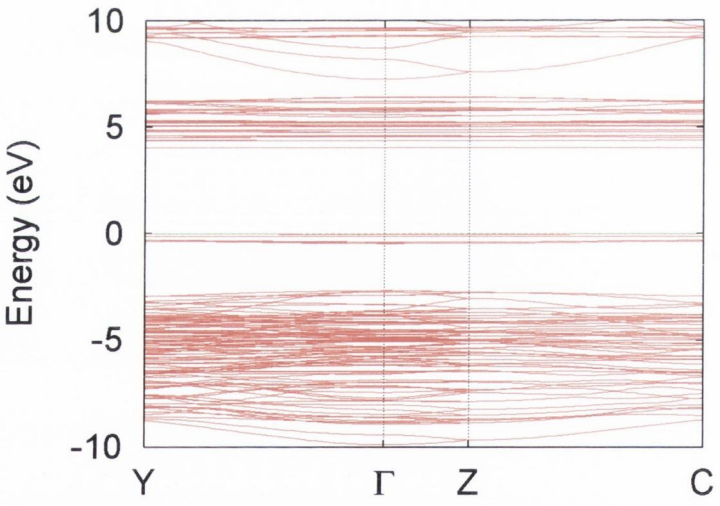

Figure 3.5: $P2/c$ cell minority-spin electronic band structure at 50% exchange.

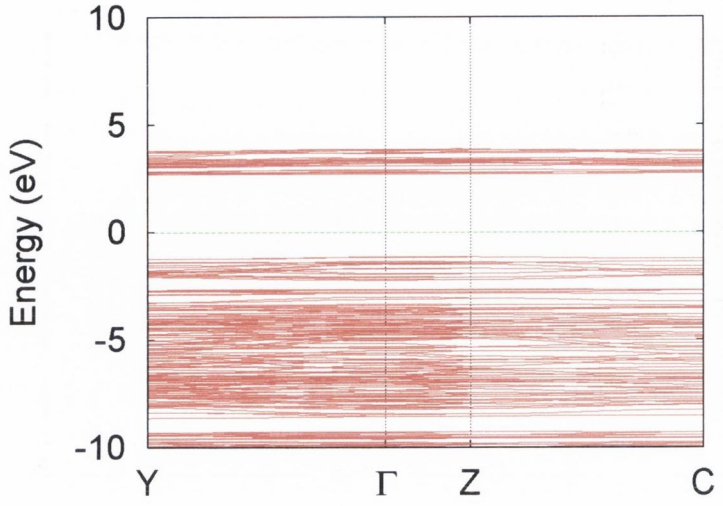

Figure 3.6: $P2/c$ cell majority-spin electronic band structure at 30% exchange.

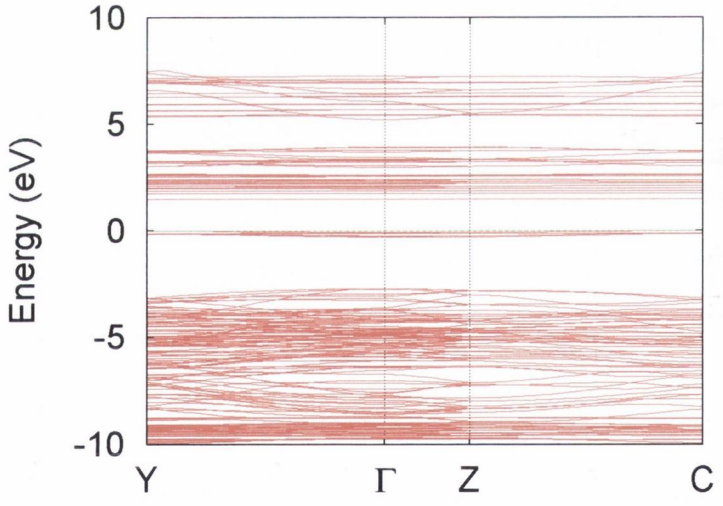

Figure 3.7: $P2/c$ cell minority-spin electronic band structure at 30% exchange.

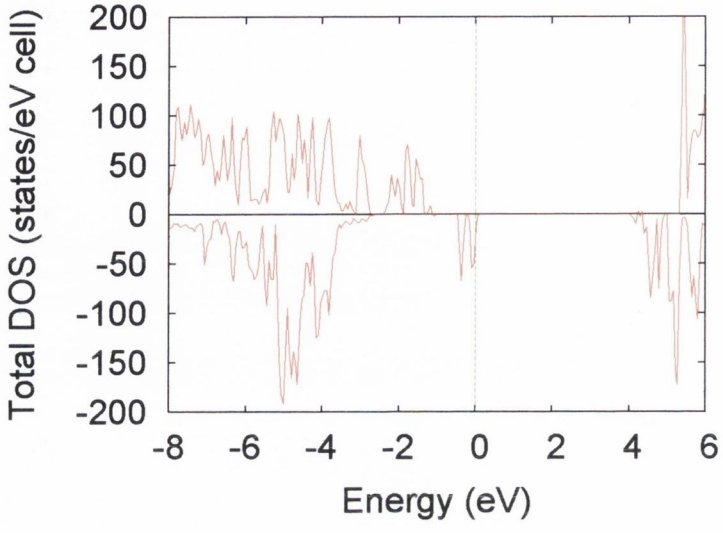

Figure 3.8: $P2/c$ cell total density of states at 50% exchange.

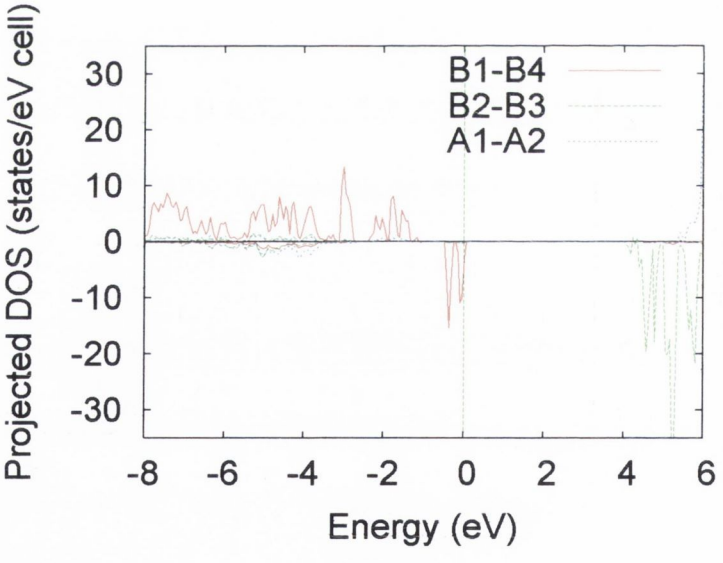

Figure 3.9: $P2/c$ cell projected density of states at 50% exchange.

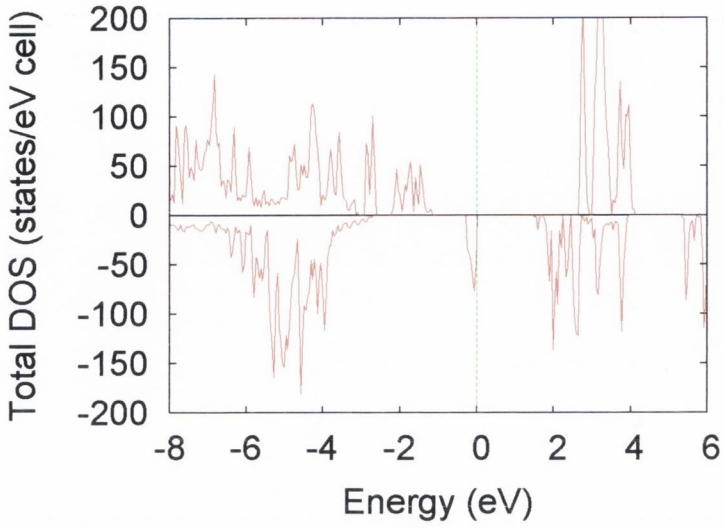

Figure 3.10: $P2/c$ cell total density of states at 30% exchange.

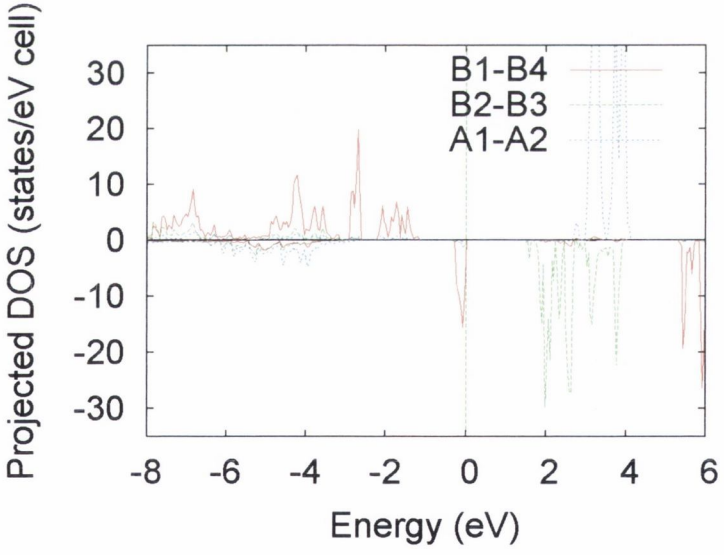

Figure 3.11: $P2/c$ cell projected density of states at 30% exchange.

Table 3.1: 3*d*-shell charge and spin populations at 50% HF exchange.

Atom	Initial valence	Final valence	Initial spin/ μ_B	Final spin/ μ_B
A(1)	5	5.59	-5	-4.40
A(2)	5	5.59	-5	-4.40
B(1)	6	6.11	4	3.81
B(2)	5	5.54	5	4.49
B(3)	5	5.56	5	4.46
B(4)	6	6.11	4	3.81

Table 3.2: 3*d*-shell charge and spin populations at 30% HF exchange.

Atom	Initial valence	Final valence	Initial spin/ μ_B	Final spin/ μ_B
A(1)	5	5.73	-5	-4.24
A(2)	5	5.73	-5	-4.24
B(1)	5.5	6.10	4.5	3.78
B(2)	5.5	5.66	4.5	4.34
B(3)	5.5	5.71	4.5	4.28
B(4)	5.5	6.13	4.5	3.74

Table 3.3: 3*d*-shell charge and spin populations for structure optimised low-temperature cell at 50% exchange.

Atom	Initial valence	Final valence	Initial spin/ μ_B	Final spin/ μ_B
A(1)	5.59	5.59	-4.24	-4.24
A(2)	5.59	5.59	-4.24	-4.24
B(1)	6.11	6.11	3.78	3.76
B(2)	5.54	5.54	4.34	4.34
B(3)	5.56	5.55	4.28	4.31
B(4)	6.11	6.11	3.74	3.75

Table 3.4: 3*d*-shell charge and spin populations for structure optimised low-temperature cell at 30% exchange.

Atom	Initial valence	Final valence	Initial spin/ μ_B	Final spin/ μ_B
A(1)	5.73	5.72	-4.25	-4.25
A(2)	5.73	5.72	-4.25	-4.25
B(1)	6.10	6.12	3.77	3.77
B(2)	5.66	5.66	4.35	4.36
B(3)	5.71	5.68	4.29	4.32
B(4)	6.13	6.13	3.76	3.76

its Verwey transition? Accurate ab-initio calculations are clearly needed in order to cast light on the subject. Our hybrid HF/DFT and structure optimisation approach allows us to gauge the relative effects of both on-site electrostatic repulsion and electron-lattice coupling on the charge-orbital order and band gap in magnetite. Thus we can disentangle these effects and examine the relative contributions of these competing degrees of freedom to the Verwey transition mechanism.

We begin by analyzing the electronic structure of the low-temperature cell with Hartree-Fock exchange mixing set to 50%. Figures 3.4 and 3.5 show electronic band structures for the experimentally determined $P2/c$ cell [11]. A minority band gap of ~ 4.0 eV is found. The bands around the gap are of predominantly *d*-*d* character, indicating Mott insulating behaviour. They show very little dispersion, indicating that charge is significantly localised below T_V. Figure 3.8 is a plot of the total electronic density of states, displaying the 4.0 eV gap in the minority (spin-down) spin channel. The Fermi energy has been scaled to 0 eV. We have projected the DOS onto pairs of Fe ions in Figure 3.9. A comparison with the total DOS shows that the gap results from charge localisation on the $B1$ and $B4$ atoms just below the Fermi level, with a gap to hopping of electrons onto the $B2$ and $B3$ sites.

Table 3.5: Fe-O bond lengths for the $P2/c$ and optimised structures with mean values for AO_4 tetrahedra and BO_6 octahedra shown.

Bond	Expt. Length[11] (Å)	50% optimised (Å)	30% optimised
A(1)-O(1)	1.898(4)	1.916	1.910
A(1)-O(5a)	1.875(2)	1.854	1.864
A(1)-O(5b)	1.882(2)	1.873	1.877
A(1)-O(2)	1.890(4)	1.913	1.908
⟨A(1)-O⟩	1.886(3)	1.889	1.890
A(2)-O(4)	1.913(5)	1.925	1.923
A(2)-O(6)	1.870(2)	1.859	1.860
A(2)-O(6)	1.877(2)	1.861	1.861
A(2)-O(3)	1.899(5)	1.912	1.911
⟨A(2)-O⟩	1.890(4)	1.891	1.889
B(1)-O(1) ×2	2.042(3)	2.059	2.053
B(1)-O(6) ×2	2.091(3)	2.159	2.148
B(1)-O(2) ×2	2.082(3)	2.134	2.129
⟨B(1)-O⟩	2.072(3)	2.117	2.110
B(2)-O(5) ×2	2.052(3)	2.027	2.026
B(2)-O(4) ×2	2.040(3)	2.004	2.013
B(2)-O(3) ×2	2.038(4)	1.986	1.993
⟨B(2)-O⟩	2.043(3)	2.006	2.011
B(3)-O(5) ×2	2.092(3)	2.036	2.046
B(3)-O(6) ×2	2.018(3)	1.979	1.981
B(3)-O(2)	1.964(5)	1.951	1.952
B(3)-O(3)	2.116(5)	2.072	2.084
⟨B(3)-O⟩	2.050(4)	2.009	2.015
B(4)-O(5) ×2	2.094(3)	2.126	2.122
B(4)-O(6) ×2	2.053(3)	2.097	2.098
B(4)-O(1)	2.033(5)	2.049	2.044
B(4)-O(4)	2.086(5)	2.153	2.135
⟨B(4)-O⟩	2.069(4)	2.108	2.103

Table 3.6: Fe-Fe bond lengths for the $P2/c$ and optimised structures

Bond	Expt Length (Å)	50% optimised (Å)	30% optimised
B(1a)-B(1b)	2.972	2.972	2.972
B(1a)-B(3)	2.864	2.941	2.919
B(1a)-B(4)	2.958	2.933	2.947
B(1b)-B(3)	2.855	2.931	2.909
B(1b)-B(4)	2.950	2.922	2.936

Reducing the percentage of Hartree-Fock exchange mixing in the density functional to 30% results in a reduced bare Coulomb potential, substantially shrinking the minority gap by around 60% to $\sim$ 1.60 eV on the total DOS plot (Fig. 3.10). Another result of interest can be seen by comparing the band structures. Not only is the overall charge gap altered by varying the amount of exchange screening, but the *relative* position of bands is also affected, as seen for example in the dispersive conduction bands between Y and Z. This demonstrates that certain electronic bands are more influenced by reduction in HF exchange mixing than others, and is reminiscent of a GW study of the prototypical strongly correlated antiferromagnetic insulator, NiO [70]. In that work, dynamical screening of the bare HF exchange through the GW approach led to shifts of the unoccupied d-bands, to such an extent that the qualitative band gap character was altered from $d-d$ (Mott-like) to $d-s$. This relative band shift therefore lends some credence to the notion of B3LYP as a poor man's GW [71]. The magnitude of the band gap decrease going from 50% to 30% is also quite large relative to a previous B3LYP study of NiO [72]. In that study, a larger reduction of HF exchange from 50% to 20% decreased the gap by a half.

The question of charge order is clearly of key importance for this material. Tables 3.1 and 3.4 show calculated Mulliken charge and spin populations for Fe ions in the unit cell, at 50% and 30% exchange respectively. We

Table 3.7: Fractional atomic coordinates for optimised structure at 50% exchange. Experimental structures are taken from Wright [11] and Iizumi [9] (italics)

			Experimental		50% optimised	
Atom	x	y	z	x	y	z
A(1)	1/4	0.0034(4)	0.06366(7)	0.24931	0.0052	0.06357
		0.0049(3)	*0.0635(1)*			
A(2)	1/4	0.5061(2)	0.18867(8)	0.25022	0.4915	0.18876
		0.5067(2)	*0.1887(1)*			
B(1a)	0	1/2	0	0	1/2	0
B(1b)	1/2	1/2	0	1/2	1/2	0
B(2a)	0	0.0096(3)	1/4	0	0.0072	1/4
		0.0099(3)				
B(2b)	1/2	0.0096(3)	1/4	1/2	0.0071	1/4
		0.0099(3)				
B(3)	1/4	0.2659(2)	0.38010(9)	0.25027	0.24953	0.37771
		0.2643(4)	*0.3789(1)*			
B(4)	1/4	0.7520(2)	0.37659(9)	0.25030	0.74441	0.37691
		0.7549(5)	*0.3746(2)*			
O(1)	1/4	0.2637(7)	-0.0023(3)	0.24985	0.2592	-0.00095
		0.2630(6)	*-0.0027(2)*			
O(2)	1/4	0.7461(6)	-0.0029(3)	0.25008	0.757862	-0.00601
		0.7477(6)	*-0.0009(2)*			
O(3)	1/4	0.2447(8)	0.2542(3)	0.24992	0.225122	0.25451
		0.2461(7)	*0.2450(2)*			
O(4)	1/4	0.7738(8)	0.2525(3)	1/4	0.7659	0.248777
		0.7696(6)	*0.2427(2)*			
O(5a)	-0.0091(4)	0.0095(6)	0.1277(2)	-0.008479	0.007535	0.13173
	-0.0116(6)	*0.0089(3)*	*0.1295(2)*			
O(5b)	0.4909(4)	0.0095(6)	0.3723(2)	0.49207	0.0076474	0.36822
	0.4884(6)	*0.0089(3)*	*0.3705(2)*			
O(6a)	-0.0081(4)	0.5046(6)	0.1246(2)	-0.012790	0.483012	0.12848
	-0.0067(6)	*0.5050(3)*	*0.1244(1)*			
O(6b)	0.4919(4)	0.5046(6)	0.3754(2)	0.487659	0.483145	0.37145
	0.4933(6)	*0.5050(3)*	*0.3756(1)*			

Table 3.8: Fractional atomic coordinates for optimised structure at 30% exchange. Experimental structures are taken from Wright [11] and Iizumi (italics) [9]

			Experimental		30% optimised	
Atom	x	y	z	x	y	z
A(1)	1/4	0.0034(4)	0.06366(7)	0.24922	0.00638	0.06361
		0.0049(3)	*0.0635(1)*			
A(2)	1/4	0.5061(2)	0.18867(8)	0.25029	0.49579	0.18873
		0.5067(2)	*0.1887(1)*			
B(1a)	0	1/2	0	0	1/2	0
B(1b)	1/2	1/2	0	1/2	1/2	0
B(2a)	0	0.0096(3)	1/4	0	-0.00204	1/4
		0.0099(3)				
B(2b)	1/2	0.0096(3)	1/4	1/2	-0.00202	1/4
		0.0099(3)				
B(3)	1/4	0.2659(2)	0.38010(9)	0.25032	0.2538	0.37849
		0.2643(4)	*0.3789(1)*			
B(4)	1/4	0.7520(2)	0.37659(9)	0.25029	0.74744	0.37648
		0.7549(5)	*0.3746(2)*			
O(1)	1/4	0.2637(7)	-0.0023(3)	0.24997	0.26087	-0.00169
		0.2630(6)	*-0.0027(2)*			
O(2)	1/4	0.7461(6)	-0.0029(3)	0.25011	0.75786	-0.00601
		0.7477(6)	*-0.0009(2)*			
O(3)	1/4	0.2447(8)	0.2542(3)	0.24987	0.2301	0.25454
		0.2461(7)	*0.2450(2)*			
O(4)	1/4	0.7738(8)	0.2525(3)	1/4	0.768736	0.24941
		0.7696(6)	*0.2427(2)*			
O(5a)	-0.0091(4)	0.0095(6)	0.1277(2)	0.00841	0.00967	0.13129
	-0.0116(6)	*0.0089(3)*	*0.1295(2)*			
O(5b)	0.4909(4)	0.0095(6)	0.3723(2)	0.49228	0.009843	0.36863
	0.4884(6)	*0.0089(3)*	*0.3705(2)*			
O(6a)	-0.0081(4)	0.5046(6)	0.1246(2)	-0.01749	0.4865	0.1279
	-0.0067(6)	*0.5050(3)*	*0.1244(1)*			
O(6b)	0.4919(4)	0.5046(6)	0.3754(2)	0.48851	0.48682	0.37199
	0.4933(6)	*0.5050(3)*	*0.3756(1)*			

find that partial charge ordering exists on Fe B1 and B4 sites. At 50%, deep in the insulating regime, the charge disproportionation between $B1$-$B4$ and $B2$-$B3$ sites is of order $\sim 0.5e$ or 50% of the expected value for ideal Fe^{2+} and Fe^{3+} states. This reduces to $\sim 0.4e$ as the HF exchange is decreased. We also find a greater accumulation of charge on Fe sites, which may be explained as follows. Unrestricted Hartree-Fock methods tend towards the ionic limit due to the large unscreened Coulomb interaction. The uniform reduction of this interaction, through increased mixing of DFT exchange-correlation in the hybrid DFT energy fuctional, leads to an increasingly covalent wavefunction character. Overall there is a general transfer of charge from oxygen ions to metal ions, with oxygen populations typically around $-1.5e$ and $-1.4e$ for the 50% and 30% cases respectively, in contrast to the ideal ionic values of $-2e$. There is also an associated spin ordering, with a magnetic moment disproportionation of $\sim 0.7\mu_B$ and $0.5\mu_B$ between $B1$-$B4$ and $B2$-$B3$ sites. The extra spin density is in the spin-down state, in agreement with a heuristic Hund's rule treatment for the free Fe^{2+} ion. Thus we can conclude that, in the $P2/c$ structure, varying the degree of electronic correlation has an appreciable effect on the band gap but not on the partial $B1$-$B4$ charge ordering scheme, which remains fairly robust.

The B-site charge ordering arrangement corresponds to class-I CO in the classification scheme of Wright et al [54] described in Section 3.4. The magnitude of charge disproportion published by those authors is 20%, derived from structural data using bond valence sums, though the accuracy of this empirical approach has been questioned as we have previously elaborated [57]. We confirm the presence of a $[001]_c$ charge density modulation on the B-site lattice[2], characterised by alternate electron-rich Fe_{B1} planes and electron-poor Fe_{B2} planes, separated by planes containing chains of Fe_{B3}

[2]The 'c' subscript indicates that the Miller indices are taken with respect to the high temperature cubic cell, rather than the low temperature $P2/c$ cell which is doubled along the z-axis.

and Fe_{B4} (see Figure 3.2). These chains contain both electron rich and electron-poor ions and hence are considered charge neutral in the overall charge modulation (Tables 3.1 and 3.2). The chains also cause a secondary $[00\frac{1}{2}]_c$ charge modulation on the B-site lattice due to the interchanged positions of ions at $z = 3/8$ and $z = 5/8$ with respect to the $P2/c$ cell[3]. This picture contrasts with the original Verwey proposal which saw a simple arrangement of (001) planes alternately occupied by Fe^{2+} and Fe^{3+} B-site cations, as shown previously in Figure 3.1.

Our results also confirm that the well-known Anderson criterion for minimal electrostatic repulsion is violated in Fe_3O_4 [73]. This qualitative condition was first advanced for systems with the spinel structure in 1956 and has long been considered a prerequisite requirement when determining the exact CO scheme. It may be explained as follows. If we consider the B-site lattice in Fig. 3.2, it can be seen that B-sites form corner-sharing tetrahedra. If we consider this lattice to consist of N Fe^{3+} ions, then there will be $N/2$ extra electrons to make up the Fe^{2+} sites. The nearest neighbour electrostatic energy is minimised at $U = e^2/d_{Fe-Fe}$, with d_{Fe-Fe} representing the interionic distance, when each tetrahedron contains two of the extra electrons, giving two Fe^{2+} and two Fe^{3+} ions. For the $P2/c$ unit cell, this would imply that the extra charge resides on the $B1$ and $B2$ ions, in contradiction to our findings of electron rich $B1$ and $B4$ sites.

Recently, other ab-initio studies have appeared using Wright's experimentally determined $P2/c$ crystal structure, as highlighted in Table 3.9. Self-interaction corrected local spin density approximation (SIC-LSDA) calculations were performed by Szotek et al [74]. These authors considered the Verwey charge order scenario, and two other scenarios whereby all Fe sites are 2+ or 3+ respectively. This meant that in these latter cases, the unit

[3]corresponding to the $[00\frac{1}{2}]$ positions on the high-temperature cubic cell, see Figure 7(a) of Ref. [11]

cell was not charge neutral. The third scenario (all Fe^{3+}) emerged as the lowest energy solution; however the Fe charge populations appear questionable. Total charge disproportionation in the region of 0.5 - 0.6e was found, as shown in Table 3.9. Possible objections to these results could include the fact that the minimal basis set and atomic sphere approximation used for the potential could make the total energies unreliable. A second objection could be that one must choose a set of localised states for which the SIC is applied. The actual ground state will only be found if it is among those tested [75].

The LDA+U studies by Jeng et al[76] and Leonov et al[77] use the values of $U = 4.5$ eV and 5 eV respectively, with exchange parameters $J = 0.89$ eV and $J = 1$ eV, originally derived in the context of earlier ab-initio calculations on the high-temperature cubic cell[78]. It is not clear which oxidation state of Fe was used in the calculation of these parameters. Madsen et al[75] use $U - J = 6.33$ eV for Fe_A^{3+} and $U - J = 6.21$ eV for $Fe_B^{2.5+}$, considerably larger than the $U - J = 3.61$ eV and 4 eV used in the first two LDA + U studies. Jeng found a gap of 0.2 eV, while Leonov reported a gap of 0.18 eV, in contrast to our 1.6 eV gap for 30% HF exchange. Published LDA+U charge populations are shown in Table 3.9. In all instances, a partial $B1-B4$ charge ordering scheme was obtained, in agreement with our hybrid DFT results. Furthermore, Leonov et al state that this CO configuration is arrived at regardless of initial charge arrangement, again in agreement with our findings for the $P2/c$ cell. Our results show a slightly greater degree of charge disproportionation between electron-rich and electron-deficient Fe_B sites, though this may be a function of the increased electrostatic repulsion in our calculations, as manifested in our larger band gap. The most remarkable difference between our 30% and 50% results and the LDA+U is perhaps the higher charge populations that we find on the Fe sites. As previously noted, our Fe charge populations become higher as the system becomes in-

creasingly covalent, i.e. moving from 50% to 30% HF exchange. The absence of orbital dependence in the LDA exchange-correlation potential means that the mixed HF exchange should act on all orbitals in our hybrid density functional scheme. The LDA+U method, on the other hand, incorporates an orbital-dependent potential U acting only on localised d-electrons, and which neglects oxygen p-electrons. This may have some bearing on the LDA+U populations reported by these authors.

Table 3.9: Fe $3d$-shell charge populations from published calculations. δ is the band gap in eV.

Atom	B3LYP30	LDA+U_1[76]	LDA+U_2[77]	LDA+U_3[75]	SIC-LDA[74]
A(1)	5.73	-	-	5.37	6.56
A(2)	5.73	-	-	5.38	6.56
B(1)	6.10	5.57	6.04	5.61	7.74
B(2)	5.66	5.41	5.73	5.33	7.45
B(3)	5.71	5.44	5.92	5.39	7.15
B(4)	6.13	5.58	6.03	5.58	7.35
δ/eV	1.6	0.2	0.14	0.0	0.35

Interestingly, we find substantial transfer of charge to the tetrahedral A-sites, of the order of $0.7e$ at 30%. This contrasts markedly with the simple Verwey picture, whereby A-sites are trivalent and are hypothesized to be uninvolved in any charge ordering mechanism for the Verwey transition. There is some precedent for this in the literature; Mössbauer spectroscopy [59] found a transfer of charge to Fe_A ions at the Verwey transition, as we discussed in Section 3.4. This led to the proposal of a coordination crossover scenario at T_V, with Fe_A^{2+}-sites and Fe_B^{3+}-sites, thus ruling out B-site charge order. Our detailed ab-initio calculations find therefore that A-sites are not trivalent below T_V, and are indeed closer to the 2+ ideal state proposed in this Mössbauer study. However, our results definitely do not support

these authors' subsequent interpretation of their results as yielding all Fe^{3+} B-sites. For some reason, most of these LDA+U studies do not give their calculated A-site populations so we cannot make a comparison in every case, though Madsen et al show Fe_A at $\sim +5.4$ valence, in close agreement with their low-charge B-site values and in disagreement with the traditional Fe_A trivalent picture.

The question then arises as to the exact orbital-resolved charge and spin populations. We find that Fe_3O_4 is in fact orbital ordered. This ordering takes place on the $B1$ and $B4$ ions due to the extra charge density on these ions preferentially filling a particular d-orbital. We find that the t_{2g} orbitals are favoured. In the $P2/c$ frame, the Fe_{B1} charge is greatest on the d_{xz} and d_{yz} orbitals, with occupation numbers of $1.60e$ ($1.66e$) and $1.28e$ ($1.26e$) respectively, at 30% (50%) exchange. There is also clear orbital ordering on the Fe_{B4} ions, with orbitally-resolved occupation numbers greatest for the $d_{x^2-y^2}$ at $1.68e$ ($1.62e$), with d_{yz} at $1.27e$ ($1.35e$). The largest difference between the most populated Fe_B^{2+} orbital and the corresponding Fe_B^{3+} orbital is $0.54e$ ($0.58e$) for Fe_{B1} and $0.63e$ ($0.58e$) for Fe_{B4}. This is very similar to the magnitude of the total B-site charge disproportionation, previously found to be $0.4e$ - $0.5e$.

Figure 3.12 shows a three-dimensional charge density difference plot of the $B(1a)$-$B(1b)$-$B(1a)$ ion chain. This plot is obtained by taking our calculated charge density and subtracting a superposition of individual atomic charge densities. Thus, any preferential orbital filling will be visible in the 3d plot. Neighbouring B-site d-orbital lobes are rotated around the z-axis with respect to one another. Relative to the $P2/c$ axes shown, these $B1$-site orbitals correspond to a mixture of d_{xz} and d_{yz}, with neighbouring sites rotated around the z-axis with respect to one another. Figure 3.13 shows the $B3$ and $B4$ charge density difference plots from the same perspective, while Figure 3.14 shows the same plot looking down on the yz-plane. This corre-

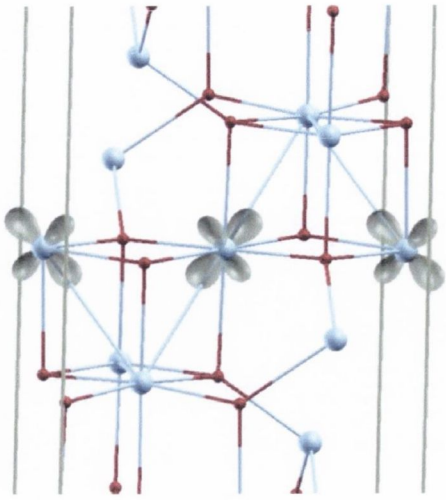

Figure 3.12: $P2/c$ cell charge density difference plot, showing orbital order along a $B(1a)$-$B(1b)$-$B(1a)$ chain. Calculated at 50% HF exchange mixing.

sponds to a predominantly $d_{x^2-y^2} \pm d_{xz}$ orbital ordering on the $B4$ Fe ions, with respect to the $P2/c$ crystal axes. With an appropriate rotation of local axes with respect of Fe B-site octahedra, the orbitals shown correspond to the three t_{2g} orbitals, d_{xz} and d_{yz} on $B1$, and d_{xy} on $B4$. Our results therefore demonstrate so-called "antiferro-orbital" ordering in magnetite, due to the orthogonal position of neighbouring B-site orbitals on orbital ordered sites.

3.5.1 Structure Optimisation

The question of the exact low-temperature crystal structure of magnetite has been central to the debate on the Verwey transition in magnetite since its first discovery. As we have previously described, x-ray and neutron diffraction experiments on the structure have been central to the controversy over charge ordering [11], [56]. Clearly, the exact crystal structure has significant implications for the Verwey transition. We propose to bridge the divide

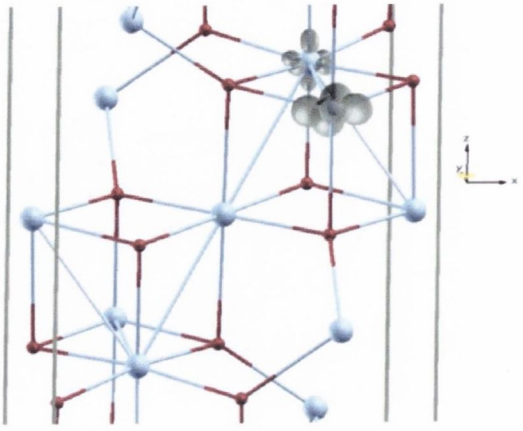

Figure 3.13: $P2/c$ cell charge density difference plot, showing orbital order on Fe $B4$. Calculated at 50% HF exchange mixing.

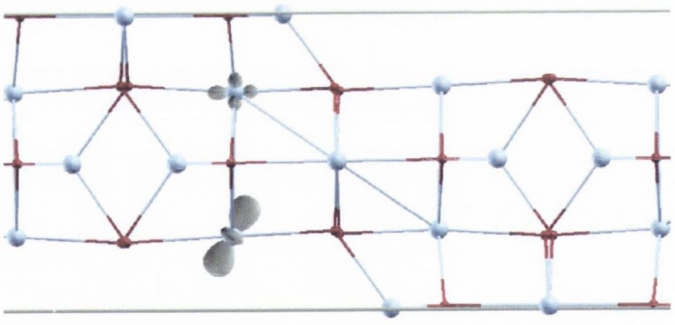

Figure 3.14: $B4$ site orbital order, yz-plane view, at 50% HF exchange mixing.

between experiment and theory by performing equilibrium structure optimisations, starting from Wright's experimentally proposed $P2/c$ structure [11]. A conjugate gradient algorithm is adopted in order to locate minima and saddle points on the potential energy surface (PES), as implemented in the CRYSTAL program[41] and discussed in Chapter 2. The matrix of first derivatives of the force, the Jacobian, permits identification of saddle points on the PES, while the Hessian matrix of second derivatives allows for their characterisation. We have carried out structure optimisations using the final wavefunctions obtained from our 30% and 50% self-consistent solutions, and beginning with the experimental $P2/c$ crystal structure of Wright et al [11].

The argument given by Wright et al for the existence of charge order is based on the structural distortion which occurs at the Verwey transition. This distortion leads to distinct metal sites with significantly differing mean distances to the surrounding anions. Experimental values of Fe-O distances at 90K are listed in Table 3.5. Distances for our optimised structure are also listed, calculated at 50% and 30% HF exchange. The first thing to notice is the expansion of the electron-rich BO_6 octahedra centred on $B1$ and $B4$ sites, with a corresponding contraction of Fe-O bond lengths in the $B2$- and $B3$-centred octahedra. This lattice distortion is less pronounced as the exchange becomes reduced, i.e. moving to the 30% case. Fe-Fe bond lengths are shown in Table 3.6. It is interesting to note that the lattice distortion follows the pattern of orbital order that we have previously discerned. $B1$-$B3$ bond lengths are visibly expanded along the orientation of d-orbital lobes (Fig. 3.12). We also note that relaxing the unit cell has virtually no effect on the magnitude of charge disproportionation in the low-temperature cell (Table 3.3). This is similar to a previous hybrid HF/DFT study of another strongly correlated magnetic oxide, the half-doped manganite $La_{0.5}Ca_{0.5}MnO_3$ [71], where it was found that optimisation of the crystal lattice had little effect on the emergence of a Zener polaron

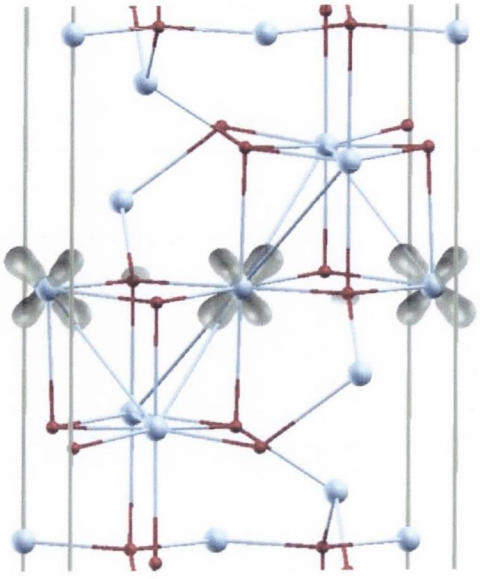

Figure 3.15: $B1$-site orbital order on optimised $P2/c$ structure.

ground state at high values of HF exchange. Since optimisation has little effect on charge ordering, it is therefore reasonable to conjecture that the orbital order is also unaffected by the optimisation, and indeed we find this to be the case, as shown in Fig. 3.15. Fe_{B1} largest occupation numbers are now $1.66e$ on d_{xz} and $1.24e$ on d_{yz}, with Fe_{B4} at $d_{x^2-y^2} = 1.67e$ and $d_{yz} = 1.29e$, at 30% exchange.

In addition, the question of the effect of lattice distortion on the band gap clearly has important ramifications for the mechanism of the Verwey transition and deserves further investigation. Fig. 3.16 shows a density of states plot for the 30% structure-optimised cell. The gap has opened up to $\sim$ 2.2eV from its original value of $\sim$ 1.6eV before optimisation (Fig. 3.10), a substantial increase of almost 40%. This result shows the critical role of strong electron coupling to the lattice in opening up a gap, and strongly suggests that this is a driving force behind the Verwey transition.

Atomic coordinates for the optimised structure are shown in Table 3.7.

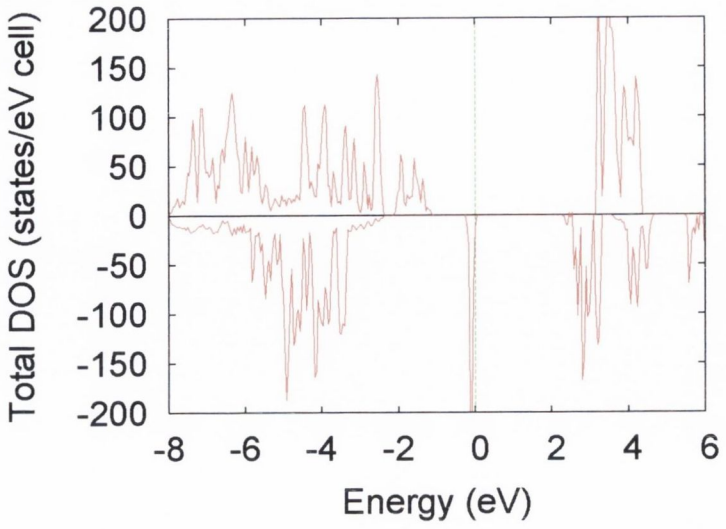

Figure 3.16: Total Density of States for optimised $P2/c$ structure.

We have used the Isotropy code [79] to determine the space group corresponding to these new atomic positions. Interestingly, for the 30% case, we find that the structure retains $P2/c$ symmetry. For the 50% study, we find that the optimised cell also has $P2/c$ symmetry, pointing to good experimental resolution of the structure in the study of Wright et al [11].

In order to ascertain the robustness of the ordering arrangement and ensure that we have not introduced a bias in our choice of initial charge configuration, we have performed the same calculations starting at all Fe B-sites having initial charge +2.5 and with the A-sites at +3. We found very similar results, indicating that our $P2/c$ cell calculations arrive at the same results independent of the starting point.

3.6 High Temperature Phase Results

For $T > T_V$, Fe_3O_4 has a face-centred cubic crystal structure with space group $Fd\bar{3}m$, with a symmetry-lowering structural distortion to a mono-

clinic cell at $T = T_V$. The high-temperature cubic cell consists of 2 formula units, and therefore contains 2 symmetry-equivalent Fe A-sites and 4 symmetry-equivalent Fe B-sites. The exact interplay of electronic and lattice dynamics at the transition point clearly requires further elucidation. We have therefore carried out extensive calculations of the electronic and equilibrium crystal structure of cubic magnetite, starting with the $T > T_V$ experimental structure reported by Wright et al [11]. Our calculations span a range of values of Hartree-Fock exchange, thus enabling us to approach the Verwey transition point from either side (insulating or metallic), and allowing a picture of general trends to develop. A comparison with our low-temperature $P2/c$ results is made and a number of key parallels and differences are shown to emerge.

3.6.1 $Fd\bar{3}m$ 30%

30% exchange yields a minority gap of 0.31 eV, as shown in the band structure and DOS plots (Figs. 3.17, 3.18 and 3.19). This provides an interesting case because we are now in the insulating regime, at the cusp of half-metallicity. It would be interesting to see whether charge order develops in this hypothetical case, for the following reason. The central difficulties inherent in understanding the Verwey transition result from the appearance of both a band gap (with possible charge-ordering) and a structural distortion at the transition point. From an experimental perspective, it is difficult to separate these effects. Our calculations allow us the scope to investigate separately the effects of electronic correlation (by varying HF exchange) and electron-lattice coupling (by structure optimisation).

The cubic unit cell has two formula units. We have therefore labelled the four B-sites in this doubled unit cell as B_a, B_b, B_c and B_d for clarity in the ensuing discussion. This is to avoid confusion with our previous notation for the low-temperature cell, where $B1$ to $B4$ Fe sites were unique by symmetry

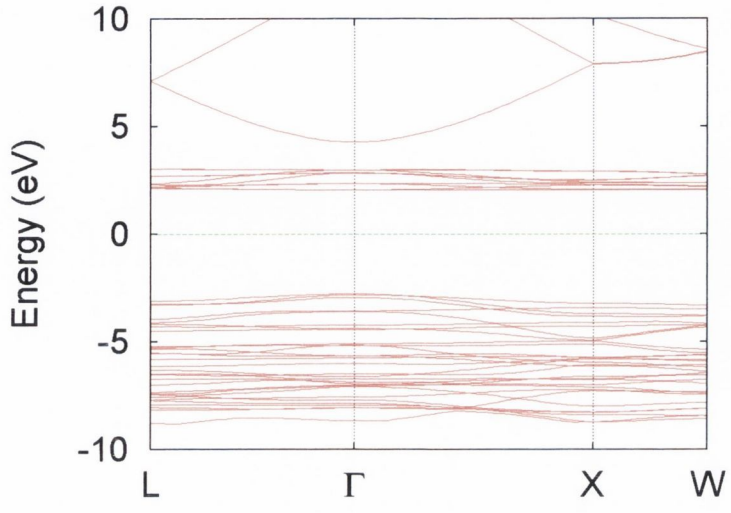

Figure 3.17: $Fd\bar{3}m$ cell majority spin band structure at 30% exchange.

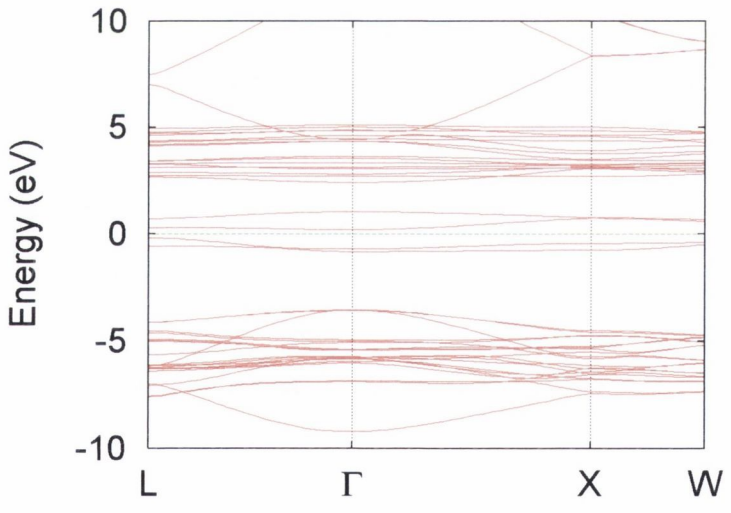

Figure 3.18: $Fd\bar{3}m$ cell minority spin band structure at 30% exchange.

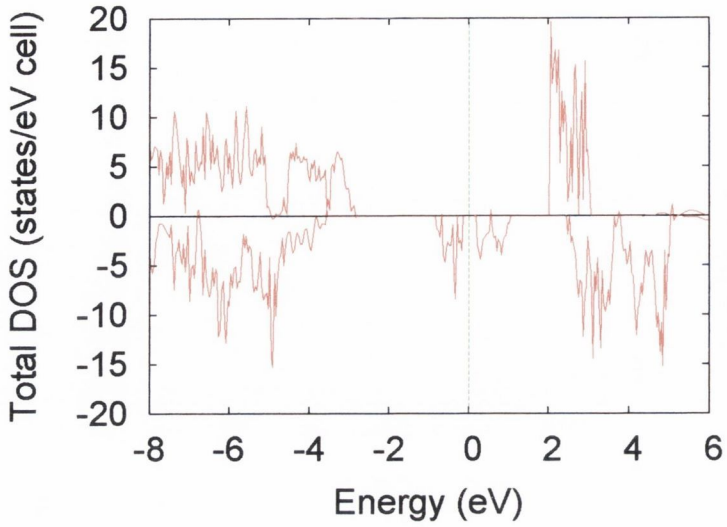

Figure 3.19: $Fd\bar{3}m$ cell total density of states at 30% exchange.

Initial	A	B_a	B_b	B_c	B_d
B_aB_d	5.82	5.96	5.96	5.95	5.95
B_bB_c	5.82	5.96	5.96	5.96	5.96
B_bB_d	5.82	5.92	5.98	5.95	5.97
$B\_B\_$	5.83	6.18	6.18	5.77	5.77

Table 3.10: 3d-shell charge populations for $Fd\bar{3}m$ cell at 30% exchange.

Initial	A	B_a	B_b	B_c	B_d
B_aB_d	-4.27	4.08	4.09	4.09	4.09
B_bB_c	-4.27	4.09	4.09	4.08	4.09
B_bB_d	-4.27	4.13	4.05	4.09	4.07
$B\_B\_$	-4.25	3.76	3.76	4.32	4.34

Table 3.11: 3d-shell spin populations for $Fd\bar{3}m$ cell at 30% exchange.

to the $P2/c$ space group. It should be borne in mind, of course, that the four cubic cell Fe_B sites are space group symmetry-equivalent, unlike the four inequivalent B sites in the $P2/c$ cell. Tables 3.10 and 3.11 show the results for charge and spin populations. The results differ from our previous low-temperature cell results in several respects. We label our solutions based on which pair of sites is assigned as 2+ and which pair is 3+ in the *input* to the calculation, e.g. B_aB_d means a starting point of Fe^{2+} on ions B_a and B_d. We find it necessary to make this distinction since it will be shown that results are not always independent of initial conditions for the high-temperature cell, in contrast to our findings for the low-temperature structure.

By starting from an integer charge ordered configuration, we end up arriving at a non-CO ground state of almost integer Fe^{2+} B-site cations. The Fe_A sites, at $Fe^{2.18+}$, are clearly much closer to divalence than the traditional trivalent Verwey picture. Though we only show charge populations for fully converged calculations, this trend of non-CO was found for all initial charge ordered inputs at 30%, regardless of which B-sites were chosen as integer charge ordered. This lack of dependence on initial charge configuration is reminiscent of the low-temperature monoclinic cell, where it was found that $B1$-$B4$ CO resulted regardless of initial conditions. The B_aB_d and B_bB_c solutions are practically degenerate, differing by < 2 meV per formula unit. The B_bB_d solution shows negligible charge disproportionation of less than $0.06e$, and this arrangement is in fact around 10 meV/fu higher in energy.

However, this is not the full story, since the lowest energy solution is in fact the charge ordered one, obtained from a charge neutral starting point (labelled $B\_B\_$). We find that this solution is lower than the lowest energy non-CO arrangement by ~ 265 meV/fu. Thus we have obtained a charge ordered insulating ground state even *without* the Verwey structural distortion, and only Coulomb repulsion, sufficient to create a 0.31 eV gap. The corresponding $P2/c$ monoclinic cell with the same degree of Coulombic repulsion

(at 30% exchange) shows a 1.6 eV gap, clearly demonstrating the central role of the lattice distortion in widening the band gap. We previously discovered this trend with our $P2/c$ cell structure optimisations. A comparison with the Mulliken populations for the high and low temperature insulating cells shows the population and degree of charge disproportionation ($\sim 0.4e$) to be almost the same in each case. Thus, CO is energetically favourable over non-CO states in the insulating regime, irrespective of lattice distortions, which in fact serve to increase the band gap. In addition, the $P2/c$ distortion lowers the unit cell's total energy by a further 10 meV/fu.

As we have seen, orbital order in the $P2/c$ cell correlates with the lattice distortion around OO sites. It would be interesting to see whether such order accompanies charge order in the undistorted cubic insulating cell. To this end, we investigate the orbital occupation numbers of this solution, and find that orbital ordering, of predominantly $d_{xz} + d_{yz}$ character, exists on the both charge ordered (B_b and B_c) Fe ions. Specifically, we find occupation numbers of $n_b^{d_{xz}} = 1.31$, $n_b^{d_{yz}} = 1.55$ and $n_c^{d_{xz}} = 1.41$, $n_c^{d_{yz}} = 1.44$. This represents a $0.44e$ and a $0.36e$ orbital occupation disproportionation, respectively, compared with the least occupied ($d_{3z^2-r^2}$) e_g orbital on each ion. This situation is represented graphically in a charge density difference plot (Fig. 3.20). We can see that this $d_{xz} \pm d_{yz}$-like OO corresponds to orbitals rotated almost orthogonally with respect to each other around the z-axis. The OO sites are seen to line up in a chain pointing in the $\langle 110 \rangle$ direction, with non-OO sites aligned in $\langle \bar{1}10 \rangle$ chains. This in fact very similar to Verwey's originally proposed charge ordering scheme. In that model, he proposed that Fe^{2+} and Fe^{3+} chains occur in precisely this alignment, in what he assumed was a tetragonally distorted unit cell below T_V (see Figure 3.1).

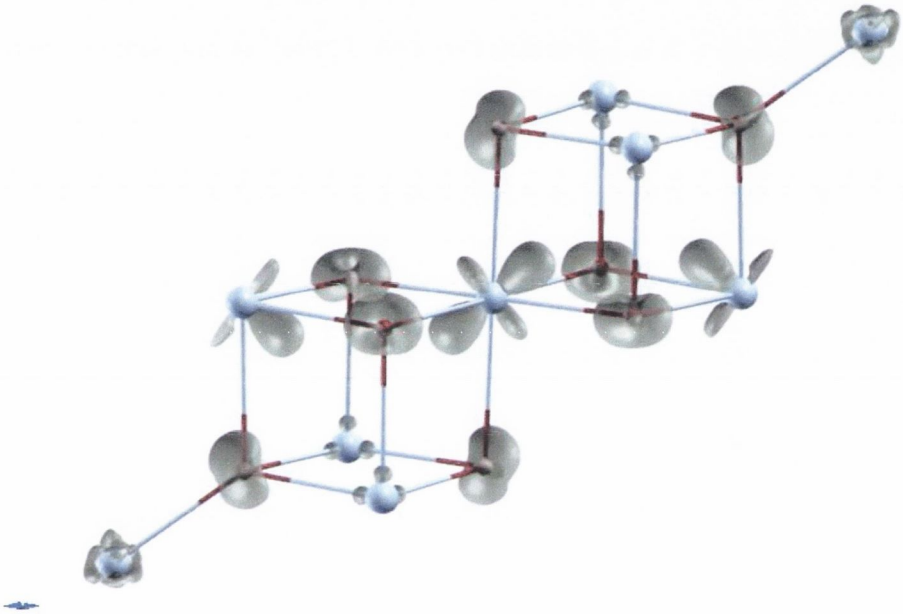

Figure 3.20: $Fd\bar{3}m$ cell orbital order at 30% exchange.

3.6.2 20%

We now consider the half-metallic cubic cell, obtained by reducing HF exchange to 20%. Traditionally this has been considered the ground state of metallic Fe_3O_4, though there is some dispute about this, as outlined in our experimental overview. Figs. 3.21 and 3.22 show the electronic band structure for majority and minority band structures. The band dispersion is much the same as the 30% case, though there is a rigid shift of bands which closes the minority gap. This gap closing can be seen clearly in the total density of states plot in Fig. 3.23. In fact, we are right on the cusp of the metal-insulator transition.

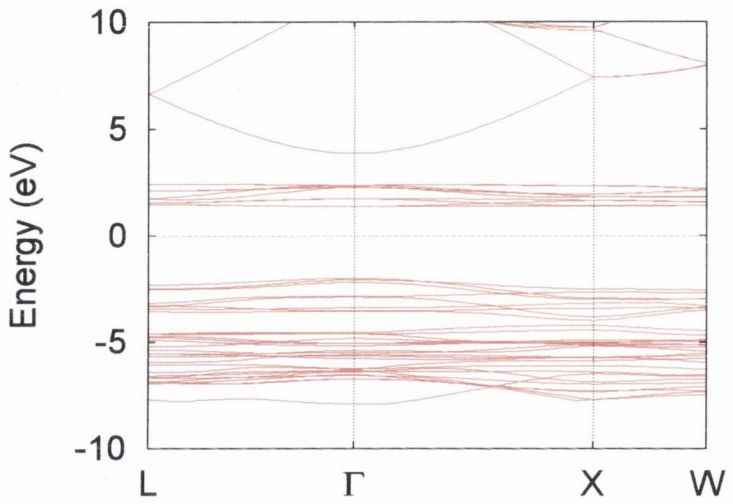

Figure 3.21: $Fd\bar{3}m$ cell majority spin band structure at 20% exchange.

Charge and spin populations are shown in Tables 3.12 and 3.13. Two of our three 20% solutions do not show charge order. In our 30% case, CO occurred only when a charge neutral $Fe^{+2.5}$ initial configuration was used in the calculation. Now, this initial configuration leads to a non-CO state. We obtain a charge-ordered state, with $\sim 0.25e$ disproportionation, from a

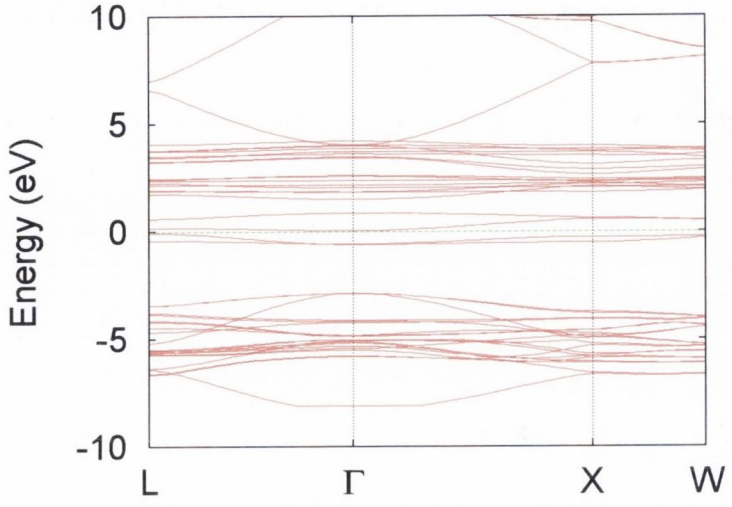

Figure 3.22: $Fd\bar{3}m$ cell minority spin band structure at 20% exchange.

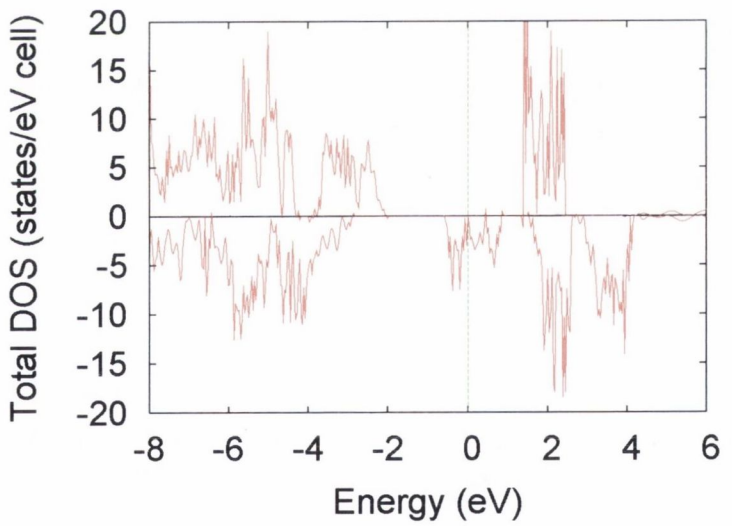

Figure 3.23: $Fd\bar{3}m$ cell total density of states at 20% exchange.

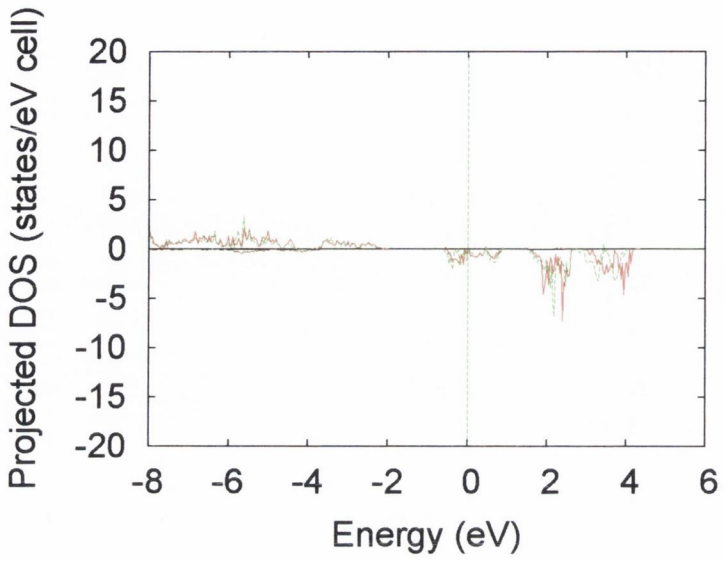

Figure 3.24: $Fd\bar{3}m$ cell B_b-B_d projected density of states at 20% exchange.

Initial	A	B_a	B_b	B_c	B_d
B_aB_d	5.89	6.02	5.99	5.99	6.02
B_bB_c	5.90	6.14	5.88	5.88	6.13
$B\_B\_$	5.89	6.01	6.01	6.01	6.01

Table 3.12: 3d-shell charge populations for Fd$\bar{3}$m cell at 20% exchange.

Initial	A	B_a	B_b	B_c	B_d
B_aB_d	-4.16	3.99	4.04	4.04	3.99
B_bB_c	-4.15	3.79	4.19	4.19	3.80
$B\_B\_$	-4.16	4.01	4.01	4.01	4.01

Table 3.13: 3d-shell spin populations for $Fd\bar{3}m$ cell at 20% exchange.

B_bB_c Fe^{2+} starting point. The corresponding projected density of states for this situation is shown in Fig. 3.24. The CO solution is almost identical in energy to our non-CO $B\_B\_$ solution, the latter of which is lower by just 10 meV/fu. Thus, at the cusp of the metal-insulator transition there is considerable competition between charge ordered and non-CO ground states, with the non-CO state apparently winning and closing the band gap. Also, the charge population tends to increase on all ions as the percentage of exchange is decreased from 30 to 20%, in line with our earlier findings for the $P2/c$ cell.

3.6.3 30% Structure Optimisation

We have performed a number of structure optimisations on the $Fd\bar{3}m$ cubic cell, starting from our previously converged ground state solutions in the cubic geometry (Table 3.10). For those solutions, we recall that the single charge ordered solution $B\_B\_$ was energetically favoured over the almost degenerate non-CO cases. Remarkably, we find that the structure optimisation stabilises a generic charge ordered state with $0.41e$ charge disproportionation, regardless of which initial solution we input into our structure calculation. This is reflected in Tables 3.16 and 3.17 for the charge and spin populations. It is interesting to note that the ordering takes place on different pairs of Fe_B ions in each case, depending on which ground state solution is used for the optimisation. These different configurations are nearly degenerate. In addition, these populations are in close agreement with those obtained from our low-temperature $P2/c$ optimised structure (Table 3.3) at 30% exchange. We see that the Fe_A population is, once again, entirely unaffected by the presence of a structural distortion. Thus we have found that CO can exist even without breaking the cubic symmetry of the high-temperature cell - an important distinction from LDA+U studies which obtained CO (Table 3.9) but only considered the low-temperature $P2/c$ cell

[76],[77],[75]. Conversely, however, we have also shown that a symmetry-lowering distortion[4] on a *non-CO* cubic cell solution can itself generate a CO configuration, once electronic correlation is sufficient to open a band gap in the cubic cell. This essentially demonstrates the cooperative nature of both strong electron-electron correlation and electron-lattice interaction in the Verwey transition.

It could be expected, given our results for the $P2/c$ cell optimisation, that distortion of Fe-O octahedra will occur around the high-charge Fe_B ions. Since the Fe^{2+}-like state can in fact occur on any two of the four Fe_B ions in the doubled unit cell, we would expect that an electron hopping between B-sites to be dressed by a dynamic lattice distortion, suggestive of polaronic behaviour.

Bond	Distances (Å)
A-O (× 4)	1.889
B-O (× 6)	2.058

Table 3.14: Experimental $Fd\bar{3}m$ bond lengths [11].

Experimental Fe-O bond lengths are shown for reference in Table 3.14. Our results for the lowest energy ($B\_B\_$) optimisation are shown in Table 3.15. Using the Isotropy code [79], we find that this new structure corresponds to the low symmetry $P1$ space group, with 14 unique atoms in the unit cell, and unit cell vectors $a = (0, 0, 1)$, $b = (0, 1, 0)$ and $c = (-1, 0, 0)$ relative to the parent $Fd\bar{3}m$ cubic space group. Oxygen octahedra are expanded around the high-charge Fe_B sites and contracted around the low-charge sites, as was seen for the $P2/c$ cell optimisation. Though Mulliken populations are similar for both this $P1$ cell and our previous optimised $P2/c$ cell at 30%, a comparison of bond lengths (recall Table 3.5) shows that the

[4]resulting from our structure optimisation which breaks cubic symmetry.

Table 3.15: Fe-O bond lengths for the optimised $P1$ structure at 30% exchange, using our $B(-)B(-)$ solution (Table 3.16).

Bond	$B(-)B(-)$ case (Å)
A(1)-O(1)	1.911
A(1)-O(2)	1.911
A(1)-O(3)	1.873
A(1)-O(4)	1.870
A(2)-O(5)	1.911
A(2)-O(6)	1.911
A(2)-O(7)	1.870
A(2)-O(8)	1.873
B(1)-O(3)	2.080
B(1)-O(8)	2.080
B(1)-O(4)	2.088
B(1)-O(7)	2.088
B(1)-O(2)	2.123
B(1)-O(6)	2.123
B(2)-O(7)	2.083
B(2)-O(4)	2.083
B(2)-O(8)	2.086
B(2)-O(3)	2.086
B(2)-O(1)	2.123
B(2)-O(6)	2.123
B(3)-O(4)	1.996
B(3)-O(7)	1.996
B(3)-O(2)	2.033
B(3)-O(6)	2.033
B(3)-O(1)	2.033
B(3)-O(5)	2.033
B(4)-O(8)	1.997
B(4)-O(3)	1.997
B(4)-O(1)	2.032
B(4)-O(5)	2.032
B(4)-O(2)	2.032
B(4)-O(6)	2.032

overall magnitude of octahedral expansion and contraction is greater for the low-temperature optimised cell. The Fe_A-O lengths are similar for both structures. Ordering of $d_{xz} + d_{yz}$ t_{2g} orbitals continues to occur with very similar occupation numbers to the $Fd\bar{3}m$ cell. We note that our optimised $B_bB_c^{SO}$ structure also has $P1$ symmetry.

As in the case of the $P2/c$ cell optimisation, the band gap is substantially widened by the structural distortion from 0.3 eV to 2.1 eV, as shown in Fig. 3.25). There is a also a pronounced narrowing of the minority band just below E_F, showing further localisation of the 'extra' $Fe_{B\downarrow}$ charge on Fe^{2+}-like sites accompanying the lattice distortion. In fact, the $P1$ cell DOS is strikingly similar to our optimised $P2/c$ cell, which had a 2.2 eV gap at 30% (Fig. 3.16).

Table 3.16: 3d-shell charge populations for structure-optimised cell at 30% exchange.

Initial	A	B_a	B_b	B_c	B_d
$B_aB_d^{SO}$	5.83	5.77	6.18	5.77	6.18
$B_bB_c^{SO}$	5.83	6.18	6.18	5.77	5.77
$B_bB_d^{SO}$	5.83	5.77	5.77	6.18	6.18
$B\_B_-^{SO}$	5.83	6.18	6.18	5.77	5.77

3.6.4 20% Structure Optimisation

We have also performed structure optimisations on the half-metallic cubic cell at 20% exchange. Our two lowest energy solutions in this case are the charge ordered solution with high-charge states occurring on Fe B_a and B_d, obtained from a B_bB_c charge ordered initial configuration, and the non-charge ordered solution obtained from a neutral $Fe_B^{+2.5}$ initial configuration. We label these solutions $B_bB_c^{SO}$ and $B\_B_-^{SO}$ for consistency with our earlier

Table 3.17: $3d$-shell charge populations for structure-optimised cell at 30% exchange.

Initial	A	B_a	B_b	B_c	B_d
$B_a B_d^{SO}$	-4.25	4.34	3.76	4.35	3.76
$B_b B_c^{SO}$	-4.26	3.76	3.76	4.35	4.35
$B_b B_d^{SO}$	-4.25	4.34	4.35	3.76	3.76
$B\_B_{-}^{SO}$	-4.25	3.76	3.76	4.35	4.35

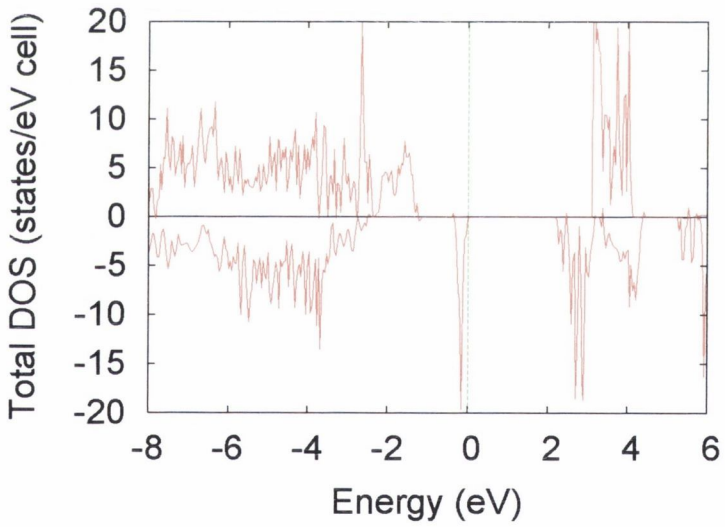

Figure 3.25: Optimised cell total density of states at 30% exchange.

Mulliken population results in Table 3.12. The obtained $B\_B_{-}^{SO}$ structure was unstable and divergent in energy. The $B_bB_c^{SO}$ and $B_aB_d^{SO}$ optimisations both yielded cells with $P1$ space group. These structures were equal in energy.

Fe-O bond lengths for the $B_bB_c^{SO}$ solution are shown in Table 3.18. There is an expansion of bond lengths in the Fe-O octahedra around $B1$ and $B2$ ions, with a corresponding contraction around $B3$ and $B4$ in the $P1$ cell, corresponding to the charge ordering in this system. Charge and spin populations are given in Tables 3.19 and 3.20, and it is seen that the lattice optimisation once again stabilises a charge-ordered state. There is also an associated orbital ordering. We note that distortion of A-site oxygen tetrahedra and B-site oxygen octahedra becomes less pronounced as we move to 20% exchange.

One might expect from previous experience that the optimisation introduces a significant band gap. This would be of particular significance in this case as we would be moving from a cubic half-metallic cell to a charge-ordered insulating cell with triclinic $P1$ distortion. This case thus provides an effective simulation of the Verwey transition. Figure 3.26 shows the total Density of States for the optimised $P1$ cell. The system is now insulating charge-orbital ordered, with a $\sim$ 0.76 eV band gap created purely by electron coupling to the lattice. This demonstrates the critical role of the electron-phonon interaction in the Verwey transition.

Symmetry Analysis

Consider a crystalline solid containing N atoms. Let $\vec{r}_i$ be the position of the i^{th} atom. Let the space-group symmetry of the crystal be G. A $3N$-dimensional vector ϕ can describe displacements of atoms. The $3N$ coordinates of the vector are given by $\phi_{i\alpha}$, where $\alpha = 1, 2, 3$ refers to the coordinates of the i^{th} atom. This displacement vector lies in some $3N$-

Table 3.18: Fe-O bond lengths for optimised $P1$ structure at 20% exchange.

Bond	B_bB_c case (Å)
A(1)-O(1)	1.908
A(1)-O(2)	1.906
A(1)-O(3)	1.865
A(1)-O(4)	1.885
A(2)-O(5)	1.907
A(2)-O(6)	1.906
A(2)-O(7)	1.884
A(2)-O(8)	1.866
B(1)-O(4)	2.060
B(1)-O(7)	2.061
B(1)-O(8)	2.092
B(1)-O(3)	2.093
B(1)-O(2)	2.116
B(1)-O(6)	2.116
B(2)-O(4)	2.073
B(2)-O(7)	2.073
B(2)-O(8)	2.083
B(2)-O(3)	2.084
B(2)-O(5)	2.113
B(2)-O(1)	2.114
B(3)-O(4)	2.011
B(3)-O(7)	2.012
B(3)-O(5)	2.032
B(3)-O(1)	2.033
B(3)-O(6)	2.036
B(3)-O(2)	2.037
B(4)-O(3)	2.005
B(4)-O(8)	2.005
B(4)-O(1)	2.036
B(4)-O(5)	2.037
B(4)-O(2)	2.041
B(4)-O(6)	2.041

Table 3.19: $3d$-shell charge populations for structure-optimised cell at 20% exchange.

Initial	A	B_a	B_b	B_c	B_d
$B_aB_d^{SO}$	5.91	5.84	5.85	6.18	6.18
$B_bB_c^{SO}$	5.91	6.18	6.19	5.84	5.86

Table 3.20: $3d$-shell spin populations for structure-optimised cell at 20% exchange.

Initial	A	B_a	B_b	B_c	B_d
$B_aB_d^{SO}$	4.15	-4.25	-4.24	-3.72	-3.73
$B_bB_c^{SO}$	4.14	-3.72	-3.72	-4.25	-4.22

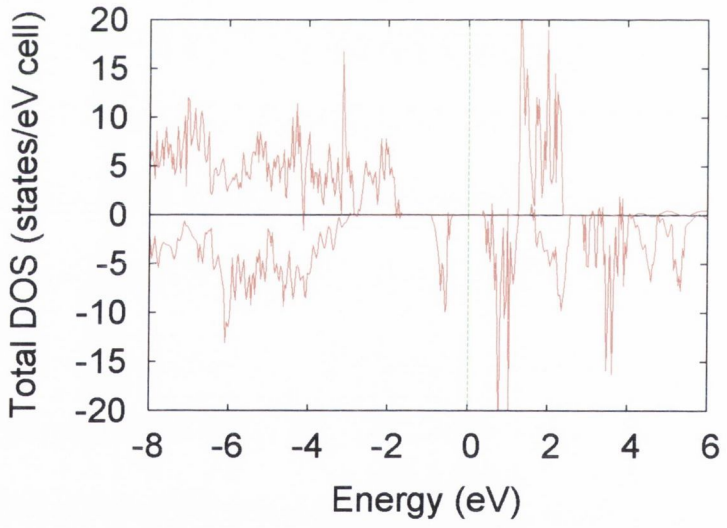

Figure 3.26: Total Density of States for optimised structure at 20% exchange.

dimensional vector space S. All vectors spanning this space can describe atomic displacements. The displacement vector is zero in the high-symmetry with space group G. In general, a displacive phase transition will lower the symmetry to a group H. This new space-group symmetry H is a subgroup of G and consists of all g in G which leave the displacement vector ϕ invariant, i.e. $g\phi = \phi$.

We wish to characterise the displacement from magnetite's cubic cell with $Fd\bar{3}m$ symmetry to the $P1$ symmetry present in our structure optimised cell. The Landau theory of phase transitions involves using an *order parameter* (OP), representing the atomic displacement, which is zero in the high-temperature phase and non-zero in the low-temperature phase [80]. We can try to classify the symmetry of this phase transition in terms of *irreducible representations* (IR) of the high-symmetry group G. Each n-dimensional IR has an associated n-dimensional vector space spanned by n-dimensional vectors which are order parameters of displacements consistent with the irrep symmetry. The total $3N$-dimensional vector space containing displacement vectors ϕ can be completely decomposed into these IR subspaces S'.

The IR maps symmetry operators g in G onto an $n \times n$ matrix $D(g)$. For a given OP $\mathbf{v}$ of the transition, the operators g in G which satisfy $D(g)\mathbf{v} = \mathbf{v}$ form a group H' such that its symmetry is greater than or equal to that of H. All group H' and H are called *isotropy subgroups*. The OPs for which $H' = H$ are primary OPs. They determine the symmetry of the low-symmetry phase. The other OPs in the set are secondary OPs. In general, a full description of the symmetry-lowering transition from G to H will not be directly given in terms of a single OP associated to an IR of G. Thus, the symmetry of H will be determined by coupled order parameters (representing atomic displacements which lower the symmetry of G) associated to IRs of G. Secondary OPs couple to primary OPs in a

specific way - at the phase transition, the primary OP becomes non-zero and the secondary OP also becomes non-zero because of this coupling to the primary OP. In some group-subgroup relations, a single primary OP is not sufficient and several coupled primary OPs induce the transition [80]. We find that this is actually the case in the $Fd\bar{3}m \rightarrow P1$ transition which occurs following our optimisation of the high-temperature cubic cell.

The aim of the COPL code [81] is to generate a complete set of OPs, both primary and secondary, associated with a given group-subgroup pair of space groups, G and H. This is done via a solution of the so-called inverse Landau problem [82]: given a group G and a subgroup H, we wish to find the irreducible representation of G determined by this transition. Details of the algorithm may be found in [83]. We have used this code to analyse the $Fd\bar{3}m$ to $P1$ structural phase transition which occurs in our structure optimisation of the cubic cell. The results are shown in Table 3.21.

We have obtained a list of IRs and the corresponding directions of order parameters in the IR space. The notation for IRs corresponds to the convention of Miller and Love [84], and the specific form of the OP depends on the choice of matrices for the IR. Γ point displacements are labelled by Γ - these are the displacements which are visible by infrared and Raman spectroscopy. X point displacements are labelled accordingly, where X is at $(1, 0, 0)$ in the Brillouin zone.

It can be seen from Table 3.21 that there are 6 primary order parameters which take take the $Fd\bar{3}m$ space group to $P1$. The first two are associated to 3-dimensional irreps Γ_4^- and Γ_5^-. The remaining four IRs occur at the X point and have 6-dimensional order parameters (a, b, c, d, e, f). Interestingly, these order parameters yield atomic displacements which cause a cell quadrupling. In other words, they permit the transition from a 14 atom cubic cell to a 56 atom cell with $P1$ symmetry. This $P1$ cell has basis vectors (0,1,0), (0,0,1) and (1,0,0) and the same origin relative to the parent

Table 3.21: Irreducible representations, corresponding primary and secondary order parameters and isotropy subgroups of the Fe_3O_4 $Fd\bar{3}m$ to $P1$ space group displacive phase transition.

IR	OP Direction	Size	Subgroup	No
Γ_1^+	(a)	1	$Fd\bar{3}m$	227
Γ_2^+	(a)	1	$Fd\bar{3}$	203
Γ_3^+	(a,b)	1	$Fddd$	70
Γ_4^+	(a,b,c)	1	$P\bar{1}$	2
Γ_5^+	(a,b,c)	1	$P\bar{1}$	2
Γ_1^-	(a)	1	$F4_132$	210
Γ_2^-	(a)	1	$F\bar{4}3m$	216
Γ_3^-	(a,b)	1	$F222$	22
Γ_4^-	(a,b,c)	1	$P1$	1
Γ_5^-	(a,b,c)	1	$P1$	1
$X1$	(a,b,c,d,e,f)	4	$P1$	1
$X2$	(a,b,c,d,e,f)	4	$P1$	1
$X3$	(a,b,c,d,e,f)	4	$P1$	1
$X4$	(a,b,c,d,e,f)	4	$P1$	1

$Fd\bar{3}m$ cell. We recall that the monoclinic $P2/c$ cell determined experimentally by Wright, within orthorhombic $Pmca$ symmetry constraints, had 56 atoms. The 56-atom triclinic $P1$ cell we obtain here has lower symmetry than $P2/c$. We mention, however, that $P1$ symmetry has been advanced as the space group of the low-temperature phase of Fe_3O_4, based on the observation of a magnetoelectric effect [85], while an x-ray topography study showed twins which were consistent with triclinic symmetry [86]. However, the Raman study of Gasparov et al [69], which we discussed in Section 3.4, failed to find the modes that should be active in a cell like $P1$ which lacks inversion symmetry.

Thus, a single primary order parameter is not sufficient to define this group-subgroup relationship , and we find that multiple primary OP's induce the transition. This process does not lead to new distortion modes, but rather combines existing distortion modes from different irreps to achieve more complex distortions. Primary order parameters energetically drive the phase transition. Table 3.21 shows that there are secondary OP's - while not sufficient to lower the symmetry themselves, they couple to primary OP's in order to achieve a fully arbitrary distortion which utilizes all the degrees of freedom available to the superstructure.

We have investigated how these OP's affect the $Fd\bar{3}m$ structure using the ISODISPLACE visualisation tool [87]. Figure shows the 14-atom cubic $Fd\bar{3}m$ cell with axes indicated for both this cell and the corresponding 14-atom $P1$ cell. ISODISPLACE can consider the action of order parameters on a given unique atomic site. Thus the modes at a given atomic site can be classified according the the Wykoff site point-group irreps that induce its local distortion.

The Γ-point primary order parameter associated to the Γ_4^- irrep of $Fd\bar{3}m$ induces uniform shifts of all three types of atom - Fe_A, Fe_B and O - along the $< 111 >$ direction. This distortion corresponds to an Fe_A T_2, Fe_B A_{2u}

and E_u and oxygen A_1 and E distortion modes. Raman spectroscopy [69] showed a strong peak at 670 cm^{-1} which was attributed to an oxygen A_{1g} mode like the above, representing stretching vibrations of the oxygen atoms along the Fe_A-O bonds in a $< 111 >$ direction relative to the cubic axes.

The order parameter associated to the three-dimensional Γ_5^- irrep induces displacements of all atoms, except the central Fe_B atom with orbital order, and the oxygen atoms pointed to by the lobes of the orbital seen in our charge density difference plot in Figure 3.20. The other four primary order parameters lie in the carrier space of six-dimensional X-point irreps of $Fd\bar{3}m$, and induce atomic displacements in the quadrupled 56-atom cell. Strain modes are always associated with Γ-point irreps and usually appear as secondary order parameters in displacive phase transitions, though they must be primary in proper ferroelastic transitions [79]. In our case, the (a)-directed OP for Γ_1^+ is an overall cell volume change, while Γ_3^+ and Γ_5^+ are modes associated to expansion and contraction of individual cell axes.

The above analysis is based purely on group theoretic symmetry considerations for *any* $Fd\bar{3}m$ to $P1$ displacive transition with our lattice parameters and atomic coordinates. The actual relative amplitudes of the distortion modes obtained above will depend on physical parameters such as atomic masses, interatomic forces and thermodynamic state variables, requiring experimental (e.g. diffraction) or further ab-initio calculations.

3.7 Conclusion

At this point we pause to consider our results, and see that a plausible mechanism for the Verwey transition is beginning to emerge. We begin with our $Fd\bar{3}m$ cubic cell results at 30% HF exchange in Section 3.6.1. Of our four solutions in Table 3.10, we found that the charge ordered one was clearly energetically favourable over the three degenerate non-CO solutions, being 256 meV/formula unit lower in energy. This shows that the 'extra' Fe B-site

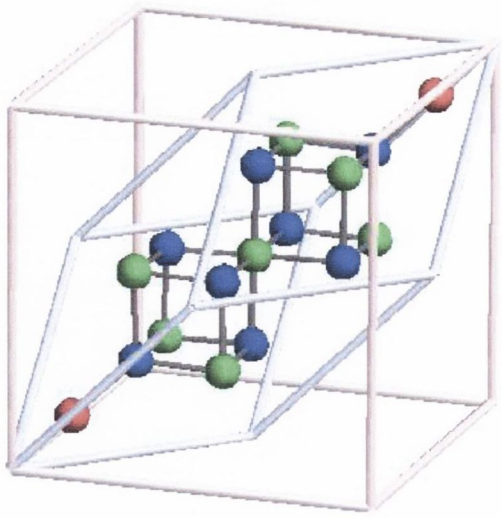

Figure 3.27: $Fd\bar{3}m$ cell with corresponding $P1$ axes shown. Fe_A sites are in red, Fe_B in green and oxygen in blue.

electron[5] prefers to localise on one of the two Fe_B ions in the formula unit rather than spreading evenly in a non-CO $Fe^{+2.5}$-like configuration, even *without* the presence of a monoclinic distortion. The LSDA+U results of Leonov [77] and Jeng [76] are carried out in the $P2/c$ cell only, making it unclear whether CO/OO can exist without the monoclinic distortion which occurs below T_V. We show that CO can indeed occur in the cubic cell and is not merely an artifact of the experimental $P2/c$ cell [11] used in our calculations. We ascribe the cause of this charge ordering preference to the electrostatic repulsion, resulting from mixing 30% HF exchange in the density functional. This assertion is confirmed by our 20% cubic solutions (Table 3.12). Reducing the HF exchange to 20% results in the the CO and non-CO solutions (Table 3.12) becoming almost degenerate in energy,

[5]For illustrative purposes and to avoid excessive pedantry in the ensuing discussion, we will speak of the 'extra' Fe_B electron , even though our results clearly show that the B-site charge disproportionation is only a fraction of e.

with non-CO winning out by only 10 meV/fu as the system turns metallic - the lower amount of electrostatic repulsion in this case means that electron localisation on a particular Fe_B site is not so markedly favourable. We further believe that it is *d-d* repulsion in particular that is mainly responsible for electron localisation on a particular *B*-site, since our band structure and DOS calculations for the cubic insulating cell (Figures 3.17, 3.18 and 3.19) and the experimental low-temperature cell (Figures 3.6, 3.7 and 3.19) show that the minority gap resulting from the electron localisation is of predominantly *d-d* character[6]. The aforementioned DOS calculations show that the 'extra' electron occupies a narrow spin-down band just below the Fermi energy.

This is not all; the 'extra' spin-down electron occupies a specific *d*-orbital on the Fe_B site, leading to orbital order (Figure 3.20). This order results from the localised $t_{2g}^4 e_g^2$ configuration of Fe^{2+}, which is triply degenerate and thus is a Jahn-Teller active distortion mode [11]. We then allowed the cell to relax in order see the effect of this electron localisation on the surrounding Fe-O octahedron. The cubic symmetry of the high temperature cell is broken by the orbital ordering. The lattice distortion occurs on the *B*-site sublattice and is largest in the oxygen octahedra surrounding the JT-active orbital ordered sites (Tables 3.15 and 3.18). This distortion lowers the energy by a further 440 meV/fu (100 meV/fu in the 20% solution). Our new structure is a 14 atom cell with $P1$ space group. We have further determined the irreducible representations and corresponding cell distortion modes which energetically drive the symmetry lowering from $Fd\bar{3}m$ to $P1$ symmetry (Table 3.21).

The JT distortion is strongly coupled to the localised Fe_B electron just

[6]After our calculations were completed, a recent GGA+U study by Pinto and Elliot [88] was brought to our attention which also found that a CO insulating state is favoured in the cubic geometry for sufficiently high values of U, in agreement with the present work using hybrid HF/DFT.

below the Fermi energy. This Fe-O octahedral distortion results in a widening of the band gap and a narrowing of the spin-down band just below E_F, as shown in the DOS of the $P1$ structure (Figures 3.25 and 3.26). The action of the localised electron's coupling to the surrounding O octahedra can be seen in the DOS of our 30% and 50% structure optimisations of the experimental $P2/c$ low-temperature cell (Figure 3.16). The extra distortion induced by the optimisation further pins the 'extra' electron and significantly widens the band gap. Thus, once orbital ordering has occurred and the cubic structure has been distorted to a lower symmetry cell, then further structural optimisation of the monoclinic $P2/c$ cell causes further Fe-O octahedral distortion around OO sites but has little effect on charge and spin populations (Tables 3.4 and 3.3).

We find that tetrahedral Fe_A charge populations are actually closer to 2+, as opposed to the 3+ expected in a simple ionic picture. There is experimental evidence for an Fe_A^{2+}-like state below T_V from Mössbauer [59] and NMR [58] spectroscopy. However, orbital order does not occur on tetrahedral Fe_A ions. We find that lattice distortion when the cubic cell symmetry is broken is not significant around Fe_A sites compared to B-sites (Tables 3.15 and 3.18).

The localising influence of strong electron correlation therefore cooperates with the strong electron-lattice interaction by facilitating strong JT coupling around OO sites. Our results do not support contention of Garcia et al [56], [7] and Subias et al [57], based on their x-ray diffraction experiments, that charge ordering does not occur in magnetite. Our results are, however, fully consistent with these authors' view of the key role played by the strong electron-phonon coupling in the conduction mechanism - this is visible in the large band gap opening we see occurring with in our $Fd\bar{3}m$ to $P1$ structure optimisation, due to distortion mainly around JT-active orbitally ordered Fe_B sites. The key role of electron-phonon coupling also is

strongly supported in many other studies: X-ray [89], Raman [90] and heat capacity [91] experiments show the large influence of doping on the Verwey transition temperature, while optical conductivity [67], photoemission [60] and Raman spectra [69] show clear evidence for polaronic behaviour in temperature ranges around T_V [13]. Thus, the above ab-initio study shows the critical cooperative role that charge/orbital order and strong electron-phonon coupling play in the Verwey transition in magnetite.

Chapter 4

Manganites

4.1 Introduction

4.1.1 Background

The study of strongly correlated electron systems in low-dimensions has been in many respects the most challenging and fascinating field of condensed matter physics. Many of the most startling examples of emergent order [15] and collective behaviour from the last 30 years have originated from this class of many-body system. Some behaviour has even challenged the conventional many-body physics paradigm, due to Landau, and forced theorists to re-evaluate the twin cornerstones of traditional condensed matter theory: the Fermi liquid theory and the Landau theory of classical phase transitions. The first of these, the Fermi liquid theory, is based on the notion of the weakly interacting, spin-1/2, charge 1 electron quasiparticle with finite lifetime as the fundamental entity of a many-electron system. The second, the Landau theory of phase transitions[1] rests on the idea that changes of phase can be described by thermally-induced fluctuations of a *local* (i.e. spatially dependent) order parameter, e.g. the magnetisation in a

[1] or its slightly more sophisticated formulation in terms of the Renormalisation Group [92].

second-order paramagnetic to ferromagnetic phase transition, or more generally between some symmetric and symmetry-broken phase. This is the notion of spontaneously broken symmetry - in fact, the Landau order parameter quantifies the amount of symmetry breaking in any ordered phase. In our example, the paramagnet is symmetric with respect to spin orientation, while in the ferromagnet, this symmetry is "broken" - there is now a preferred spin alignment.

Both conditions are spectacularly violated in the two-dimensional gas in a high magnetic field. This is the famous quantum Hall effect, where transitions can occur between degenerate ground states which cannot be classified by any local order parameter. The Fractional Quantum Hall Effect in particular permits quasiparticle statistics which are neither Fermi-Dirac (spin-1/2) or Bose-Einstein (spin-1), but can have quantum numbers which are "fractionalised" and lie between Fermi and Bose statistics. Such quasiparticles are said to have anyonic statistics and were dubbed anyons by Franz Wilczek, who, along with Zee, first postulated the existence of fractional statistics in 2 dimensions [93] in 1982. These quasiparticles could also carry fractionalised units of charge. This seemingly bizarre situation has its origin in the particular topology of 2-dimensional space and the Berry phase that is acquired when two electrons are interchanged in two spatial dimensions. The existence of anyonic statistics has been unambiguously confirmed in interferometry experiments of quantum Hall systems [94].

The celebrated Landau theory of phase transitions also fails for FQHE systems. It was discovered that no *local* (i.e. spatially dependent) order parameter could distinguish phase transitions between degenerate ground states of the system. Only the *global* properties of the ground state wavefunction determined the degeneracy and transitions between ground states. This implies that the topology of the system has an influence on the ground states - in simple terms, the ground state depends on the topology of the

manifold where the electrons live. It can be shown that on a surface of genus g (i.e. with g holes), the ground state degeneracy is equal to k^g for the quasiparticle with fractional charge p/k [95].

The behaviour of such systems with ground state degeneracies, exitations having fractional quantum numbers, and dependence on the manifold in which the electrons live can be abstracted beyond the FQHE, and has been dubbed *topological order* by Wen. The long distance physics of these topologically ordered systems and their low-lying quasiparticle excitations are described by a new class of field theories known as topological quantum field theories (TQFTs). Mathematical work on TQFTs commenced in the late 80's with the Fields medal-winning work of Witten [96], and subsequent axiomatization by Atiyah [97]. This work fortuitously permitted the subsequent classification of topologically ordered condensed matter systems [95] - one such TQFT, the Chern-Simons theory [98], is in fact the low-energy effective theory for fractional quantum Hall systems[2].

A further surprise for theorists was that fractionalized quasiparticles can be realised relatively easily, at least theoretically, in simple Hamiltonians, without the presence of a magnetic field [101]. The main impetus for theoretical work on such fractionalised quasiparticle phases (called "topological phases") of 2d Hamiltonians was the suggestion by Anderson in 1987 that such physics, dubbed "spin-charge separation", may be responsible for the anomalous behaviour of the so-called pseudogap phase in 2d high-temperature superconducting cuprates [14]. This has led to a plethora of theoretical realisations of 2d systems with exotic fractionalised excitations, such as spin liquids [102], Z_2 gauge theories [103], deconfined quantum critical points [102] etc. Laughlin and Pines' notion of a "quantum protectorate" [15] has been evoked by Anderson to argue that such phases may be per-

[2]The seemingly miraculous links between 2d electrons in a magnetic field and modern mathematics continue to abound, with the recent assertion that the dynamics of the fractional quantum Hall fluid may be described by a non-commutative field theory [99],[100].

mitted in cuprates at finite temperature [17]. To date however, no definitive experimental evidence exists that such phases are actually realised in the pseudogap phase of cuprates. Very recently, topological phases of interacting electrons have been subject to a renewed surge of interest [104],[105] with the revelation that they may permit naturally fault-tolerant quantum computation [106],[107].

We mention that the Luttinger liquid in one-dimensional spin chains also exhibits a form of fractionalisation in the form of so-called spin-charge separation. This has long been known and is thought to originate from simple one-dimensionality, and not the same topological order mechanism as described above. Very recently, Oshikawa and Senthil have argued, based on general principles, that topological order is essential to realise fractionalisation in insulating phases in dimensions $d \geq 2$ [108].

In the preceding discussion, we hope to have given the briefest of hints of the kind of remarkable and counterintuitive physics that can arise when strong electronic correlation and low dimensionality are combined. This work will focus on a doped Mott insulator with effective 2-dimensional character: the half-doped bilayer manganite $LaSr_2Mn_2O_7$. The doped bilayer manganites with the general formula $La_{2-x}Sr_{1+2x}Mn_2O_7$, where x is the fraction of hole doping, have attracted much recent interest [109]. They possess a rich phase diagram due to a complex interplay of charge, spin and orbital degrees of freedom, and can exhibit the phenomenon of colossal magnetoresistance for certain doping ranges. Bilayer manganites are also interesting in that they share the essential structural features of the high-temperature superconducting cuprates, with pseudogap behaviour [110] and apparent nodal features Fermi surface features being recently seen in ARPES experiments [111][112],[113],[114], in common with the cuprates [115],[116][19]. It is to this latter class of system that we now turn our attention.

4.1.2 High-Temperature Superconducting Cuprates

In 1986, superconductivity was discovered up to 30K in a class of LaBaCuO ceramics by Bednorz and Müller [117]. This was the highest known superconducting temperature, and at the time it was completely unexpected that such behaviour would arise in this transition metal oxide. By 1987, a T_c of approximately 90K had been observed in $YBa_2Cu_3O_{7-\delta}$. The record T_c of 133.5K at atmospheric pressure was later obtained in the trilayer system $HgBa_2Ca_2Cu_3O_{8+x}$ [118]. It was soon realised that this new class of high-T_c superconductors had a number of key common features that must be responsible for the anomalous superconductivity mechanism [119].

Firstly, the materials are quasi-2-dimensional; the key structural unit is the CuO_2 plane, consisting of a square lattice of Cu ions surrounded by four oxygens. Secondly, high-temperature superconductivity was obtained by doping a parent Mott insulator. In the parent compound, the formal valence of Cu is 2+, which means that its electronic structure is in the d^9 configuration. The copper is surrounded by six oxygens in an octahedral environment. The distortion from a perfect octahedron splits the e_g orbitals so that the highest partially occupied d orbital is $x^2 - y^2$. The lobes of this orbital point directly to neighbouring oxygen p orbitals, forming a strong covalent bond with a large hopping integral t_{pd} (Figure 4.1). In the archetypal example, the parent antiferromagnetic Mott insulator La_2CuO_4 is hole-doped by substituting La ions for Sr ions, to give the series $La_{2-x}Sr_xCuO_4$, with x holes per Cu added to the CuO_2 layer. Upon doping, the antiferromagnetism is rapidly destroyed and insulators become poor metals in the normal state and high-temperature superconductors (HTSCs) upon reducing the temperatures. A phenomenological phase diagram for the electron- and hole-doped HTSCs can be seen in Figure 4.2 taken from the ARPES review of Damascelli et al [19].

Prior to this discovery, it was widely assumed that all known supercon-

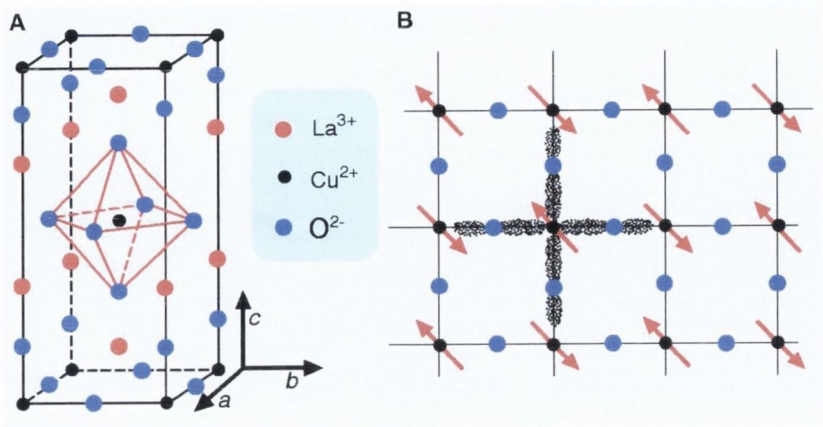

Figure 4.1: Crystal structure of La_2CuO_4, the parent antiferromagnetic Mott insulator of the $La_{2-x}Sr_xCuO_4$ family of high-temperature superconductors [120].

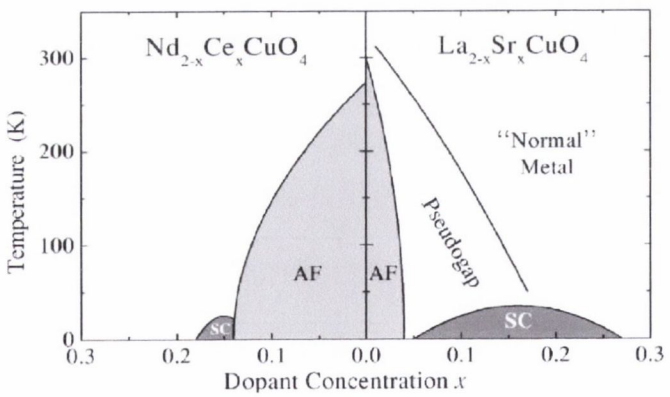

Figure 4.2: Schematic phase diagram for cuprate superconductor. The hole-doped case is on the right and the electron-doped case on the left [19].

ductors, or superfluids of neutral fermions such as ^{3}He, were described by the BCS theory. However, many of the physical properties of the new high-T_c superconducting cuprates, especially at temperatures above T_c, could not be described within the conventional BCS/Fermi Liquid theory framework. The combination of strong electron correlation, low dimensionality and proximity to a Mott insulator appeared to result in some puzzling experimental results. For example, at optimal doping for highest T_c, the isotope effect is at its minimum, a situation not expected in conventional phonon-mediated superconductivity. Even more mysterious is the behaviour above the superconducting temperature T_c at low doping. This is the so-called pseudogap phase; its features include a greatly reduced spectral weight around the Fermi energy [19], a gapped out Fermi surface with so-called 'arcs' [116], and broad spectral peaks indicating a lack of clearly defined Fermi liquid-like quasiparticles. Other distinctly non-Fermi liquid features include the linear scaling of resistivity with temperature at optimal doping, a fact incompatible with the T^2 scaling expected in a traditional Landau picture [121].

A host of theories have been evoked in an attempt to explain the anomalous superconducting and "normal" (pseudogap) states in this 2d doped Mott insulator. Resonant valence bonds [122], fractionalisation [14], dynamic inhomogeneity-induced pairing [16], superconducting stripes [5], proximity to a quantum critical point [123] and bipolaronic carrier pairing [4] are just some of the concepts which have been advanced to explain high-T_c cuprate physics.

It would be interesting to carry on this thread into an investigation of the properties of other members of the class of 2-dimensional doped Mott insulators. This reflects a developing trend of viewing such strongly correlated systems as a generic class possessing common orders and many-body behaviour [2]. In general, the problem of doped holes in an AF background is ex-

tremely complicated, involving many-particle interaction terms [124],[125]. Some theoretical research on strongly correlated electron systems has focussed on ring exchange, a generalisation of the Heisenberg pair exchange to higher order n-particle permuations [126]. Permutations of even parity (like three-particle cycles) induce ferromagnetism while odd permutations (pair and four-particle exchanges) favour antiferromagnetism. During the past 10 years, many experimental results have revealed the presence of four-spin exchange interactions in the Cu-O plaquettes of cuprates [127].

Recent experiments have pointed to a pseudogap picture in another class of 2d doped Mott insulators: the colossal magnetoresistive bilayered manganites, whose 2d electron confinement and pseudogap properties are even more extreme than that of the high Tc cuprates [128]. This class of layered transition metal oxide is relatively newly synthesized and has not received as much attention as the HTSCs, though research on bilayer manganites has become very active recently, yielding some remarkable ARPES results, which we discuss in Section 4.1.3. The crystal structure bears much similarity to the well known bilayer HTSC cuprate $Bi_2Sr_2CaCu_2O_{8+\delta}$ (Bi2212). The experimental Fermi surface topology of Bi2212 shows bilayer band splitting, that is, the splitting of the CuO_2 plane-derived electronic structure into bonding and antibonding bands due to the presence of CuO_2 bilayer blocks in the unit cell of Bi2212 [19].

4.1.3 Colossal Magnetoresistive Manganites

The manganites are a class of transitional metal oxides with general formula unit given by the Ruddelson-Popper series $(A,B)_{n+1}Mn_nO_{3n+1}$. They share a common structural feature of 2-dimensional MnO_2 planes (in analogy with the CuO_2 planes of high-T_c cuprates) stacked along the z-axis, along with (A,B)O spacer bilayers where A is a trivalent cation such as La and B a divalent cation such as Sr, Ca or Ba. For the manganite compound considered

in this work, we will consider the commonly used cations A=La and B=Sr. The number of MnO_2 layers between each (La,Sr)O bilayer is denoted by n in the Ruddelson-Popper formula. Thus the single MnO_2 layer system will have formula $(La,Sr)_2MnO_4$, the bilayer is $(La,Sr)_3Mn_2O_7$ etc. The most heavily studied series is the $n = \infty$ perovskite manganites $(A,B)MnO_3$, consisting of continuously stacked MnO_2 planes sharing apical oxygens - in other words, a stacking of MnO_6 octahedra. This is the most 3-dimensional system, referred to as cubic manganite. The situation is illustrated in Figure 4.3, taken from Ref. [129]. The MnO_2 planes form the n-layers, which are shifted in the xy-plane as shown.

A series of compounds may be obtained for a given n by doping a parent antiferromagnetic Mott insulator. This is done by replacing 3+ La ions with 2+ Sr ions. This has the effect of doping one hole for every La^{3+} that is replaced by an Sr^{2+}. The extra hole is doped into the MnO_2 plane of the unit cell. Like the high-temperature superconducting cuprates, this hole doping of the parent Mott insulator has radical effects on the behaviour of the system. The basic physics may be explained as follows. As an example, we consider the $n = \infty$ parent AF Mott insulator, the cubic $LaMnO_3$. In a simple ionic picture, the Mn ion has a $3d^4$ configuration. As shown in Figure 4.3, this ion is in an octahedral environment and is hence subject to a cubic crystal field. The crystal field breaks the degeneracy of the d-orbitals, resulting in a splitting into three-fold degenerate t_{2g} levels (d_{xy}, d_{xz}, d_{yz}) and higher energy two-fold degenerate e_g levels $(d_{x^2-y^2}, d_{3z^2-r^2})$. These e_g orbitals point directly at neighbouring oxygens, and should hybridize strongly with the O $2p$ states, forming dispersive bands containing the electrons responsible for the conduction. According to Hund's rules, the first three Mn d-electrons will go into each one of the t_{2g} levels, with the final electron filling an e_g orbital. This final electron will result in a Jahn-Teller (JT) lattice distortion to break the degeneracy of the e_g level. A d^4 ion in a cubic

crystal field is strongly Jahn-Teller active and this results in a significantly distorted lattice with *Pnma* space group. The four electron spins are aligned in accordance with strong Hund's rule intra-atomic exchange J_H. We can now start to see what will happen in our simple picture when a divalent La is replaced by a trivalent Sr. This will dope a hole into the Mn e_g, leading to unoccupied e_g levels and a subsequent diminishing of JT lattice distortion, as shown schematically in Figure 4.4, panels (a) and (b). The chemical formula of the doped cubic manganite is then $La_{1-x}Sr_xMnO_3$, where x represents the fraction of holes in the Mn e_g band. Addition of a small number of holes rapidly destroys the antiferromagnetism and 'Mottness' of the parent $LaMnO_3$, leading to a ferromagnetic metallic state for cubic manganites at low-temperature. Much work has gone into elucidating the phases of doped cubic manganites. As an example, the experimental phase diagram of $La_{1-x}Ca_xMnO_3$ is shown in Figure 4.5 [130]. The strong electron correlation and electron-lattice coupling leads to complex interplay of the charge, spin and orbital degrees in this system and yields a rich variety of phases across the phase diagram. We also note that the electron/hole-doping asymmetry present in cuprates (Figure 4.2) is also seen in the manganites.

Until relatively recently, less research has been carried out into other members of the Ruddelson-Popper series. In particular, the $n = 1$ and $n = 2$ cases are of great interest due to their effective 2-dimensional character and significant structural similarity to single and bilayer HTSC cuprates. In this work, we will focus the bilayer manganite series $La_{2-2x}Sr_{1+2x}Mn_2O_7$, following remarkable recent ARPES data on the ferromagnetic metallic $x = 0.4$ compound $La_{1.2}Sr_{1.8}Mn_2O_7$ [112],[113],[114] showing an apparent pseudogap state and gapped out Fermi surface with possible nodal quasiparticles [113], previously believed to be the sole preserve of *d*-wave superconducting cuprates [19],[115]. The experimental phase diagram upon doping for this series is shown in Figure 4.6, taken from Ling et al [109]. A variety of

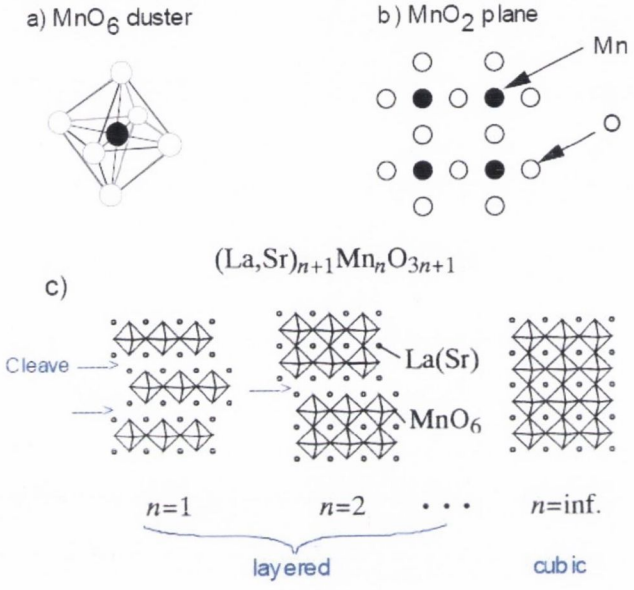

Figure 4.3: (a) An MnO_6 octahedron. (b) The MnO_2 plane, identical in structure to the CuO_2 planes of the high-temperature superconductors. (c) The crystal structure of the layered and cubic manganite. Taken from [129]

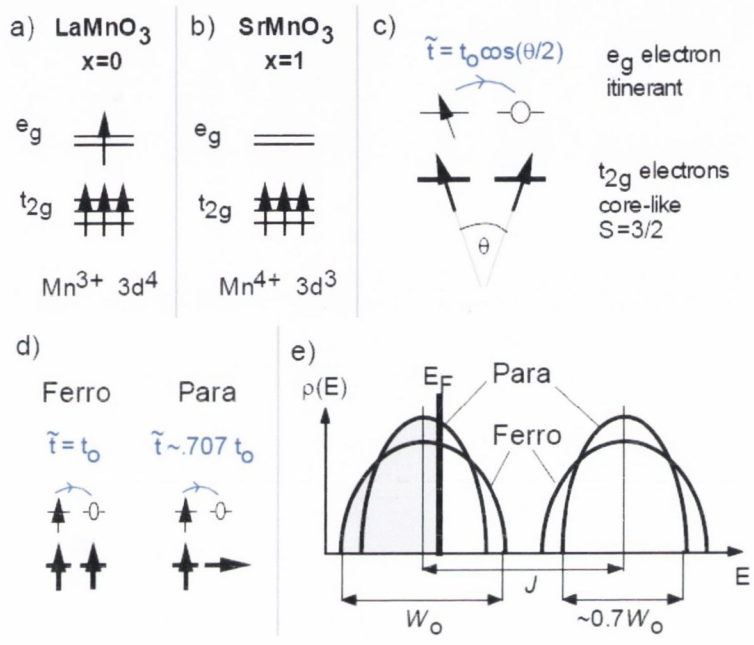

Figure 4.4: (a) The d^4 ion. (b) The d^3 ion. (c,d) An illustration of the concept of double exchange - the hopping matrix element as a function of spin alignment. (e) The double-exchange prediction of the bandwidths for the ferromagnetic and paramagnetic cases. From Ref. [129].

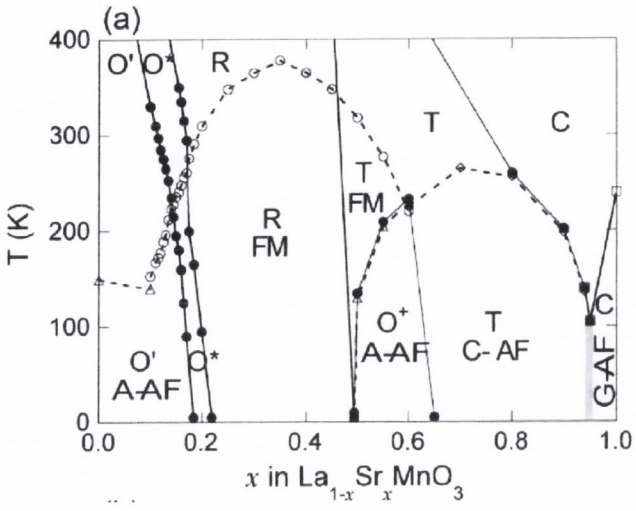

Figure 4.5: Experimental phase diagram of cubic $La_{1-x}Sr_xMnO_3$ [130].

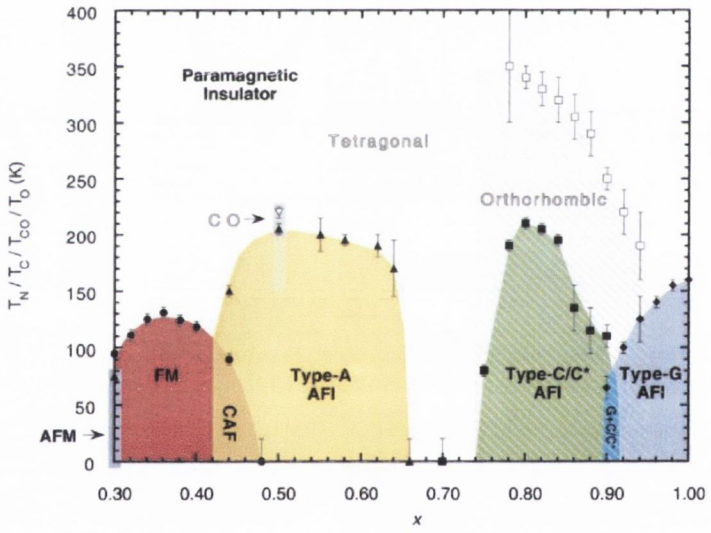

Figure 4.6: Experimental phase diagram of bilayer $La_{2-2x}Sr_{1+2x}Mn_2O_7$ [109]. Solid points mark magnetic transitions determined from neutron powder-diffraction data. Open points mark crystallographic transitions.

magnetic and crystallographic phases can occur by varying temperature T and hole-doping fraction x. At low hole-doping, the antiferromagnetic metal (AFM) present at $x = 0.3$ becomes ferromagnetic. There is even a charge-ordered (CO) phase for the half-doped ($x = 0.5$) system $LaSr_2Mn_2O_7$, for a temperature range above the Neel temperature T_N. A variety of antiferromagnetic ordering types are present.

Double Exchange and Colossal Magnetoresistance

What mechanism is behind the magnetic and metal-insulator transitions that are seen in the phase diagrams of both the cubic and bilayer LSMO? The traditional starting point for understanding the electronic and magnetic properties of manganites is the double-exchange mechanism, originally studied by Zener [131], deGennes [132] and Anderson and Hasegawa [73]. Double exchange says that the hopping probability t for an e_g electron to hop from one Mn site to the next is $t = t_0 \cos\theta/2$, where t_0 is the bare hopping probability and θ is the relative angle between two 'core' (t_{2g}) spins. This assumes that the three spin-aligned t_{2g} electrons may be treated as a core spin with $S = 3/2$ (see Figure 4.4, panel (c)). A ferromagnetic sample therefore has a full hopping probability, while an antiferromagnetic sample has $\theta = \pi$ and no probability of hopping. The paramagnetic case corresponding to $T \geq T_c$ can be approximated by $\theta = \pi/2$, meaning that t should be reduced to $\cos(\pi/4)$, or about 70% of its original value. A calculation of the bandwidth (W) change with temperature was done more precisely by Kubo [133], with the result being very similar to the above simple explanation.

However, the double exchange model is not sufficient in a number of respects - in particular, its ability to describe the magnitude of the *Colossal Magnetoresistance* (CMR) effect observed in manganites. This effect, first discovered by Jin [134], is the large magnetic field-induced drop in resistance in which occurs in certain manganites in their high-temperature paramag-

netic phase, near the paramagnetic insulator/ferromagnetic metal transition temperature T_C. The metal-insulator transition is brought on by the application of the magnetic field. Though originally discovered in the cubic compounds, this CMR effect is in fact greater in the bilayered manganite series, in the doping region from $x = 0.3$ to 0.5 [135]. CMR is still not fully understood theoretically. Theoretical ideas advanced towards an explanation include possible phase separation into inhomogeneous magnetic phases [5], and bipolaronic conductivity [136].

ARPES Experiments

Recently there has been an upsurge in experimental activity on the $n = 2$ bilayer manganite series $La_{2-2x}Sr_{1+2x}Mn_2O_7$. Angle-resolved photoemission spectroscopy (ARPES) experiments offer the prospect of determining single-particle spectral functions $A(\mathbf{k}, \omega) = (1\backslash\pi)\mathrm{Im}G(\mathbf{k}, \omega)$ (see Chapter 2), which when integrated over all momenta (i.e. over the Brillouin zone) gives the density of states (DOS). ARPES has been widely used in the study of high-temperature superconductors [19] and has proven to be a very powerful tool for probing the electronic structure. The principal experimental outputs obtained are the Energy Distribution Curves (EDCs) and Momentum Distribution Curves (MDCs). EDCs are plots of intensity, closely related to $A(\mathbf{k}, \omega)$, versus Binding Energy $(E - E_F)$, at a fixed emission angle. MDCs comprise of intensity versus emission angle at fixed binding energy. By taking a large number of EDCs at different emission angles and considering the spectral weight near the Fermi energy, it is possible to obtain experimental plots of the 2d Fermi surface. Estimates of the effective mass m^*, Fermi velocity v_F, and mean free scattering time τ can also be obtained from the ARPES dispersion, allowing an estimate of the Drude conductivity to be calculated from ARPES parameters [112].

A characteristic feature of ARPES Fermi surface plots for HTSC cuprates

is the marked dichotomy between spectral density along the antinodal $(0,0)$ and $(0,\pi)$ lines in the Fermi surface, and the nodal $(0,0)$ to (π,π) diagonal directions [19]. The maximum energy gap occurs along the antinodal direction (parallel to the Cu-O bonds) and vanishes along the nodal direction. In the superconducting phase, this is commonly assumed to derive from the d-wave pairing of quasiparticles which mediate the superconductivity. Above T_c, in the 'normal' phase, part of the Fermi surface remains 'gapped out'; gapless nodal points at $(0,\pi)$ on the Fermi surface, associated with the superconducting state, become spread out to occupy finite disconnected segments known as Fermi arcs [116]. This is the famous pseudogap phase of the cuprates, usually believed to be either a competing or precursor order associated with the d-wave superconductivity below T_c.

ARPES experiments on Bi2212 by Kanigel et al [116] have hinted that the pseudogap anisotropy and associated Fermi arcs depend only on the ratio $T/T^*(x)$, where $T^*(x)$ is the temperature below which the pseudogap first develops. Thus, the arcs may collapse linearly as $T \rightarrow 0$. This suggests that the $T = 0$ pseudogap state is a nodal liquid - a metallic state whose gapless excitations exist only at points in k-space, just like the nodal points in a d-wave superconducting state.

Recent ARPES experiments [113] on the $x = 0.4$ bilayer manganite have in fact demonstrated a similar nodal-antinodal dichotomy in the near-E_F spectral intensity, leading to a pseudogapped Fermi surface. This is quite remarkable in that such behaviour was hitherto considered intrinsic to the HTSCs and their d-wave superconducting state. These observations have given rise to the speculative hypothesis that the LSMO family are 'nodal metals' with nodal quasiparticles, analagous to the HTSCs, implying that the Fermi surface pseudogap features are not unique to the HTSCs. This has even led to a suggestion of the possibility of latent d-wave spin triplet superconductivity in this class of manganites [137]. This spin triplet state

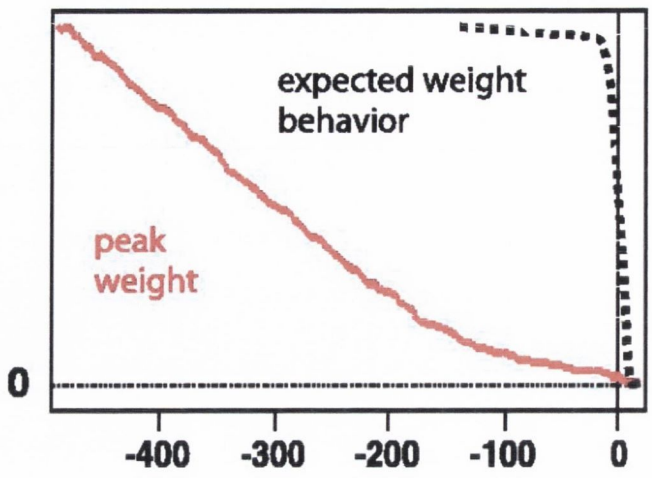

Figure 4.7: $La_{1.2}Sr_{1.8}Mn_2O_7$ ARPES spectral weight versus binding energy (red line). The black line indicates the expected weight behaviour for a non-interacting theory [112].

for a d-wave pair is hypothesized to arise from the orbital degrees of freedom. The superconductivity is, however, kept dormant by some intrinsic strong Cooper pair breaking processes. A pseudogap is also visible as a marked suppression in spectral weight over that expected for a normal metal, as shown in Figure 4.7 taken from Chuang et al [112].

Other ARPES studies [138],[114] did not reveal any coherent nodal or other quasiparticles in the pseudogapped state of the $x = 0.4$ compound. For the $x = 0.36$ and $x = 0.38$ systems, these ARPES studies found *antinodal* quasiparticle signatures: namely, quasiparticle peaks were seen around the $(0, \pi)$ point, which is thus non-gapped. This mitigates against the 'nodal metal' idea as being a general phenomenon for LSMO bilayer systems outside of the $x = 0.4$ case. Further ARPES studies by Saitoh et al [110] have even called into question the importance of the double exchange mechanism in the $x = 0.4$ bilayer, based on the minimal change in bandwidth which occurs across the ferromagnetic/paramagnetic phase transition.

Motivated by these reports of strong similarities between the $x = 0.4$ system and the HTSCs, we have studied the $x = 0.5$ bilayer manganite $LaSr_2Mn_2O_7$. The magnetic structure of the $La_{2-2x}Sr_{1+2x}Mn_2O_7$ series switches from ferromagnetic at $x = 0.4$ to A-type antiferromagnetic as we increase the doping fraction to $x = 0.5$ holes per La, as shown in the experimental phase diagram [109] in Figure 4.6. This system remains relatively unexplored experimentally and theoretically. To the best of our knowledge, no ARPES study of the $x = 0.5$ system currently exists. Our ab-initio calculations show a small but finite density of states at the Fermi level, and further show that the conduction band is highly anisotropic, existing in the 2-dimensional MnO_2 layers which are stacked along the z-axis in this material.

Further Photoemission Results for $LaSr_2Mn_2O_7$

We are interested in the effect of further hole doping into the Mn e_g band as we move from $x = 0.4$ to $x = 0.5$ holes per Mn site. An X-ray photoemission spectroscopy (XPS) study [139] of $La_{1.2}Sr_{1.8}Mn_2O_7$ and $LaSr_2Mn_2O_7$ revealed that the spectral features of the O $1s$, Mn $2p$ and valence band spectra are shifted by ~ 0.2 eV towards the Fermi level going from $x = 0.4$ to $x = 0.5$. This is shown in Figure 4.8. The spectral weight at E_F was suppressed both at 300K and 90K, consistent with ARPES studies for $x = 0.4$ [111],[112][113]. This was explained by the hole doping in the e_g band. Our density of states calculations show that this Mn e_g density around the Fermi level is primarily of $d_{x^2-y^2}$ character, i.e. in the plane of the MnO_2 layers. The same photoemission measurements on valence band, O $1s$ and Mn $2p$ were performed with the samples illuminated with laser light. This caused only minor shifts on the valence band and Mn $2p$ spectra in all cases except the O $1s$ spectrum for $x = 0.5$. While the O $1s$ spectrum of the $x = 0.4$ sample is shifted by 0.1 eV to higher binding energy, that of $x = 0.5$ is

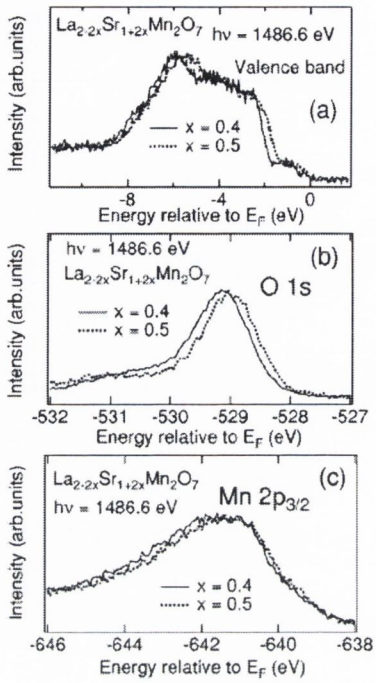

Figure 4.8: XPS spectra of (a) valence band (b) O 1s (c) Mn 2p of $x = 0.4$ and $x = 0.5$ taken at 300K [139].

shifted by 0.7 eV. The authors propose that the hybridisation between Mn and oxygen is considerably changed by the laser illumination, leading to an electronic structure change that is frozen by some lattice distortion. In addition, Chuang et al have suggested in their high-resolution ARPES study [112] that the e_g band of the $x = 0.4$ system is strongly renormalised by the electron-lattice interaction, causing the spectral weight to be considerably suppressed [112] and thus creating the pseudogap spectrum. Both of these experimental observations, as well as the well-known role of Jahn-Teller distortion in cubic manganites [18], suggest the importance of electron-lattice coupling in the layered magnetoresistive oxides. To our knowledge, there are no ab-initio lattice studies of $La_{2-2x}Sr_{1+2x}Mn_2O_7$ compounds. We have therefore performed structure optimisation calculations to test how the den-

sity of states and, by inference, the photoemission spectrum, is affected by lattice relaxation.

At present, research on trilayer manganites, corresponding to the chemical formula $La_{3-3x}Sr_{1+3x}Mn_3O_{10}$, is still relatively in its infancy, in part due to the the challenges of chemical synthesis of this class of compounds [140].

First Principles Calculations

The first ab-initio study of $LaSr_2Mn_2O_7$ was by de Boer and de Groot [141] using GGA. They found that the strong anisotropy of the crystal structure was reflected in the band structures, which showed dispersion in the MnO_2 plane direction and almost no dispersion in the ΓZ line parallel to the bilayer stacking direction. A half-metallic ferromagnetic ground state was found. A second LDA study [142] also found this ground state, in contradiction to later neutron diffraction studies [143],[109], which found antiferromagnetic order in the low-temperature phase of $LaSr_2Mn_2O_7$. This most likely results from an insufficient treatment of electronic correlation inherent in the DFT methods adopted by these authors, as discussed in Chapter 2.

Many of the statements in the literature about doped Mott insulators which are intended to refer to the cuprates in fact hold equally well for the layered manganites. The systems share several distinctive features: strong correlation, effective 2-dimensionality, proximity to an AF Mott insulating state, electron/hole-doping asymmetry, phase separation [5], stripes and dynamic inhomogeneity, pseudogapped Fermi surface [113], possibly nodal quasiparticles [114], to name a few. An understanding of the layered manganites as 2d doped Mott insulators with a pseudogap feature in their spectral weight at E_F [110],[139] and 'gapped out' Fermi surface [113] would be a highly worthy endeavour in itself and lend key insight into the CMR effect; in addition, a comparative study of the pseudogap physics in both mangan-

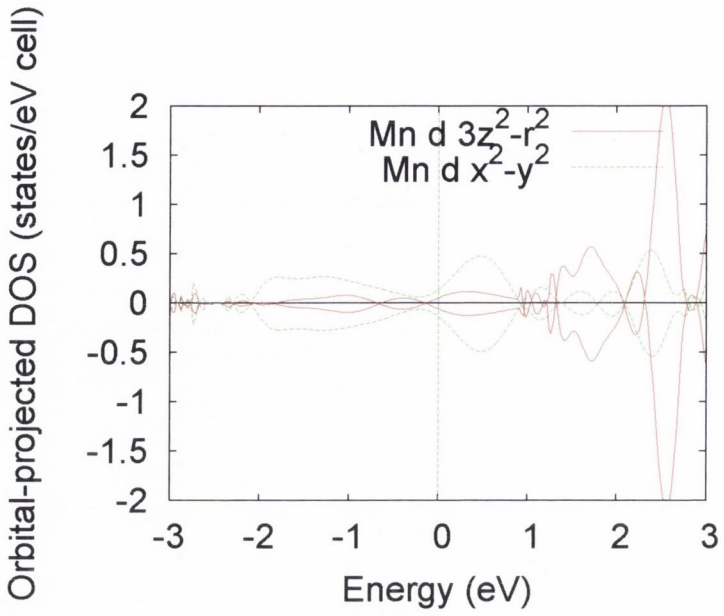

Figure 4.9: $LaSr_2Mn_2O_7$ Mn e_g orbital projected density of states at 30% exchange (lowest energy antiferromagnetic solution).

ites and cuprates may help to identify those features which are unique to cuprates and which may have some bearing the anomalous "normal" state in the HTSCs, an understanding of which is crucial for unravelling the high-T_c superconducting mechanism.

4.2 Results

Calculations were performed using the CRYSTAL code [41], starting from the experimental crystal structure determined by Kubota et al using neutron powder diffraction [143]. A hybrid B3LYP scheme with 30% Hartree-Fock exchange was adopted. The crystal structure of $LaSr_2Mn_2O_7$ is shown in Figure 4.14. We firstly considered the question of the exact magnetic structure of $LaSr_2Mn_2O_7$. Total energy calculations were obtained for three different spin arrangements, in order to determine the correct magnetic ground state for this system. We firstly investigated A-type antiferromagnetism,

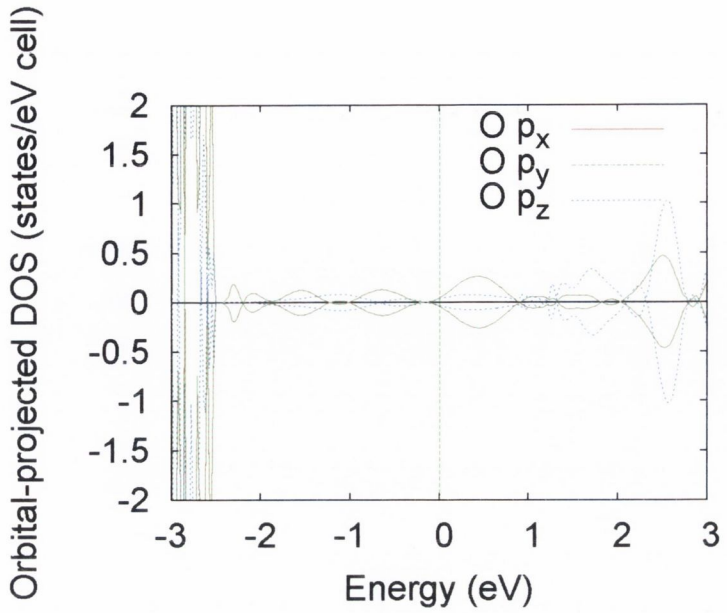

Figure 4.10: $LaSr_2Mn_2O_7$ oxygen p orbital projected density of states at 30% exchange (lowest energy antiferromagnetic solution).

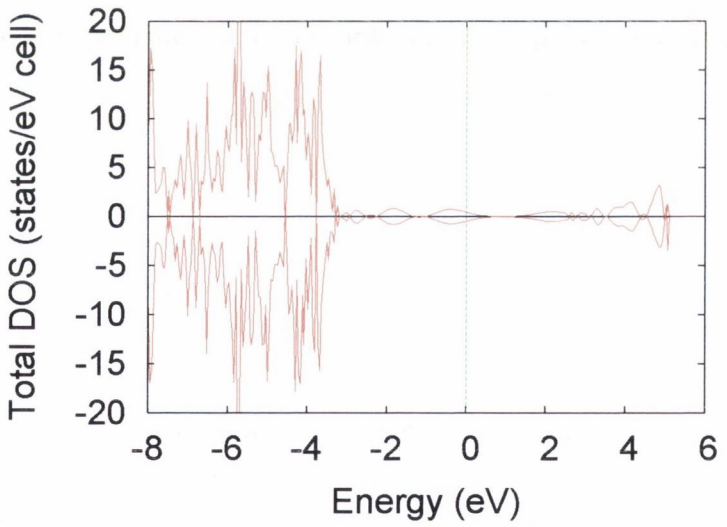

Figure 4.11: $LaSr_2Mn_2O_7$ total density of states at 60% exchange (lowest energy antiferromagnetic solution).

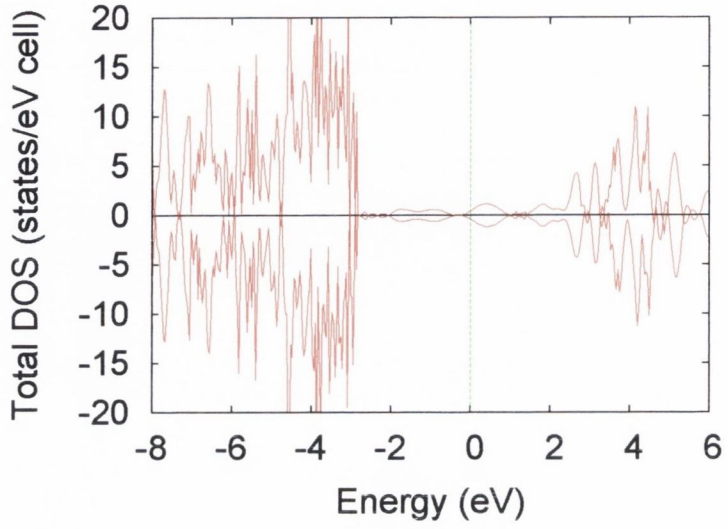

Figure 4.12: Optimised structure total density of states at 30% exchange.

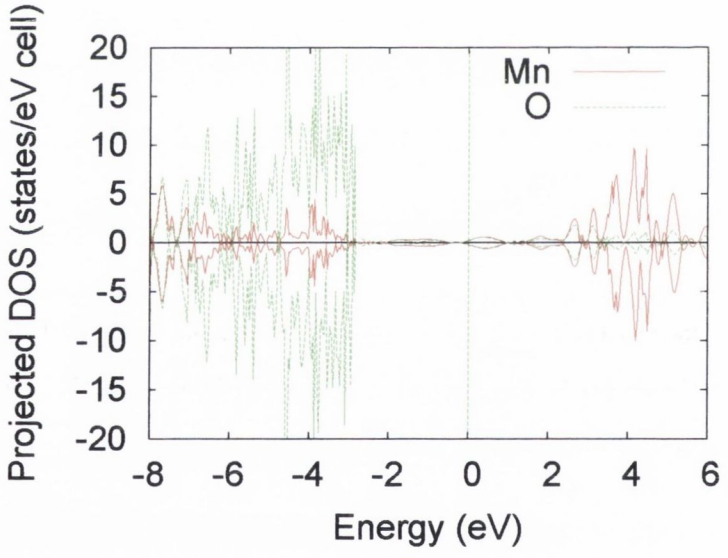

Figure 4.13: Optimised structure projected density of states at 30% exchange.

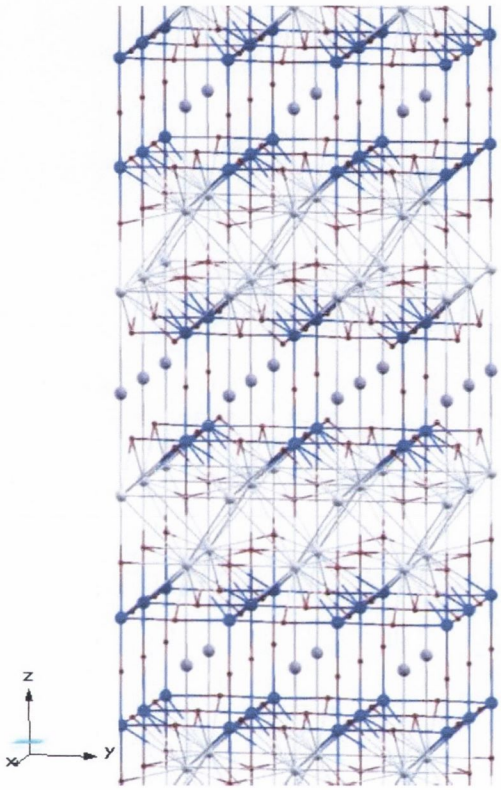

Figure 4.14: $LaSr_2Mn_2O_7$ lattice. Mn bilayers are shown in blue. Intra-bilayer intercalation is by La ions (purple). The inter-bilayer spacing contains Sr ions (grey).

with AF coupling both between individual MnO_2 layers within a bilayer (intra-bilayer coupling), and between the bilayers themselves (inter-bilayer coupling), as shown in Figure 4.14. Secondly, we investigated A-type antiferromagnetism with *ferromagnetic* inter-bilayer coupling i.e. the bottom layer of spins in one bilayer is aligned with the top of the bilayer below it. We lastly obtained results for the ferromagnetic system, with FM coupling between all layers. This was the magnetic ground state obtained in previous LSDA [141], [142] and self-consistent KKR studies [144], which predicted half-metallicity. In all cases, coupling between Mn ions in a single 2d MnO_2 plane is ferromagnetic. The highest energy solution was the first case above, with AF coupling both in bilayers and between bilayers. We found that the ferromagnetic solution was lower in energy by 11 meV/formula unit. However, this is not in fact the ground state, as we find that our third solution, with AF intra-bilayer and FM inter-bilayer coupling, is in fact the lowest in energy, around 9 mev/fu lower than the FM case. As is well documented, LSDA copes poorly with strongly correlated transition metal oxides. The incorporation of Hartree-Fock exchange in our hybrid DFT approach allows the experimentally determined antiferromagnetic ground state [109], [143] to be obtained. This is also consistent with the LSDA+U study of this system by Medvedeva et al [145]. However, we have shown that the inter-bilayer magnetic coupling orientation plays a significant role in determining the ground state energies, and that bilayers must be coupled *ferromagnetically*, with AFM coupling between individual layers in a bilayer, to obtain the lowest energy AFM solution.

The electronic band structure has been calculated at 30% exchange, as shown in Figure 4.15. Our plot shows a single dispersive band crossing the Fermi energy, indicating a highly delocalised conduction band character. This band has significant width, of around 6 eV. We have analysed the conduction band character at three points in the IBZ. At Γ, below E_F, this band

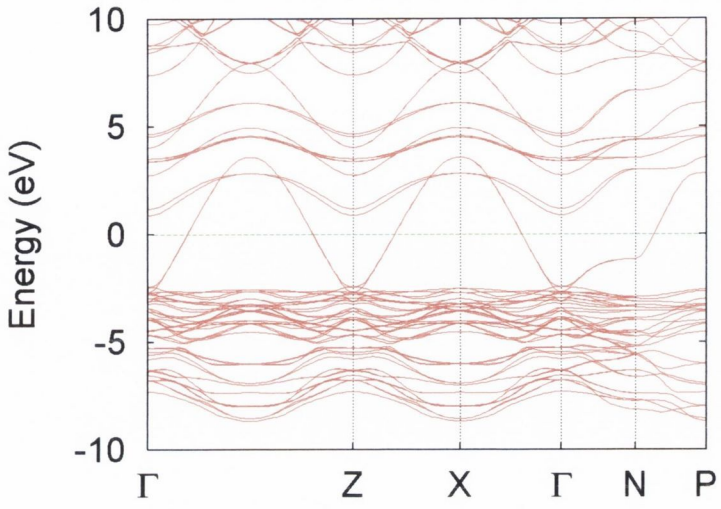

Figure 4.15: $LaSr_2Mn_2O_7$ electronic band structure at 30% exchange (lowest energy antiferromagnetic solution).

is predominantly of oxygen p_y character. Moving along in Γ-Z direction, at 1.9 eV above E_F, the band contains Mn $3z^2 - r^2$ e_g orbital character, with some in-plane Mn $x^2 - y^2$ e_g mixing. We also consider the X high-symmetry point. Here the conduction band has been crossed by a more dispersive band at 0.75 eV below. The band under consideration now displays strong $x^2 - y^2$ character, while the new band below it is predominantly $3z^2 - r^2$.

The corresponding density of states plot is shown in Figure 4.17. The first point to note is that our DOS graph shows a significant reduction in carrier density around E_F. This is compatible with high-resolution ARPES studies of the $x = 0.4$ compound [112], [113], which showed a significant decrease in spectral weight of the one-particle spectral function $A(\mathbf{k}, \omega)$ over a large energy scale (nearly 0.5 eV) as the dispersive peak approaches E_F. ARPES directly provides information about the momentum-resolved single-particle spectral function $A(\mathbf{k}, \omega)$, which when integrated over all momenta gives the density of states. This is not expected in the simple theory of

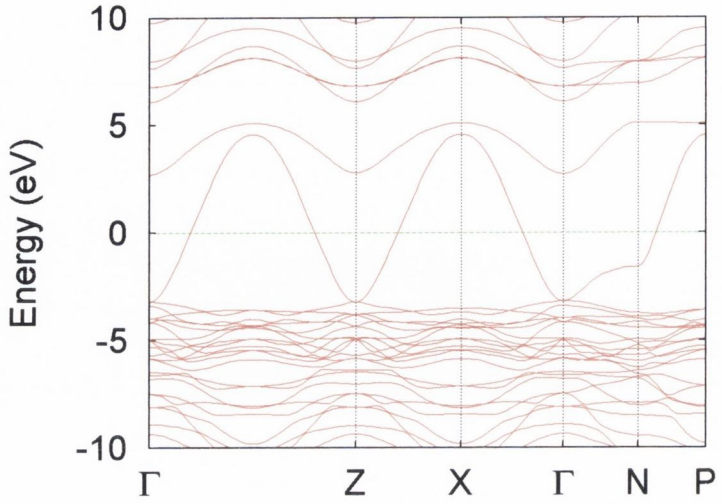

Figure 4.16: $LaSr_2Mn_2O_7$ antiferromagnetic electronic band structure at 60% exchange (lowest energy antiferromagnetic solution).

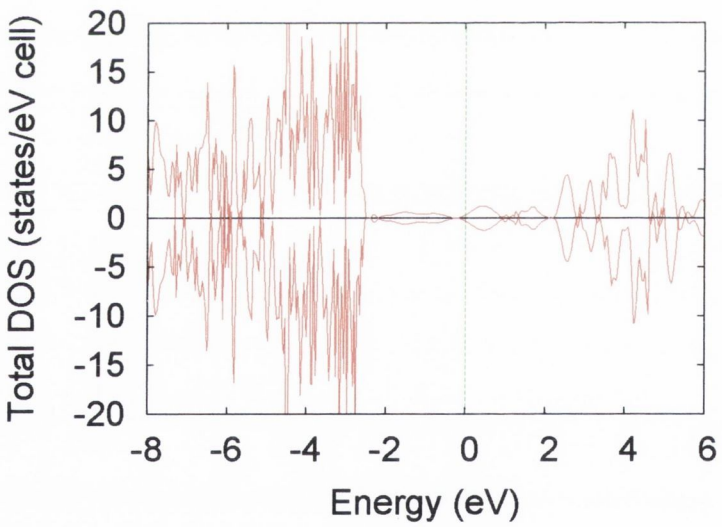

Figure 4.17: $LaSr_2Mn_2O_7$ total density of states at 30% exchange (lowest energy antiferromagnetic solution).

metals, where the spectral weight remains relatively constant until cut by the the Fermi energy. Figure 4.7 shows the actual peak weight for the pseudogapped $x = 0.4$ compound versus the expected peak shape for a normal metal. Thus we find the half-doped bilayer manganite $LaSr_2Mn_2O_7$ to be an antiferromagnetic metal, albeit one with a low carrier density at E_F.

Band structure and DOS calculations were also carried out with 60% HF exchange. This contains a relatively large proportion of bare HF exchange and should be sufficient to open a gap in many strongly correlated transition metal oxides, where LSDA alone would not. Most of conduction bands are pushed upwards, as would be expected from the extra exchange mixing. The upwards shift in these conduction bands is accompanied by a large reduction in their density, as shown in the 60% DOS plot in Figure 4.2. However, the system remains metallic since the dispersive band crossing the Fermi energy in the 30% calculation is only slightly affected by the large increase in HF exchange mixing. There is in fact a slight increase in this band's dispersion - perhaps somewhat unexpectedly, since the increase in Coulomb repulsion due to extra exchange mixing would normally serve as an electron-localising influence, leading to band narrowing. The E_F-crossing band clearly has significant implications for the Fermi surface and physics of this system. The apparent robustness of this band in the face of a large increase in exchange is most likely a dimensional effect, due to the reduced effective dimensionality of the system caused by the MnO_2 layered structure.

It is therefore worth further investigating exactly which orbitals are involved at the Fermi surface. Figures 4.2 and 4.2 show atomic orbital resolved DOS plots for Mn and O ions, with the scale expanded for better resolution around E_F. We found that La and Sr states did not feature around E_F and for clarity were not included in this plot. Interestingly, there is a clear predominance of in-plane Mn $x^2 - y^2$ e_g orbital density over Mn $3z^2 - r^2$

e_g. This orbital features lobes which point directly at neighbouring in-plane oxygen p_x and p_y lobes in the xy-plane. The $3z^2 - r^2$ e_g orbital points along the z-axis to the apical oxygens' p_z-orbital lobe in the MnO_6 octahedron. Our oxygen p orbital-resolved plot shows that p_x and p_y orbitals are of the same density around E_F. This is to be expected by symmetry; both p_x and p_y lobes should have the same overlap with Mn $x^2 - y^2$ without preference for a given direction in the xy-plane, since all xy-plane Mn-O bond lengths are equal in this structure [143]. Both O p_x and p_y are predominant over p_z. This orbital arrangement is in fact similar to that of the cuprates CuO_2 planes - there the highest partially occupied Cu d-orbital in $x^2 - y^2$ with lobes pointing directly to the p_x and p_y orbitals of neighbouring oxygens [14].

Figure 4.18 shows the Fermi surface for $LaSr_2Mn_2O_7$. This calculation was performed using the Exciton program [146], beginning with our lowest energy antiferromagnetic solution at 30% HF exchange mixing. The area in the box is a slice of the Brillouin zone. We see a square feature centred on Γ, corresponding to an electron pillar mainly of $d_{x^2-y^2}$ character. The segments seen neighbouring the Brillouin zone slice are simply reflections also centred on Γ. In our band structures (Figures 4.15 and 4.16), this Fermi surface pillar is crossed between Γ and X. A similar feature is seen in experimental Fermi surfaces for the $x = 0.4$ manganite $La_{1.2}Sr_{1.8}Mn_2O_7$, obtained using ARPES [112], [113]. These demonstrate the highly two-dimensional nature of this system.

Overall, we have a clear picture of enhanced carrier density and conductivity in the 2d xy-plane, with reduced conductivity along the z-axis, confirming the effective 2d character of this system , particularly when compared to the $n = \infty$ perovskite manganites. This will also have some bearing on the inter-bilayer magnetic coupling. As previously discussed, a candidate mechanism for ferromagnetism is the double exchange model, though the

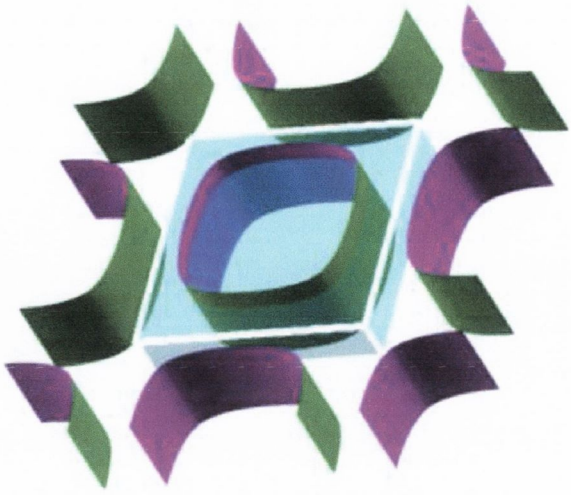

Figure 4.18: $LaSr_2Mn_2O_7$ Fermi surface, starting from our lowest energy antiferromagnetic solution at 30% HF exchange mixing.

importance of DE in the 2-dimensional case has been called into question by ARPES experiments [110]. Ferromagnetic intrabilayer couplings seen in the $x = 0.4$ case, will compete with the superexchange interaction, which promotes the antiferromagnetic intrabilayer coupling that wins out in the $x = 0.5$. This implies that the extra hole doping in the Mn band promotes superexchange over double exchange along the bilayer z-axis.

Populations

Table 4.1 shows Mulliken charge and spin populations. We find no charge ordering on Mn ions, consistent with experimental studies of the low-temperature phase [109]. This is also consistent with the experimental space group and lattice parameters chosen, which were taken from a neutron powder diffraction study at 10K [143], comfortably below the 100K threshold where charge ordering is believed to occur [147],[109],[148]. We also investigated the effects of using a biased Mn 3+/4+ integer charge ordered starting point, and

Table 4.1: Charge and spin states for $LaSr_2Mn_2O_7$ at 30% exchange. Values are shown for the experimental and the optimised structures.

Atom	Valence	Valence^{Opt}	Moment $/\mu_B$	Moment^{Opt} $/\mu_B$
Mn1	+1.86	+1.86	3.61	3.57
Mn2	+1.86	+1.86	-3.60	-3.56
La	+2.82	+2.82	0.00	0.00
Sr1	+0.14	+0.15	0.00	0.00
Sr2	+0.14	+0.15	0.00	0.00
O1	-1.53	-1.50	0.00	0.00
O2a	-1.46	-1.46	-0.08	-0.02
O2b	-1.46	-1.46	0.08	0.02
O3a	-1.46	-1.46	0.02	0.02
O3b	-1.46	-1.46	-0.02	-0.02
O3c	-1.46	-1.46	-0.02	-0.02
O3d	-1.46	-1.46	0.02	0.02

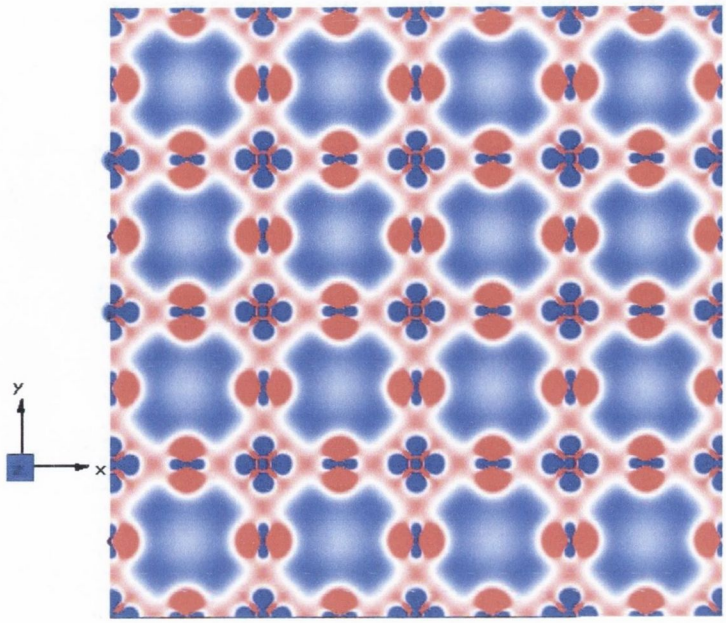

Figure 4.19: MnO_2 plane charge density difference at 30% exchange.

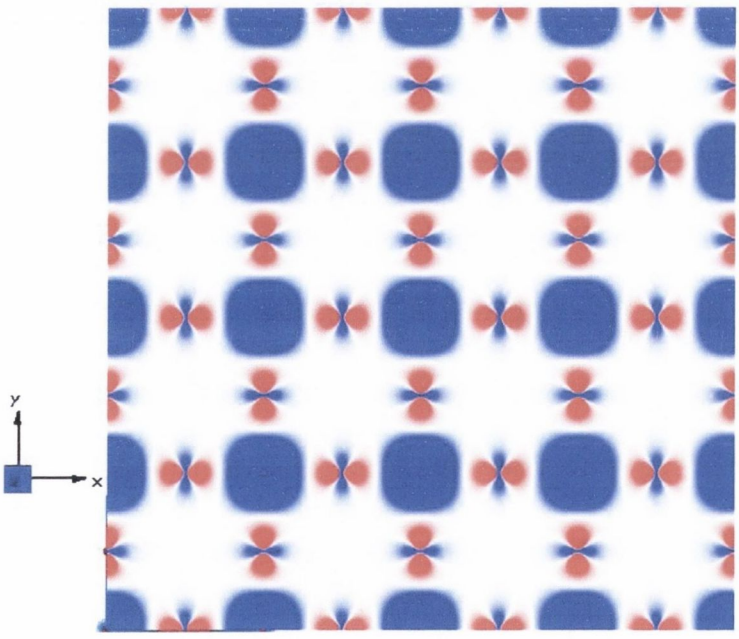

Figure 4.20: MnO_2 plane spin density difference at 30% exchange.

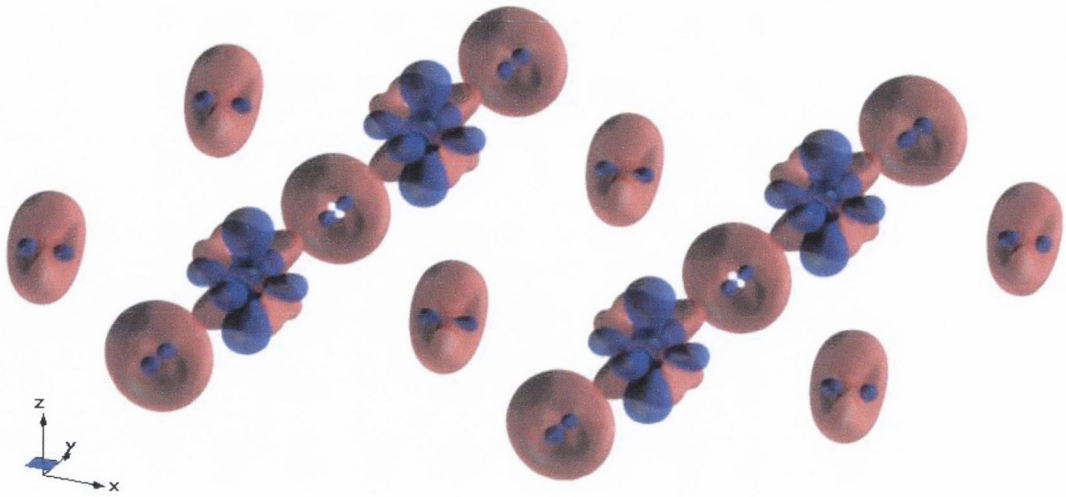

Figure 4.21: MnO_2 plane 3d charge density difference at 30% exchange.

found that it had no effect on the final populations shown in Table 4.1, thus showing that the populations obtained have not been biased by our calculation's initial conditions. Most ab-initio studies have not given populations; the LSDA study of de Boer [141] reported an Mn valence of +2.7, though the LSDA's failure to account adequately for the effects of strong electronic correlation means that this half-metallic FM solution does not reflect the correct experimental AF ground state [109],[148]. Experimental estimates of populations via Bond Valence Sums or otherwise have not to our knowledge been reported. Our calculated Mn populations are less than their idealised ionic value of +3.5, reflecting the trend towards *p-d* hybridisation and increased covalence seen around the Fermi energy in our band structure and DOS graphs. In addition, we do not find orbital order on Mn sites. This can be seen graphically in Figure 4.19, which shows a 2-dimensional charge density difference plot, in the plane of an MnO_2 layer. This plot was obtained by taking our calculated charge density and subtracting a linear superposition of atomic orbitals. Areas in blue indicate negative difference and areas in red indicate positive difference. In effect, this means that cation orbitals

with higher occupation numbers will appear more blue, and more occupied anion orbitals will appear more red. Figure 4.20 shows the corresponding spin density difference plot. Finally, in Figure 4.21, we have projected our calculated charge density difference into a 3-dimensional view. The Mn e_g orbital lobes in the xy-plane can be seen to point directly at neighbouring oxygens. The smaller weight in the in-plane blue lobes, relative to the lobe pointing along the z-axis, may be due to the increased hybridisation with oxygen p orbitals in the plane. We do not see the Mn t_{2g} orbitals, whose lobes would point diagonally between oxygen ions.

Structure Optimisation

We investigate the role of electron-lattice coupling in this system by performing an optimisation of the structure, beginning from our above solution. This is, to our knowledge, the first ab-initio structure study of any $La_{2-2x}Sr_{1+2x}Mn_2O_7$ system. Table 4.2 shows the atomic coordinates for the experimental [143] and optimised cell. 1 Mn and 3 Mn are in opposite layers in a bilayer, while 2 Mn and 4 Mn are in another bilayer, which is shifted relative to the bilayers above and below it, as can be seen in Figure 4.14. There are 3 kinds of oxygen symmetry positions associated with every Mn-O octahedron: type(I) apical oxygens inside a bilayer, with Mn's above and below (11 O and 12 O), type(II) apical oxygens outside a bilayer (13-16 O), and type(III) oxygens in the 2d MnO_2 xy-planes (17-24 O).

Following our ab-initio structure optimisation, the pattern of lattice relaxation of the experimental structure may be discerned as follows. Type(I) apical oxygens inside the bilayer are symmetry-constrained and do not move during the structure optimisation. Type(II) apical oxygens move straight downwards along the z-axis towards the Mn ion to which they are attached in an MnO_2 layer. The entire MnO_2 layer, consisting of Mn and type(III) oxygens, shifts as a whole layer away from the type(I) apical oxygens and

Table 4.2: Fractional atomic coordinates for experimental[143] and optimised structures at 30% exchange.

			Experimental		30% optimised	
Atom	x	y	z	x	y	z
1 Mn	0	0	0.0970	0	0	0.0988
2 Mn	-1/2	-1/2	-0.4030	-1/2	-1/2	-0.4013
3 Mn	0	0	-0.0987	0	0	-0.0970
4 Mn	-1/2	-1/2	0.4030	-1/2	-1/2	0.4013
5 La	-1/2	-1/2	0	-1/2	-1/2	0.0005
6 La	0	0	-1/2	0	0	-1/2
7 Sr	-1/2	-1/2	-0.1826	-1/2	-1/2	-0.1838
8 Sr	0	0	0.3174	0	0	0.3162
9 Sr	-1/2	-1/2	0.1826	-1/2	-1/2	0.1838
10 Sr	0	0	-0.3174	0	0	-0.3162
11 O	0	0	0	0	0	0
12 O	-1/2	-1/2	-1/2	-1/2	-1/2	-1/2
13 O	0	0	0.1965	0	0	0.1939
14 O	-1/2	-1/2	-0.3035	-1/2	-1/2	-0.3061
15 O	0	0	-0.1965	0	0	-0.1939
16 O	-1/2	-1/2	0.3035	-1/2	-1/2	0.3061
17 O	0	-1/2	0.0949	0	-1/2	0.0930
18 O	-1/2	0	-0.4051	-1/2	0	-0.4070
19 O	0	-1/2	-0.0949	0	-1/2	-0.0930
20 O	-1/2	0	0.4051	-1/2	0	0.4070
21 O	-1/2	0	-0.0949	-1/2	0	-0.0930
22 O	0	-1/2	0.4051	0	-1/2	0.4070
23 O	-1/2	0	0.0949	-1/2	0	0.0930
24 O	0	-1/2	-0.4051	0	-1/2	-0.4070

towards the type(II) apical oxygens and the Sr atoms. In other words, the spatial gap between the two layers in the bilayer is increased. This is shown schematically in Figure 4.22. This also implies that no significant twisting or buckling of Mn-O octahedra occurs following the lattice relaxation, in marked contrast to the Fe-O octahedra in our study of Fe_3O_4. There is a very small buckling of the MnO_2 layer, due to fact that the Mn moves along z by 0.002 Å less than its four in-plane oxygen neighbours, but this is very minor when compared to the existing z-axis displacement of Mn relative to O in the experimental structure [143]. All in-plane Mn-O bond distances remain identical to each other, with a marginal increase from 1.9370 Å experimental to 1.9399 Å in the optimised structure. The Jahn-Teller (JT) distortion of Mn-O octahedra, i.e. the ratio of the averaged apical Mn-O bond length to the equatorial bond Mn-O length is reduced from $\Delta_{JT} = 1.010$ (experimental) to $\Delta_{JT} = 0.995$ (optimised).

Using the Isotropy code [79], we have determined that the above cell with two formula units has a $P4mm$ space group. This is the same space group that the doubled cell had before the optimisation, so we find no lattice symmetry breaking.

A look at the charge and spin populations in the optimised cell confirms this picture. Table 4.1 lists the populations of the optimised structure alongside those for the experimental structure. The Mn valence states at +1.86 are unchanged by optimisation. There is a 0.04 μ_B drop in magnetic moment on both of the AF-coupled Mn ions in a bilayer. This may result from the increased interbilayer separation in the optimised structure.

It would be interesting to see if the structure optimisation has much influence on the conduction band and DOS around the Fermi energy. Given that we find a conduction band character that is largely 2-dimensional in the MnO_2 planes, it would be reasonable to assume that a structure optimisation whose primary effect is a shift of the MnO_2 planes along the z-axis,

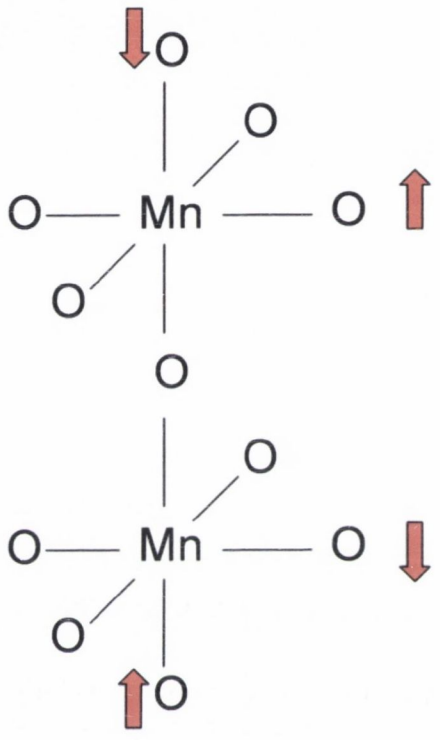

Figure 4.22: Schematic illustration of the effects of structure optimisation on an $LaSr_2Mn_2O_7$ bilayer.

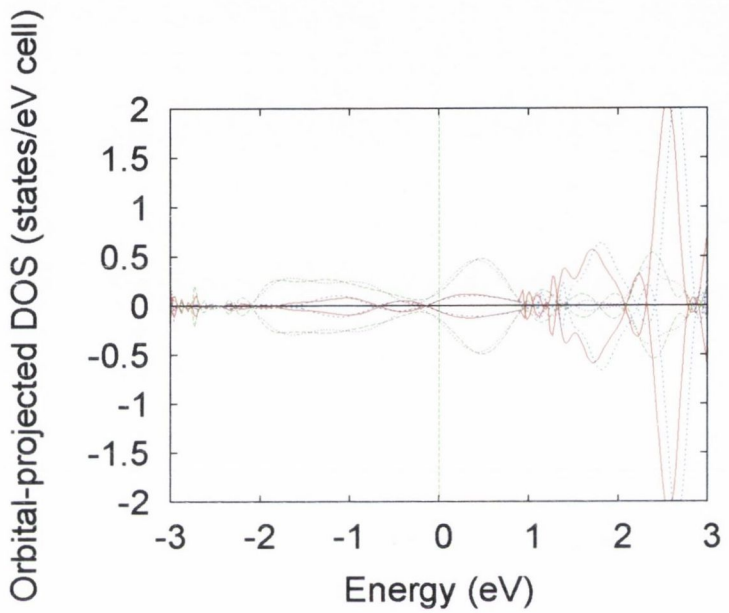

Figure 4.23: Comparison of Mn e_g states around E_F. Mn $d_{x^2-y^2}$ states for the experimental and optimised structures are shown in green and purple respectively, with $3z^2 - r^2$ states shown in red and blue.

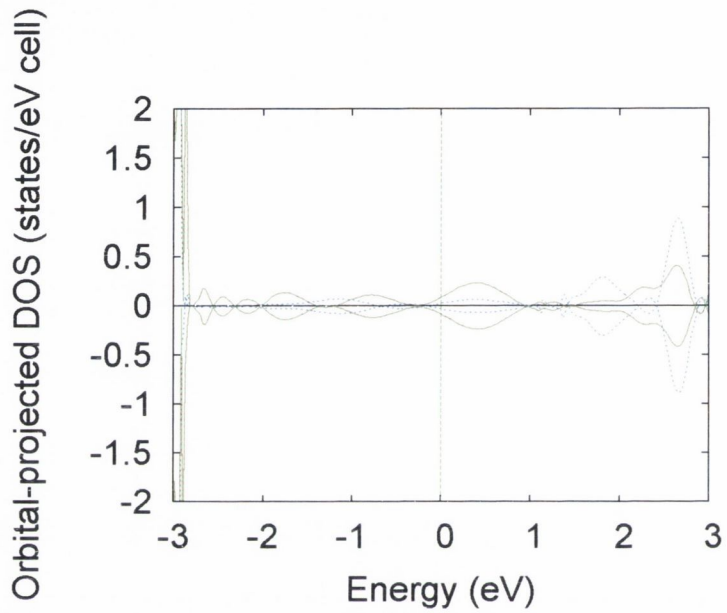

Figure 4.24: Comparison of O p states around E_F. Oxygen p_x, p_y and p_z states are shown in red, green and blue in the experimental structure, and purple, cyan and yellow in the optimised structure.

without significantly distorting them, would not cause a major change in the density of states around E_F. To investigate further, Mn e_g and O p atomic orbital-projected DOS plots have been calculated for the optimised structure. We previously calculated these densities for the experimental structure and plotted them in Figures 4.2 and 4.2. In Figures 4.23 and 4.24, the same densities for the optimised cell are plotted alongside the experimental cell densities for comparative purposes, in a ± 3 eV window around the Fermi energy. It can be seen that the structure optimisation has minimal effect on carrier densities in $LaSr_2Mn_2O_7$. Thus, we find that the magnitude and orbital character of the DOS at E_F remain remarkably robust under both lattice distortion and large increases in HF exchange (Figure 4.16).

Structure optimisations were also carried out for starting from our 60% HF exchange solution for this manganite system. The optimised structure was again found to retain $P4mm$ symmetry, the same space group as the experimental structure with two formula units.

4.3 Conclusion

As more hole doping occurs in the e_g band, moving towards $x = 0.5$, the JT distortion is reduced due to the change in the e_g orbital state [143]. This means that there is less $d_{3z^2-r^2}$ orbital overlap with type(I) oxygens inside bilayers, mitigating against a double exchange mechanism along the z-axis 1Mn-$O_{type(I)}$-3Mn bond and suppressing intrabilayer ferromagnetism. The increased separation of single MnO_2 layers in a bilayer in our optimisation would further mitigate against ferromagnetism between the single layers and promote antiferromagnetism via a type(I) apical oxygen-mediated superexchange mechanism. There is in fact very little change in the atomic coordinates resulting from the structure optimisation , pointing to good experimental resolution of the structure by Kubota et al [143].

Our total energy studies determined that antiferromagnetic intrabilayer

combined with ferromagnetic interbilayer coupling was the most favourable magnetic arrangement, in contradiction to previous LSDA studies [141], [142] which found ferromagnetism. This most likely resulted from LSDA's inadequate treatment of electron self-interaction.

We also note the significant degree of hybridization between oxygen p-states and Mn e_g states at the Fermi energy ,which is largely confined to the MnO_2 planes, in agreement with experimental resistivity results which show significant anisotropy between the ab-plane and c-axis directions [147]. Our calculated Fermi surface also exhibited significant two-dimensional character. All these signs indicate pseudogap behaviour very similar to that seen in the normal state of the superconducting cuprates, and seen experimentally as a suppression of spectral weight at E_F. This pseudogap will decrease the conductivity by removing a large portion of the carriers from the conduction process. We find that this AF pseudogap is robust with respect to structure optimisation of the equilibrium lattice geometry and significant increases of HF exchange of up to 60%. Such an effect may arise from structural considerations related to the effective low-dimensionality of this material.

Any statements about a normal state d-wave pseudogap with isolated nodal points and Fermi surface nesting being involved in the high-T_c superconducting mechanism should by rights also explain why the $x = 0.4$ bilayer manganite, which is very different from a superconductor, shows similar features its ARPES spectra. Given our findings of significant Mn $d_{x^2-y^2}$ conduction band character, reduced JT distortion and low density of states at E_F in the $x = 0.5$ case, it is felt that ARPES and STM studies of the $x = 0.5$ system $LaSr_2Mn_2O_7$ in both its low-temperature and charge-ordered phase above 100K would be a most worthwhile exercise.

Bibliography

[1] J. H. de Boer and E. J. W. Verwey, Proc. Phys. Soc. Lond. **49**, 59 (1937).

[2] S. Sachdev, cond-mat/0211027 (2002).

[3] F. Aryasetiawan and O. Gunnarsson, Rep. Prog. Phys. **61**, 237 (1998).

[4] A. S. Alexandrov, cond-mat/0508765 (2005).

[5] E. Dagotto, J. Burgy, and A. Moreo, cond-mat/0209689 (2002).

[6] E. J. Verwey, Nature **144**, 327 (1939).

[7] J. Garcia *et al.*, Phys. Rev. B **63**, 054110 (2001).

[8] F. Walz, J. Phys. Cond. Matt. **14**, 285 (2002).

[9] M. Iizumi *et al.*, Acta Crystallogr. B **38**, 2121 (1982).

[10] G. K. Rozenberg *et al.*, Phys. Rev. Lett. **96**, 045705 (2006).

[11] J. Wright, J. Attfield, and P. Radaelli, Phys. Rev. B **66**, 214422 (2002).

[12] J. R. Cullen and E. Callen, Phys. Rev. Lett. **26**, 236 (1971).

[13] D. Ihle and B. Lorentz, J. Phys. C: Solid State Phys. **18**, L647 (1985).

[14] P. Lee, N. Nagaosa, and X. Wen, Rev. Mod. Phys. **78**, 17 (2006).

[15] R. B. Laughlin and D. Pines, Proc. Nat. Acad. Sci. **91**, 28 (2000).

[16] S. Kivelson and E. Fradkin, cond-mat/0507459 (2005).

[17] P. W. Anderson, Science **288**, 480 (2000).

[18] J. M. D. Coey, M. Viret, and S. von Molnar, Adv. Phys. **48**, 167 (1999).

[19] A. Damascelli, Z. Hussain, and Z. X. Shen, Rev. Mod. Phys. **75**, 473 (2003).

[20] P. Hohenberg and W. Kohn, Phys. Rev. **136**, B884 (1964).

[21] A. D. Becke, Phys. Rev. A **38**, 3098 (1988).

[22] C. Lee, W. Yang, and R. G. Parr, Phys. Rev. B **37**, 785 (1988).

[23] A. Svane and O. Gunnarsson, Phy. Rev. Lett. **65**, 1148 (1990).

[24] V. I. Anisimov, F. Aryasetiawan, and A. I. Lichtenstein, J. Phys. Cond. Matt. **9**, 767 (1997).

[25] F. Aryasetiawan, K. Karlsson, O. Jepsen, and U. Schönberger, cond-mat/0603138 (2006).

[26] Y. S. Su, T. A. Kaplan, S. D. Mahanti, and J. F. Harrison, Phys. Rev. B **59**, 10521 (1999).

[27] S. Massida, M. Posternak, and A. Baldereschi, Phys. Rev. B **48**, 5058 (1993).

[28] X. Feng and N. M. Harrison, Phys. Rev. B **70**, 092402 (2004).

[29] A. D. Becke, J. Chem. Phys. **98**, 5648 (1993).

[30] L. A. Curtiss, K. Raghavachari, P. C. Redfern, and J. A. Pople, J. Chem. Phys. **105**, 1063 (1997).

[31] C. Adamo, M. Ernzerhof, and G. E. Scuseria, J. Chem. Phys. **112**, 2643 (2000).

[32] S. H. Vosko, L. Wilk, and M. Nusair, Can. J. Phys. **58**, 1200 (1980).

[33] T. V. Russo, R. L. Martin, and P. J. Hay, J. Chem. Phys. **102**, 8023 (1995).

[34] J. Muscat, A. Wander, and N. M. Harrison, Chem. Phys. Lett. **342**, 397 (2001).

[35] A. Yamasaki and T. Fujiwara, Phys. Rev. B **66**, 245108 (2002).

[36] S. V. Faleev, M. Schilfgaarde, and T. Kotani, Phys. Rev. Lett. **93**, 126406 (2004).

[37] A. D. Rowan and C. H. Patterson, Poster Presentation, GW 2005 Conference, Bad Honnef, Germany (2005).

[38] C. H. Patterson, Int. J. Quant. Chem. **106**, 3383 (2006).

[39] X. Feng and N. M. Harrison, Phys. Rev. B **69**, 132502 (2004).

[40] D. Munoz, N. M. Harrison, and F. Illas, Phys. Rev. B **69**, 085115 (2004).

[41] V. R. Saunders *et al.*, CRYSTAL2003 User's Manual, University of Torino, Torino (2003).

[42] H. B. Schlegel, J. Comp. Chem. **3**, 214 (1982).

[43] M. Alfredson *et al.*, Mol. Sim. **31**, 367 (2005).

[44] J. M. D. Coey and S. Sanvito, J. Phys. D: Appl. Phys. **37**, 988 (2004).

[45] D. I. Khomskii, J. Magn. Magn. Mat. **306**, 1 (2006).

[46] L. Néel, Ann. Phys. **3**, 137 (1948).

[47] M. Imada, A. Fujimori, and Y. Tokura, Rev. Mod. Phys. **70**, 1039 (1998).

[48] W. H. Bragg, Phil. Mag. **30**, 305 (1915).

[49] W. H. Bragg and G. Brown, Z. Kristallogr. **63**, 122 (1926).

[50] G. Parks and K. Kelley, J. Phys. Chem. **30**, 47 (1926).

[51] W. Hamilton, Phys. Rev. **110**, 1050 (1958).

[52] G. Shirane *et al.*, J. Phys. Soc. Japan **39**, 949 (1975).

[53] M. Mizoguchi, J. Phys. Soc. Japan **44**, 1501 (1978).

[54] J. Wright, J. Attfield, and P. Radaelli, Phys. Rev. Lett. **87**, 266401 (2001).

[55] N. Brese and M. O'Keefe, Acta Cryst. B **47**, 192 (1991).

[56] J. Garcia *et al.*, Phys. Rev. Lett. **85**, 578 (2000).

[57] G. Subias *et al.*, Phys. Rev. Lett. **93**, 156408 (2004).

[58] P. Novak *et al.*, Phys. Rev. B **61**, 1256 (2000).

[59] M. P. Pasternak *et al.*, J. Magn. Magn. Mater. **265**, 107 (2003).

[60] D. Schrupp, Europhys. Lett. **70**, 789 (2005).

[61] A. Chainani *et al.*, Phys. Rev. B **51**, 17976 (1995).

[62] J. H. Park *et al.*, Phys. Rev. B **55**, 12813 (1997).

[63] B. K. Chakraverty, Solid State Commun. **15**, 1271 (1974).

[64] Y. Yamada, Philos. Mag. B **42**, 377 (1980).

[65] N. F. Mott, Philos. Mag. B **42**, 327 (1980).

[66] S. K. Park, T. Ishikawa, and Y. Tokura, Phys. Rev. B **58**, 3717 (1998).

[67] A. Pimenov, S. Tachos, T. Rudolf, and A. Loidl, Phys. Rev. B **72**, 035131 (2005).

[68] J. C. Dyre and T. B. Schroder, Rev. Mod. Phys. **72**, 873 (2000).

[69] L. V. Gasparov *et al.*, Phys. Rev. B **62**, 7939 (2000).

[70] J. Li, G. Rignasse, and S. Louie, Phys. Rev. B **71**, 193102 (2005).

[71] C. H. Patterson, Phys. Rev. B **72**, 085125 (2005).

[72] I. de P. R. Moreira, F. Ilas, and R. Martin, Phys. Rev. B **65**, 155102 (2002).

[73] P. W. Anderson, Phys. Rev. **102**, 1008 (1956).

[74] Z. Szotek *et al.*, Phys. Rev. B **68**, 054415 (2003).

[75] G. K. H. Madsen and P. Novak, Europhys. Lett. **69**, 777 (2005).

[76] H. Jeng, G. Y. Yuo, and D. J. Huang, Phys. Rev. Lett. **93**, 156403 (2004).

[77] I. Leonov *et al.*, Phys. Rev. Lett. 146404 (2004).

[78] V. I. Anisimov, I. S. Elfimov, N. Hamada, and K. Terakura, Phys. Rev. B **54**, 4387 (1996).

[79] H. T. Stokes, stokes.byu.edu/isotropy.html (2002).

[80] H. T. Stokes and D. M. Hatch, Phase Trans. **34**, 53 (1991).

[81] H. T. Stokes and D. M. Hatch, COPL, www.physics.byu.edu/ stokesh/isotropy.html (2001).

[82] E. Ascher and J. Kobayashi, J. Phys. C **10**, 1349 (1977).

[83] D. M. Hatch and H. T. Stokes, Phys. Rev. B **65**, 014113 (2001).

[84] S. C. Miller and W. F. Love, *Tables of Irreducible Representations of Space Groups and Co-Representations of Magnetic Space Groups* (Pruett, Boulder, 1967).

[85] Y. Miyamoto and M. Shindo, J. Phys. Soc. Jpn. **62**, 1423 (1993).

[86] C. Medrano *et al.*, Phys. Rev. B **59**, 1185 (1999).

[87] B. J. Campbell, H. T. Stokes, D. E. Tanner, and D. M. Hatch, J. Appl. Cryst. **39**, 607 (2006).

[88] H. P. Pinto and S. D. Elliot, J. Phys. Cond. Matt. **18**, 10427 (2006).

[89] D. Owoc *et al.*, Physica B **359**, 1339 (2005).

[90] R. Gupta, A. K. Sood, P. Metcalf, and J. M. Honig, Phys. Rev. B **65**, 104430 (2002).

[91] Z. Kakol and A. Kozlowski, Solid State Sci. **2**, 737 (2000).

[92] R. Shankar, Rev. Mod. Phys. **66**, 129 (1994).

[93] F. Wilczek, *Fractional Statistics and Anyon Superconductivity* (World Scientific, ADDRESS, 1990).

[94] F. E. Camino, W. Zhou, and V. J. Goldman, Phys. Rev. B **72**, 075342 (2005).

[95] A. Zee, cond-mat/9501022 (1995).

[96] E. Witten, Commun. Math. Phys. **121**, 351 (1989).

[97] M. F. Atiyah, Publ. Math. IHES **68**, 175 (1988).

[98] G. V. Dunne, hep-th/9902115 (1999).

[99] R. J. Szabo, physics/0401142 (2004).

[100] L. Susskind, hep-th/0101029 (2001).

[101] R. Moessner and S. L. Sondhi, Phys. Rev. Lett. **86**, 1881 (2001).

[102] T. Senthil and P. A. Lee, Phys. Rev. B **71**, 174515 (2005).

[103] T. Senthil and M. P. A. Fisher, Phys. Rev. B **62**, 7850 (2000).

[104] M. Freedman *et al.*, cond-mat/0307511 (2003).

[105] E. Ardonne, P. Fendley, and E. Fradkin, cond-mat/0311466 (2003).

[106] M. Freedman, A. Kitaev, M. Larsen, and Z. Wang, quant-ph/0101025 (2002).

[107] S. D. Sarma, M. Freedman, and C. Nayak, Phys. Rev. Lett. **94**, 166802 (2005).

[108] M. Oshikawa and T. Senthil, Phys. Rev. Lett. **96**, 060601 (2006).

[109] C. Ling *et al.*, Phys. Rev. B **62**, 15096 (2000).

[110] T. Saitoh *et al.*, Phys. Rev. B **62**, 1039 (2000).

[111] D. Dessau *et al.*, Phys. Rev. Lett. **81**, 192 (1998).

[112] Y. D. Chuang *et al.*, Science **292**, 1509 (2001).

[113] N. Manella *et al.*, Nature **438**, 474 (2005).

[114] S. de Jong *et al.*, cond-mat/0611287 (2006).

[115] T. Valla *et al.*, Science **314**, 1914 (2006).

[116] A. Kanigel *et al.*, Nature Physics **2**, 447 (2006).

[117] J. G. Bednorz and K. A. Müller, Z. Phys. B: Cond. Matt. **64**, 189 (1986).

[118] A. Schilling, M. Cantoni, J. D. Guo, and H. R. Ott, Nature **363**, 56 (1993).

[119] P. W. Anderson, Science **235**, 1196 (1987).

[120] J. Orenstein and A. J. Millis, Science **288**, 468 (2000).

[121] A. J. Schofield, Contemp. Phys. **40**, 95 (1999).

[122] P. W. Anderson, cond-mat/0510053 (2005).

[123] S. Sachdev, cond-mat/0211005 (2002).

[124] B. P. Stojkovic *et al.*, Phys. Rev. Lett. **82**, 4679 (1999).

[125] M. Brunner, F. Assaad, and A. Muramatsu, Phys. Rev. B **62**, 15480 (2000).

[126] M. Rogers, cond-mat/0504141 (2005).

[127] R. Coldea *et al.*, Phys. Rev. Lett. **86**, 5377 (2001).

[128] H. M. Ronnow *et al.*, Nature **440**, 1025 (2006).

[129] D. S. Dessau and Z. X. Shen, in *Colossal Magnetoresistive Oxides*, edited by Y. Tokura (Gordon and Breach, London, 1998).

[130] O. Chmaissem *et al.*, Phys. Rev. B **67**, 094431 (2003).

[131] C. Zener, Phys. Rev. **82**, 403 (1951).

[132] P. G. de Gennes, Phys. Rev. **118**, 141 (1960).

[133] K. Kubo, J. Phys. Soc. Jpn. **33**, 929 (1972).

[134] S. Jin, J. Appl. Phys. **76**, (1994).

[135] Y. Moritomo, A. Asamitsu, H. Kuwahara, and Y. Tokura, Nature **380**, 141 (1996).

[136] A. S. Alexandrov and A. M. Bratovsky, Phys. Rev. Lett. **82**, 141 (1999).

[137] G. Baskaran, cond-mat/0607369 (2006).

[138] Z. Sun *et al.*, Phys. Rev. Lett. **97**, 056401 (2006).

[139] J. Y. Son *et al.*, Phys. Rev. B **70**, 012411 (2004).

[140] Y. Tang *et al.*, Phys. Rev. B **72**, 132403 (2005).

[141] P. K. de Boer and R. A. de Groot, Phys. Rev. B **60**, 10758 (1999).

[142] X. Y. Huang, O. Mryasov, D. Novikov, and A. Freeman, Phys. Rev. B **62**, 13318 (2000).

[143] M. Kubota *et al.*, J. Phys. Soc. Jpn. **69**, 1606 (1999).

[144] P. Mijarends *et al.*, Phys. Rev. B **75**, 014428 (2007).

[145] J. E. Medvedeva, V. I. Anisimov, O. N. Mryasov, and A. J. Freeman, J. Phys. Cond. Matt. **14**, 4533 (2002).

[146] S. Galamic-Mulaomerovic and C. H. Patterson, Phys. Rev. B **72**, 035127 (2005).

[147] T. Kimura *et al.*, Phys. Rev. B **58**, 11081 (1998).

[148] D. N. Argyriou *et al.*, Phys. Rev. B **61**, 15269 (2000).